2010-12-22

Air-Sea Turbulent Flux Measurements and their Relationship to the Turbulent Kinetic Energy Dissipation Rate in the Ocean

Silvia Gremes-Cordero
University of Miami, sgremes@rsmas.miami.edu

UNIVERSITY OF MIAMI

AIR-SEA TURBULENT FLUX MEASUREMENTS AND THEIR RELATIONSHIP TO THE TURBULENT KINETIC ENERGY DISSIPATION RATE IN THE OCEAN

By

Silvia Gremes-Cordero

A DISSERTATION

Submitted to the Faculty
of the University of Miami
in partial fulfillment of the requirements for
the degree of Doctor of Philosophy

Coral Gables, Florida

December 2010

UNIVERSITY OF MIAMI

A dissertation submitted in partial fulfillment of
the requirements for the degree of
Doctor of Philosophy

AIR-SEA TURBULENT FLUX MEASUREMENTS AND THEIR RELATIONSHIP TO THE TURBULENT KINETIC ENERGY DISSIPATION RATE IN THE OCEAN

Silvia Gremes-Cordero

Approved:

_____ William M. Drennan, Ph.D. Professor of Applied Marine Physics	_____ Terri A. Scandura, Ph.D. Dean of the Graduate School
_____ Rana A. Fine, Ph.D. Professor of Marine and Atmospheric Chemistry	_____ Maria J. Olascoaga, Ph.D. Assistant Professor of Applied Marine Physics
_____ Brian K. Haus, Ph.D. Associate Professor of Applied Marine Physics	

GREMES-CORDERO, SILVIA (Ph.D., Applied Marine Physics)

Air-Sea Turbulent Flux Measurements and their Relationship to the Turbulent Kinetic Energy Dissipation Rate in the Ocean

(December 2010)

Abstract of a dissertation at the University of Miami.

Dissertation supervised by Professor William M. Drennan.
No. of pages in text. (117)

A study of the turbulent transfer of properties across the ocean surface and the dissipation of the energy transferred to the upper ocean is here presented. Two experiments were analyzed, both conducted during summer in the North Atlantic during phytoplankton blooms. The Marine Aerosol Production from marine sources (MAP) experiment, performed during summer of 2004, allowed for the calculation of the air-sea turbulent fluxes of momentum and humidity in high wind conditions. This analysis aims to improve the parameterization of air-sea turbulent fluxes, fundamental for coupled atmospheric-ocean models. In particular, there are very few previous calculations of the bulk coefficients for humidity fluxes over 18m/s, making the present work a fundamental contribution to the field. Wind speed and humidity fluctuations were measured with an eddy flux tower mounted on a vessel. The methods applied to calculate momentum and humidity flux were the eddy correlation or eddy covariance, the bulk, and the inertial dissipation method. Due to strong flow distortion effects derived from the instrumentation set up on board, the inertial dissipation method proved to be the more appropriate calculation for this experiment.

On the oceanic side, the Labrador Sea experiment conducted in summer 2004, allowed for the study of the dissipation of energy within the upper surface layer (up till 2 m depth). This study is useful to improve the understanding of the relevant surface processes that should be included in the parameterization of the turbulent kinetic energy dissipation rates. The measurements were obtained with an Air-Sea Interaction Spar (ASIS) buoy, which includes a flux tower and several instruments installed along its underwater structure. In particular we analyzed data from a pulse-to-pulse coherent Doppler sonar, which allows the calculation of current velocity fluctuations at densely spaced bins. The analysis of turbulent kinetic eddy dissipation rates (TKEDR) in different wind regimes allowed us to confirm the need to include the wave effects together with the wind, as a fundamental factor to parameterize the TKEDR. Near surface TKEDRs were found to be enhanced above classical law-of-the-wall estimates at moderate to high wind speeds, and also to be independent of the wave phase, even at high winds. This is contrary to recent observations showing TKEDR beneath wave crests to be significantly enhanced over those beneath wave troughs, and helps resolve a recent controversy in the literature.

In summary, new perspectives on the air-sea flux parameterizations are presented in this dissertation. They will ultimately provide insight for the numerical model community for coupled atmospheric ocean models.

TABLE OF CONTENTS

List of Figures

List of Tables

Chapter 1

Introduction

Air-sea turbulent fluxes are one of the most complex quantities to estimate in oceanic sciences, due to the variety of physical processes involved. They play a crucial role in the transfer of properties between the atmosphere and the ocean, two of the biggest components of our climate system. Their parameterization is of fundamental interest for the applicability of coupled ocean-atmospheric models of climate change prediction and thus has received preferred attention on both theoretical and experimental grounds in the last decades. However, the subject is far from being totally understood or furthermore, solved. The combination of many physical mechanisms acting simultaneously and interacting between them, plus the inherent difficulties of obtaining micro-measurements at sea, makes any estimate a challenge.

Initially the focus of this dissertation was to deepen our knowledge on the turbulent air-sea gas exchange and its transfer velocity. In particular, we were interested in greenhouse gases (GHG) due to their key role in climate changes, especially in Carbon Dioxide variability. GHGs are naturally present in the atmosphere in small quantities, but play an essential role in the Earth's energy by absorbing and emitting infrared radiation. Interestingly, CO_2 concentration has grown from 280 to 380 ppm in the last hundred years (Dilling et al., 2003; IPCC, 2007). The ocean acts as a regulator of the GHG excess, by absorbing at least one third of the anthropogenic CO_2 emitted to the atmosphere. Therefore, it is very important to understand and be able to quantify the processes that affect the exchange of CO_2 at the ocean surface.

Within the first millimeter of both sides of the ocean surface the exchange of properties is driven by diffusion or viscosity (Jähne and Haußecker, 1998; Fairall et al., 2000). Far from these diffusive and viscous layers, the transport of mass (gases), heat and momentum is essentially turbulent. Our attention is focused on the physical processes affecting the lower 10 m of the atmosphere and the upper 5 m of the ocean column, where turbulence dominates.

With this idea in mind an ASIS buoy, or Air-Sea Interaction Spar buoy, was deployed on the Labrador Sea during the summer of 2004. The Labrador Sea is an important area of dense water production, an essential part of the Meridional Overturning Circulation (MOC), fundamental for climatological studies. During the summer, as the ice cover melts, sunlight in combination with nutrients allow for a strong phytoplankton bloom to develop. The ASIS buoy was equipped to measure eddy correlation fluxes of CO_2, heat, water vapor, and momentum, wind speed, humidity, air and water temperature, CO_2 concentration in the air and water, atmospheric stability, surface waves, currents, dissipation rates in the water column as well as a variety of quantities of biogeochemical interest. See Martz et al. (2009) for the detailed description of the latter.

Our goal of the experiment was to determine a parameterization of the air-sea CO_2 flux (F) in terms of the turbulent kinetic energy dissipation rate, or TKEDR (ε) near the surface. This follows the initial work of Lamont and Schott (1970) who proposed that ε should be a better parameter for the parameterization than wind speed, the most commonly used, since gas transfer is controlled by turbulence in the water column, which is only partially determined by wind speed.

However, a failure of part of the flux tower electrical system inhibited the calculation of the gas transfer F. For this reason we decided to take a slightly different approach, namely to study from this experiment only the TKEDR in the upper ocean, and to study the atmospheric-based turbulent fluxes separately from another experiment, the recent MAP (Marine Aerosol Production) experiment conducted in the North Atlantic during high winds.

On the meteorological part, data obtained with a flux tower on board the research vessel 'Celtic Explorer' during the summer of 2006 are presented (Chapter 2). The area was chosen for being a well known site of phytoplankton bloom during summer. During these blooms, the CO_2 concentration differences between air and ocean are very large, making air-sea gas fluxes easier to measure. The data set includes wind speed, temperature, humidity, CO_2 concentration, and sound speed. However, the air-sea turbulent fluxes of momentum and humidity are the only focus of our attention. Interestingly, the data set presents some unique characteristics in terms of the environmental conditions. Indeed a massive storm impacted the area after only few days of measurements, allowing wind measurements of up to 24 m/s and hence drag coefficient calculations in gale winds. At the same time, the storm also created some problems with the humidity data, but enough measurements were obtained as to allow for calculations of humidity fluxes. These are some of the highest wind speeds in which such fluxes have been measured; hence the present calculations constitute a valuable contribution to the literature.

On the oceanic side, turbulence in the upper few meters is studied here through the spectral analysis of current speed variability, obtained through the Acoustic Doppler

devices (DopBeams) mounted on the ASIS mentioned (Chapter 3). In particular we focus our attention on the Labrador Sea experiment, and the effect of winds and waves on the turbulent kinetic energy dissipation rates, together with the analysis of TKEDR dependency on wave phase (Chapter 4).

In conclusion, a thoughtful study of turbulence at the ocean interface is here presented. It gives us fresh input on the physical processes influencing the TKEDR variability and hence, on turbulent fluxes across the interface. It is also a presentation of new methods for the TKEDR estimates and a detailed analysis of the DopBeam performance in open ocean. By giving new perspectives on the air-sea fluxes parameterizations, it will ultimately give insight to the numerical model community, for coupled atmospheric ocean models.

Chapter 2

Air-sea turbulent flux measurements in high wind conditions

2.1 – Description

Air-sea interaction processes of small spatial scales (from few to hundreds of meters) are not resolved by ocean-atmosphere coupled models, and thus they must be parameterized. Such a parameterization relies critically on accurate measurements of air-sea fluxes, which are usually extremely difficult to obtain in the open-ocean, and in particular when obtained on board a vessel in motion. Sensors must be very rugged and accurate, and sampling resolution must be high, at least 12 Hz (Drennan, 2006). In addition, motion corrections must be applied to account for 3D accelerations, and flow distortion due to the platform geometry should also be considered (Anctil et al., 1994; Drennan, 2006).

Given the above difficulties, it is customary to base the transfer calculations on mean values of the different parameters engaged. Such formulae involve non-dimensional coefficients that have been reliably determined only under low-moderate wind conditions, i.e., between 4 and 15 m/s (Drennan, 2006; Donelan, 1990). The work presented in this chapter is an attempt to improve the parameterization of the turbulent air-sea fluxes by determining those coefficients. We report direct in situ measurements of momentum and humidity fluxes in high wind conditions during the phytoplankton bloom occurring annually in the north Atlantic during summer. Momentum fluxes are higher during high winds, when also marine aerosol concentrations increase. O'Dowd et al.

(2004) showed that the organic fraction of marine aerosols increases during phytoplankton blooms.

In this context, the Marine Aerosol from Natural resources Project (MAP), aimed at understanding the concomitant physical processes present during the phytoplankton bloom and their role the air-sea transfers, was conducted during summer 2006 in the North Atlantic Ocean, near the Irish coast (Fig. 2.1), around 51-57° N and 10-12º W. It constituted an excellent opportunity to carry out measurements of momentum and mass exchange in high wind conditions. In addition, the phytoplankton bloom alters some of the surface physical characteristics, by modifying the surface tension and the roughness, possibly influencing the air-sea exchange. In this way the data analyzed here present some unique characteristics that allow some insight into air-sea transfer in special conditions.

The wind conditions during the MAP experiment were highly variable with values of up to 24 m/s, where the applicability of the classical bulk parameterizations is in doubt (Drennan et al., 1999). It is then of considerable interest to understand the effect of the high wind in the flux calculations, and in the transfer coefficients. Indeed as the wind speed increases, wave breaking increases, thus creating more turbulence, bubbles and spray. The effect of such different conditions over the humidity fluxes remains still unknown and its investigation is one of the purposes of this work.

2.1.2– Theoretical basis

Three-dimensional turbulence at the ocean surface can be generated by different mechanisms, mainly by shear production and buoyancy (Drennan, 2006; Fairall et al., 2000). Shear production comes from wind, and is associated with surface roughness. Buoyancy is motion of the air column induced by differential heating or cooling (sensible or latent heat).

Turbulent transfer is typically orders of magnitude larger than the molecular transfer occurring very close to the ocean surface (Jähne and Haußecker, 1998). At the ocean surface, we can define the atmospheric surface layer as the bottom 10% of the atmospheric boundary layer, and the viscous sublayer, as the layer occupying the first mm of both sides of the media. Within the atmospheric surface layer, far from the viscous layer, momentum and mass fluxes can be defined as:

$$\vec{\tau} = \rho\,(-\overline{w'u'}\,\hat{i} - \overline{w'v'}\,\hat{j}) \quad \text{and} \quad F_x = \rho\,\overline{w'x'} \tag{2.1}$$

respectively. Primes indicates turbulent fluctuations and the over bars represent a suitable average in time (Drennan, 2006). Here u', v', w' are the wind velocity components (horizontal in- line with the mean wind, horizontal cross-wind and vertical, respectively), ρ is the air density, and x' is the mixing ratio of any substance, such as methane or carbon dioxide, with respect to dry air.

Most of the analysis done over the turbulent sublayer is based on the theories of Obukhov (1946) and Monin-Obukhov (1954) about flow similarity. Assuming stationary and homogeneous conditions within the surface layer, the vertical momentum flux is

considered constant and proportional to the square of the so-called friction velocity u_*, as $\left|\vec{\tau}\right|/\rho = u_*^2 = \nu\ dU/dz - \overline{u'w'}$ where ν is the kinematic viscosity of air and U is the horizontal wind component in the mean wind direction. The friction velocity is introduced as a velocity scale in the Monin-Obukhov (MO) theory. Assuming that turbulence in the surface layer (far from the very near-surface region, where molecular processes are also important) is generated by only surface shear and buoyancy, the MO theory determine that the gradients and scaling parameters are related by means of universal dimensionless gradient functions Φ as:

$$\frac{\partial U}{\partial z} = \frac{u_*}{\kappa z}\Phi_u\left(\frac{z}{L}\right) \quad \text{and} \quad \frac{\partial X}{\partial z} = \frac{x_*}{\kappa z}\Phi_x\left(\frac{z}{L}\right) \tag{2.2}$$

for momentum and mass, where z is the mean height above the surface and L is the Obukhov length, $L = -u_*^3/\kappa g(\overline{w'\theta'}/T_0 + 0.61\overline{w'q'})$, with $\kappa = 0.4$ as the Von Kármán constant (Drennan, 2006) being g the gravitational constant, q' is the humidity fluctuation (equivalent to x above) , θ the potential temperature and T_0 a reference absolute temperature. Integrating (2.2) from the surface to some height z in the constant flux layer, the velocity profile can be obtained in terms of the gradient functions Φ and the structure functions (for a detailed description see Drennan, 2006). In neutral conditions, where buoyancy effects can be disregarded, one can obtain the well-known logarithmic profiles. For the velocity profile of a shear layer (Drennan, 2006; Donelan, 1990), we have:

$$\frac{U_z}{u_*} = \frac{1}{\kappa}\ln\frac{z}{z_0} \tag{2.3}$$

According to the MO theory, the Drag coefficient $C_D = u_*^2 / U^2$ which relates the momentum flux to the mean wind speed, is a function of the roughness, the height of the instrument, and the stability parameter described previously. It is customary to eliminate the dependence on stability and height by considering the neutral drag coefficient at a reference height of 10 m. The same consideration is applied to the wind speed, and we are calling it U_{10}. This so-called 'stability correction' is also applied to the humidity fluxes as well.

Direct measurements of turbulent fluxes over the ocean are influenced by different factors. The most relevant in modifying the results are the mean wind speed and gustiness, and the surface conditions or swell. Most of the measurements at sea so far were obtained in low to moderate wind conditions and the results are well known (Pedreros et al., 2003; Donelan et al., 1997). For example, swell effects can be significant at low to moderate winds increasing or decreasing the drag, for swell travelling against or with the wind respectively. Also, evidence to date supports constant Dalton coefficients being independent of wind speed at low to moderate wind conditions (up to 20 m/s). However, is not clear what to expect in stronger winds. For example, CBLAST field data analysis shows a leveling of C_D above 25 m/s (French et al. 2007); but Drennan et al. (2007) results' show a constant Dalton coefficient over the entire range of wind speed values, from 5 m/s up to 30 m/s.

The calculation of the turbulent fluxes can be done through direct or indirect methods. Direct measurements of wind velocity turbulent fluctuations over the ocean have been proved a difficult task, due mainly to the reasons listed above and platforms

limitations (in both buoys and ships). However, the instrumentation available allows us to measure the turbulent fluctuations and calculate then the fluxes through a direct method called 'eddy correlation' or 'direct covariance' (EC) method (Dupuis et al., 2003; Drennan, 2006; Fairall, 2000). The calculation of fluxes via this method requires the measurement of turbulent fluctuations of wind speed and some other parameter at a high sample rate and simply consists of the evaluation of equation (2.1) by calculating the covariance of the fluctuations. The sampling should be maintained for a long period and be fast enough as to capture all of the scales contributing to the flux. For the common variables measured at sea, the sampling rates should be at least 10 Hz and the duration of the measurements at least 20 min to ensure that all of the scales contributing to the turbulent flux are recorded (Drennan, 2006). For the present experiment, data was obtained at 20 Hz, in a continuous way (except for few days due to weather conditions). Once the fluctuations are recorded, the samples are quality controlled and detrended. The data is corrected then for motion effects (Anctil et al., 1998; Drennan et al., 1999) since sensors are set in a non-stationary platform. Then the wind vector is rotated into the mean wind direction.

For accuracy assessment, the bulk method is also applied. The bulk method is an indirect method that requires knowledge of non-dimensional coefficients. The bulk method gives only estimates of the fluxes based on the mean values of the variables along with empirical bulk coefficients. It requires applying the stability correction to the wind speed measured for neutral conditions (in the MO sense). The bulk fluxes for momentum and humidity from (2.1) can be expressed respectively as:

$$|\tau| = \rho u_*^2 = \rho C_D (U_z - U_0)^2 \qquad (2.4)$$

and $$F_q = -u_* q_* = U_z C_E (Q_{sat} - Q_z)$$

where z stands for any height, $q = \rho x$, and '0' indicates surface. C_E is the bulk mass coefficient for humidity fluxes, called the Dalton number. Even if the Bulk method is more practical, the error involved in using mean quantities for turbulent fluxes is important and cannot be disregarded. Note that after the stability correction is introduced, z is changed into a '10', or '10N' subscript.

While the EC is the most precise and standard method for calculating air-sea fluxes, in some circumstances it becomes affected by flow distortions, in particular in the band of frequencies where the supportive platform is most strongly affected by the waves (Pedreros et al., 2003; Dupuis et al., 2003; Edson et al. 1998).

Another indirect method, unaffected by flow distortion, is the Inertial Dissipation method (ID), based in spectral analysis of the velocity fluctuations. The ID method is based in the Kolmogorov theory to calculate the dissipation rates of turbulent energy as being proportional to the part of the spectra called 'inertial subrange', which frequencies are very different from the ones corresponding to the ship movements, making the fluxes calculated in this way unaffected by flow distortion. Several authors contributed to the validation of this method in the last few decades (Donelan 1990; Drennan 2006; Large and Pond 1981; Smith et al. 1992; Dupuis et al. 1997, 1999). For a review, see Fairall and Larsen (1986) or Edson et al. (1998). The ID method is derived from the turbulent energy balance equation and hence depends on the relative importance of each term.

For momentum, the turbulent kinetic energy (TKE) equation is:

$$u_*^2 \frac{\partial U}{\partial z} + F_B - \frac{\partial}{\partial z}\overline{w'e'} - \frac{1}{\rho}\frac{\partial}{\partial z}\overline{w'p'} - \varepsilon = 0 \qquad (2.5)$$

where $e' = (u'^2 + v'^2 + w'^2)/2$ represents fluctuations in TKE, p' are pressure fluctuations, F_B is the buoyancy force and ε is the TKE dissipation rate. The terms in (2.5) are, respectively, production of TKE from shear, production (or loss) due to buoyancy, transport of TKE, pressure transport, and loss due to dissipation, ε (Drennan, 2006).

Dividing (2.5) by $u_*^3/\kappa z$ we arrive at

$$\Phi_u - \zeta - \Phi_e - \Phi_p - \frac{\kappa z}{u_*^3}\varepsilon = 0 \qquad (2.6)$$

where $\zeta = z/L$ is the stability parameter, that is, the ratio between the measurements' height above the ocean and the Monin-Obukhov length. Assuming MO theory, the terms in (2.6) are expected to be universal functions of ζ. With little experimental data available on either Φ_e or especially Φ_p, they are usually combined as a single transport (or imbalance) term $\Phi_t = \Phi_e + \Phi_p$. This term is then either assumed to be zero (Large and Pond, 1981), as we will do, or determined empirically (Dupuis et al., 1997). When Φ_u=1, that is for neutral conditions, equation (2.6) leads to the well know 'Law of the wall' definition, $\varepsilon = u_*^3/\kappa z$.

The TKE dissipation rates (TKEDR) are calculated from the spectra of velocity fluctuation by assuming the existence of an inertial subrange (ISR) following the Kolmogorov theory of energy cascade (Kolmogorov, 1941). Kolmogorov theory is valid

for wavenumber spectra, but it is common to obtain the TKEDR from the frequency spectra, by assuming Taylor's or "frozen turbulence" hypothesis. Taylor's hypothesis states that the frequency spectra is proportional to the wavenumber spectra, with a proportionality constant equal to a mean advection velocity (Lumley and Terray, 1983). The TKEDR for momentum and mass are defined, respectively:

$$\varepsilon_u = (E_u / \alpha_u)^{3/2} (2\pi / U) \tag{2.7}$$

$$\varepsilon_x = (E_x / \alpha_x) \varepsilon_u^{3/2} (2\pi / U)^{2/3} \tag{2.8}$$

where $E_{u,x}$ is the mean spectral energy (S) multiplied by $f^{5/3}$ with f as frequency in Hz. The universal constants have a value $\alpha_u = 0.55$ for momentum (Dupuis et al., 2003), and $\alpha_u = 0.8$ for mass (Drennan, 2006). U is the relative mean wind at the sensor (Dupuis et al., 2003).

This dependence only on ISR frequencies (f > ~0.5Hz) is the key advantage of the ID method. These high frequencies are unaffected by either turbulent (but not mean) flow distortion or platform motion, as stated previously. Hence the method remains popular for flux measurements from vessels (Yelland et al., 1998).

Mathematical manipulation of the previous equations, as described in Dupuis et al., (1997 and 1999) leads to the expression for momentum and humidity fluxes in the form:

$$u_* = [\kappa z \varepsilon / (\Phi_u(\zeta) - \zeta]^{1/3} \tag{2.9}$$

$$\overline{wn} = [\kappa z u_* \varepsilon_n / \Phi_n(z/L)]^{1/2} \tag{2.10}$$

The applicability of this method has been questioned in developing seas (Taylor and Yelland, 2001), in swell dominated conditions (Donelan et al., 1997), and in light winds (Yelland et al., 1998). However, in the mixed seas typical of the open ocean ID fluxes compare well with direct measurements (Dupuis et al., 2003), as we will show in the present work.

Note that disregarding which method applied, the drag and latent heat exchange coefficients are ultimately calculated here through their definitions:

$$C_{DN} = (u_* / U_{10})^2 \tag{2.11}$$

$$C_{EN} = \frac{\overline{wq}}{U_{10N}(Q_{sat} - Q_{10N})} \tag{2.12}$$

where the subscript *N* represents neutral conditions, and 'sat' stands for saturated humidity at the surface, as described in Fairall et al. (2000).

There are very few existing calculations of Dalton coefficients for winds over 18 m/s, and of Drag coefficients for winds over 20 m/s, making the present work essentially important for the flux community. There are only two examples of Dalton number calculations with winds over 18 m/s. One is the CBLAST experiment data of Drennan et al., (2007) and the other is the Greenland Flow Distortion Experiment (GFDex) of Petersen and Renfrew (2009). The GFDex was performed in high-wind conditions; they flew 12 missions over the Denmark Strait and the Denmark Sea, creating the first air-sea fluxes data set in this area. They used the Eddy Covariance method to calculate the turbulent fluxes of momentum, moisture and heat, finding values for the bulk exchange coefficients at the upper end of previous results, that is $C_D = (2.04 \pm 0.3) \times 10^{-3}$ and $C_E = (1.57 \pm 0.27) \times 10^{-3}$ for winds between 15 and 19 m/s. The Coupled Boundary Layer

Air-Sea Transfer (CBLAST) Departmental Research Initiative, allowed the acquisition of direct turbulent flux measurements in the high wind boundary layer of a hurricane. With aircraft data from 6 different excursions during 2003, they calculated the humidity fluxes and Dalton numbers in winds up to 29 m/s, finding no dependence of the Dalton numbers on wind A summary of previous calculations of turbulent air-sea fluxes and data sets available in literature is presented in Drennan et al., 2007 (Fig. 2.2). While they are both important data sets, note that neither experiment represent true in situ data, as they were both obtained with aircraft.

The best known data set for humidity fluxes over the ocean is the Humidity Exchange over the Sea experiment (HEXOS), aimed at finding accurate empirical heat and water vapor flux parameterization formulas in high wind conditions (DeCosmo et al., 1996). Measurements were obtained on a fixed platform in the North Sea, with winds up to 18 m/s in the case of water vapor fluxes. Their results point out a nearly constant relation between wind and Dalton number, with $C_E = (1.12 \pm 0.24) \times 10^{-3}$ in agreement with the classic results of Smith (1980) of $C_E = 1.2 \times 10^{-3}$.

The data analyzed here was obtained with an 'eddy-flux tower', consisted of a sonic anemometer for wind turbulent fluctuations and sound speed variability, basic wind monitors, a LICOR gas analyzer, and intakes for other gas and aerosol measurements. Measurements were obtained at 20 Hz, corrected for ship motion and normalized to the standard 10 m over the ocean surface.

2.1.2.1. Accuracy of the measurements - Flow distortion

As mentioned previously, direct flux measurements over the sea have been limited by both the mobility and geometry of typical marine platforms and vessels. With the development in recent decades of compact and inexpensive rate gyros and accelerometers, special systems have been developed for use on buoys (Anctil et al., 1994) and ships (Edson et al., 1998) that allow for a correction of the data accounting for the movement of the platform. Consequently, the problems associated with platform mobility have essentially been solved.

Flow distortion is a limitation in the accuracy of the flux calculations that is neither easily avoidable nor quantifiable. It is related to the geometry of the supporting platform and to the position of the instruments on it. Of particular importance are the ship hull, the ship superstructure, the mast, the size and proximity of sensors, and of other structures. In considering flow distortion the mean and turbulent components of the flow field are usually considered separately (Wieringa, 1980; Wyngaard, 1981). Mean flow distortion is characterized by the lifting, tilting and compression of flow streamlines as they pass over or around the platform. The effects of mean flow distortion can be accurately assessed through numerical models using commercial software (*e.g.* Yelland et al., 1998; Dupuis et al., 2003) or flume studies using scale models. Instead the effect of distortion of the turbulent components remains beyond the reach of current numerical models, and therefore is more difficult to assess. Recent studies comparing turbulent fluxes measured on large ships with those from nearby buoys (which are assumed to be largely free of flow distortion effects) indicate a good comparison between scalar fluxes,

but an enhancement of the ship-board momentum flux by order 15% (Edson et al. 1998; Pedreros et al. 2003).

Oost et al. (1994) examined several methods for correction of turbulent fluxes depending on the geometry of the platform. Their corrections depend on the shape of the platform (whether it is a cylindrical or an arbitrary shape) and on the distance of the object to the sensor. They applied their models to data obtained during 1986 at a research platform 9 km off the Dutch coast for the HEXOS experiment. They conclude that the typical "tilt correction" is not enough to take into account all the distortions the streamlines are subjected to, and that a deceleration of the mean wind speed of up to 10% is verifiable.

Dupuis et al. (2003) performed turbulent measurements during the FETCH experiment conducted during March-April 1998 in the Gulf of Lion (N. Mediterranean Sea). They compared the turbulent fluxes calculated from data obtained with a research vessel (R/V "L'Atalante") against the fluxes obtained with an ASIS buoy deployed in the area. They analyzed the impact of flow distortion due to the ship structure mainly through numerical simulations. They assumed that only the mean characteristics of wind speed are disturbed and found that for moderate, bow-on winds, the flow at 17 m was decelerated by 8%, tilted upward by ~7° and uplifted by 1.2m. The effects vary with wind speed and direction, with the distortion increasing significantly for flow angles greater than 30° relative to the bow.

Pedreros et al. (2003) compared fluxes calculated from ASIS and from R/V "L'Atalante", also during FETCH, and found an overestimation of 18 % for momentum

fluxes due to flow distortion for the vessel calculations. They describe an effective way to reduce the effects of distortion, and that is to consider accurate only the measurements obtained with a relative angle to the bow smaller than 30˚. Moreover they showed how the best conditions are met when the wind speed is at least twice the ship speed. They also found that the heat fluxes are not altered by the flow distortion.

Popinet et al. (2004) proposed a time-dependent numerical technique to investigate the flow distortions by analyzing the data obtained with the R/V Tangaroa in the Pacific near New Zealand, during March 2002. Their results show also that flow distortion depends on the relative wind direction. For bow-on flows, they found an overestimation of wind speed of about 7%, while for a relative flow of 90˚, the overestimation was around 10%.

In the present analysis, the need of a correction for flow distortion is concluded after the obviously abnormal values obtained with the EC method, and after the comparison between the EC and ID methods, the latter one being unaffected by turbulent flow distortion. The factor utilized in the mean wind speed correction (8%) is derived from the literature available presented here.

In the following, a description of the experiment, the data available, and a first treatment of the data set is presented in section **2.2**. The main results are described in section **2.3** and discussed in section **2.4**, in the context of the previous experiments cited. Section **2.5** presents the conclusions of the present chapter.

2.2 – The MAP experiment

The MAP experiment is a European Union integrated project involving 16 different institutions. It integrates Europe's leading expertise in aerosol physics and chemistry and marine biogeochemistry to quantify the production of primary and secondary marine aerosol formation from natural sources. It aims at understanding of the key processes relating aerosol formation to gas transfer in the presence of surfactants. Primary marine sea-spray aerosol (PMA) production and iodine vapor sea-air transfer can be quantified as a function of organic matter at the ocean surface (measured in-situ and as a function of satellite derived chlorophyll), wind fields and white cap coverage. The integration of the field, lab, and remote-sensing studies can be ultimately incorporated into large scale models to quantify the source of primary aerosol over the ocean and to provide an estimate of the global sea-air transfer of organo-iodine. The resulting numerical models will significantly advance our capability of quantifying the impact of marine aerosol on the marine boundary layer chemistry, the radiative forcing, and the impacts on climate (http://macehead.nuigalway.ie/map/).

The experiment was conducted between June 12th and July 7th, 2006 on the west coast of Ireland (Fig. 2.1). Wind speed was fairly variable during the experiment, especially during the first part of (between June 12th and 22nd). On June 23rd the onset of a violent storm destroyed part of the instrumentation and forced the vessel to return to port for repairs. The intense storm yielded one of the most interesting data sets obtained in the North Atlantic during a bloom, allowing for the calculation of the non-dimensional coefficients of the bulk parameterizations under high winds (up to 24 m/s). The second

part of the experiment, from June 27th till July 5th, presents less intense and more even winds, between 5 and 15 m/s.

2.2.1 – Instrumentation and first treatment of data

The data set analyzed here were obtained with a flux tower on board the R/V Celtic Explorer. The Eddy flux package consists of a Gill R3A sonic anemometer and a LICOR 7500 CO*2*/H*2*0 analyzer, along with a Motion Pack system that allowed for ship movement corrections. This Eddy flux package allows for the measurement of the turbulent fluctuations of air temperature, wind speed and direction, humidity concentrations, and CO2 concentrations at a frequency of 20 Hz. Such measurements combined with the ship data (as course, speed) and the motion package data, allow for the calculation of momentum and mass fluxes.

Corrections were applied for misalignment of the sensors. We assume a coordinate system so that the u component of the wind remains in the mean wind direction, and apply tilt corrections to force $\overline{w} = \overline{v} = 0$. In addition to these corrections, files also needed to be sorted out according to the range of some parameters' variation inside the file. Indeed, if the ship direction changes more than 30 degrees during a file acquisition (half an hour), the file is discarded as inaccurate values will be obtained. The same approach is used when ship speed changes more than 5 knots. As a result of all of the sorting described above, only a total of 612 files were used in the present analysis (about 62% of the total obtained).

Other corrections applied later to the data set, as described in the following section, involved a detailed analysis of the ship speed. As flow distortion could be introduced when the ship speed is greater than 6 knots, files obtained in such conditions are disregarded. In addition, when the ship approaches the coast, the assumption of homogeneity is violated as seen in high sea surface temperature gradients. These files were also disregarded. In total, 25 - 40 % (depending on the method applied) of the initial 1100 files obtained were suitable for the analysis.

2.3 – Results

2.3.1. Momentum fluxes

The momentum fluxes were initially calculated with the eddy correlation method and with the bulk method only, following the ideas previously described (Fig 2.3). They presented a comparable order of magnitude. Note that we use in our comparisons the momentum fluxes per unit density $u_*^2 = \tau / \rho$, with its correspondent magnitude m^2 / s^2. The Drag coefficients were also calculated (Fig 2.4), and plotted against the neutral, normalized wind speed (U_{10N}), using the stability functions as described in Donelan (1990).

We can observe a remarkable scatter of the measurements, highly unusual if compared with previous experiments (see Drennan et al. 1999; Donelan, 1990; Donelan et al., 1997; Smith, 1980; Large and Pond, 1981; Garratt, 1977). Such scatter suggests the

presence of some other agent different from winds that can be modifying the fluxes, as for example swell, wave breaking, etc. The dashed line indicates the classical results of Smith (1980) and the dash-dotted line the results from Large and Pond (1981). The main difference resides in the initial value (zero wind speed), that is 0.49 (all for $10^3 C_D$) for Large and Pond, 0.61 for Smith, and a significantly negative value for our case. The bias could be the consequence of flow distortion caused by the distribution of the containers near the tower (Fig 2.5), or the apparently extreme swell present during the experiment caused by the storm passing the area around June 21st. In the case of strong swell, the MO theory and the logarithmic laws assumed to calculate the fluxes and the drag coefficients are no longer valid (Drennan et al., 1999). However, the same type of values were obtained after the storm past, leading to the idea that flow distortion would be responsible for such unusual values.

Flow distortion can also be noticed in the dependency of the drag coefficients on the relative angle between the incoming wind and the ship bow. Figure 2.4 distinguishes the C_D values grouped according to the flow angle with respect to the bow. We distinguish between angles smaller than 30° (*), between 30° and 60° (+), and for more than 60° (dots). There is also a distinction between the wind flow coming from the port side of the ship (negative angles, indicated by a circle), or the starboard side (positive angles, without circle).

Drag coefficients are usually positive values, associated with downward fluxes (towards the ocean surface). In an effort to understand the reason for the abnormal quantity of negative values, some of the files were grouped according to both date and

wind condition forming clusters that were individually analyzed (Fig 2.6). Such clusters were chosen to represent stationary conditions. For each group, the time series, covariance and cospectra of the turbulent fluctuations were meticulously screened (see Fig. 2.7.a for an example of good data, and Fig 2.7.b for an example that needed to be excluded from the calculations). The first panel shows the cumulative sum of the covariance of the humidity and the vertical velocities, the second column, same row, is the cumulative sum of the covariance between the velocity components. The 3rd panel shows the humidity spectra and the 4th, the spectra of the vertical component of velocity fluctuations. Files where the stationarity condition is violated (changing slope in the first (or second) panel or where extreme swell influences the spectra of the turbulent fluctuations (with exaggerated peaks in the lower frequencies, as observed in the last panel), were discarded (Fig. 2.7, b). As a result of this screening, the remaining quantity of files to be analyzed was 471.

Note that a consequence of the MO theory is that the velocity spectra follow some universal shape if scaled in a proper manner, for certain frequencies (Drennan et al., 1999). Many efforts have been concentrated in trying to determine the universal forms, and today different alternatives exist, and are discussed in detail in Drennan et al. (1999). The spectra of Miyake et al. (1970) based on near-neutral data over the coastal sea demonstrate universality over the ocean, and has been broadly used. For more details in the universal Miyake scaling, see Drennan et al. (1999). We assumed that the residual negative values of momentum fluxes were obviously the result of the strong flow distortion present in this experiment. While negative fluxes have been observed in the past, they occur in very light wind conditions (Drennan et al., 1999). The flow distortion

effect was noted to affect primarily the frequencies between 0.1 and 0.25 Hz, that is the frequencies in the peak of the surface wave band. Turbulent energy at these frequencies was seen to be significantly higher than expected based on universal scaling. To smooth or avoid the flow distortion effect, the spectra within this frequency range were filtered out, by setting them to zero (Fig 2.8, a). From this point on, the fluxes or coefficients calculated with the EC are actually calculated through this modified version of EC described above. For the sake of simplicity, we will only call it EC. The final values of C_D calculated following the EC (and ID) method, appear in Fig. 2.14.

Due to the evident presence of flow distortion, and since the quantity of files at this point was greatly reduced, the ID method was also applied, following the considerations presented in section **2.1.2**. The spectra of the horizontal component of wind and humidity turbulent fluctuations were calculated to determine their Inertial Subrange (ISR) for each file (Fig. 2.9). Then the TKEDR were determined according to equation (2.7), giving values comparable to previous work, as for example Högström (1990). The resulting values of Momentum fluxes and Drag coefficients are presented in Figure 2.10 and 2.11 respectively, giving results more in agreement with previous works than the ones obtained through the other methods. Figure 2.11 presents also the results from Smith (1980) and Large and Pond (1981) in comparison with the best fit to our data. Note that our results include an 8% reduction in the mean wind speed to account for mean flow distortion, as discussed in Edson et al. (1998). There are some discrepancies between the slopes, but the order of magnitude of the results shows a good agreement.

Figure 2.12 presents the stability parameter ($\zeta = z/L$) values for the dates analyzed (panel a,b), together with a comparison to the sea surface temperature (SST)

and the air temperature (Ta), in panel 'c'. Setting the limit $\zeta = 0.5$, the values of C_D considered unstable are presented with circles in Figure 2.13 a). The same analysis, but for a limit of $\zeta > -1$ is presented in Figure 2.13 b). The implications of this result are presented in section **2.4.**

Fig 2.14 presents a comparison of the momentum fluxes per unit density calculated by the 3 methods, showing the agreement in the order of magnitude. Fig. 2.15 presents a comparison of the Drag Coefficient for the ID and the modified EC methods, The higher EC coefficients correspond to days of lower winds, as can be observe in Fig. 2.6 , pointing out the ineffectiveness of the EC method in our case (see section **2.4**), due to flow distortion.

2.3.2. Humidity fluxes

Humidity fluxes were also calculated with the Eddy Correlation and Bulk method, as for the Momentum fluxes (Fig. 2.16). The quantity of files utilized were about 30% of the total used to calculate the momentum fluxes, as accurate wind speed measurements and variability are less difficult to obtain than humidity fluctuations. This is due to the sensibility of the instrumentation to stormy weather (sea spray), fog and rainy conditions. Note that Figure 2.16 corresponds to the first stage of this analysis, that is, before ruling out the files due to changing ship speed, or relative angles to the bow greater than 30 degrees, etc.

Figure 2.16 shows both curves (for EC and Bulk from Smith, 1980) with similar variability throughout the experiment. Most of the discrepancy appears at low winds, where the fluxes calculated through the Bulk method are higher than the ones obtained through the EC method. The opposite occurs for high and/or highly variable winds.

The Dalton coefficients (C_E) calculated by means of equation (2.12), with $\overline{wq}$ calculated from the EC method show no dependency on wind speed (Fig 2.17), as previously shown by Smith (1980), Sahlee et al. (2008), Drennan et al (2007), DeCosmo et al. (1996). Figure 2.17 also shows that the scatter is somehow more evident for low winds, and that the EC calculations are limited by the sensors' capabilities in high wind days.

For the ID method, the humidity dissipation rates were calculated from the turbulent spectra, as in equation (2.8) using (2.7), the humidity fluxes from equation (2.10) and the Dalton numbers from (2.12). The Dalton coefficients calculated through the ID method appear in Fig. 2.18, in function of time (a), and in function of the normalized wind speed (b). The dotted line represents the mean Bulk value obtained from the HEXOS experiment (De Cosmo et al., 1996).

Also a classification of the C_{EN} in function of the stability parameter was made, and plotted in Fig. 2.19 versus time. The very unstable ($\zeta = z/L < -1$) values are represented by dots, the plus signs (+) represent unstable ($-1 < \zeta < -0.2$) conditions, circles represents neutral ($-0.2 < \zeta < -0.1$) conditions and asterisks are stable ($\zeta = z/L > -0.1$). The meaning of these values is discussed in the next section.

2.4. – Discussion

The influence of flow distortion in the turbulent flux calculations for this experiment was more drastic than in other experiments of this type. Such influence was evident in the momentum fluxes calculated with the EC method, as shown in Figure 2.4. Indeed, drag coefficients are usually positive values, associated with downward fluxes (towards the ocean surface) while half of our measures were negative values. Also, since the EC method based on the covariance of the wind components, it is more susceptible to include flow distortion effects that could not be cleanly filtered out due to its non-stationary character. Indeed, as evident in Fig 2.8, u and w are distorted in such a way that the covariance between the two is affected. Hence it is impossible to use the EC method reliably.

The ID method is not affected by the turbulent distortion, since it is based on the spectra of only one component of the wind and not on the cospectra. In addition, the frequencies forming part of the ISR (Fig 2.9) are different from the ones disturbed by flow distortion observed in Fig 2.8, which actually coincides with the ship motion.

Flow distortion in the mean wind speed has been already accounted for by several authors, with similar results (Dupuis et al., 2003, Edson et al., 1998, Oost et al., 1994; Pedreros et al., 2003; Popinet et al., 2004). To account for the mean flow distortion, we reduced the mean wind speed by 8% as in Edson et al. (1998). This helps to give drag coefficient values more in agreement with previous results, disregarding the method applied.

In previous studies it was possible to establish that drag coefficient values are increasing linearly with U for winds between 4 and 10 m/s (Smith 1980) with a mean value of $10^3 C_D$ of around 1.14 (Large and Pond, 1981). In our case, the values are highly scattered for wind under 5 m/s and reach a more stable value at around 10 m/s. In addition our values of C_D are somewhat smaller than the typical values of other experiments for low winds (Fig. 2.11). Still, the C_D calculated with the ID method, are very well comparable to other works, as for example the Greenland Flow Distortion Experiment-GFDex (Peterson and Renfrew, 2009) presented in Fig 2.11.

Another effect that is probably included in our calculations, is the swell derived from the incoming storm of June 22nd. In the case of strong swell, the MO theory and the logarithmic laws assumed to calculate the fluxes and the drag coefficients are no longer valid (Drennan et al., 1999). The presence of swell is usually related to extremely high peaks in the energy spectra that overpass the normal value of the rest of the spectrum, similar to the ones that can be observed in Fig. 2.7. These spectral characteristics make us suspect the presence of strong swell in the measurements.

A study of the stability conditions during the experiment was also performed by calculating the stability parameter and comparing it with sea surface temperature and air temperature. It is expected that the dates when that temperature difference is maximum, the columns would be more unstable, but that is in case the wind is minimum. But L is also influenced by the wind speed, so there are many parameters to take into account. We can observe that most of the experiment was conducted in conditions of 'unstability', and that the limit of z/L was higher than the normal value. Indeed, usually $|z/L| < 0.1$ is

accepted as a limit to neutral conditions (Donelan, 1990; Drennan, 2006), while here we used 0.5, or even 1 as a probably limit (Figures 2.12, 2.13), meaning that our experiment was mainly in 'unstable' conditions. Note that when the correction for stability is large, the momentum fluxes (and coefficients) calculation is no longer trustable, as the hypothesis assumed in the Monin-Obukhov theory are not longer valid. This implies that the C_D (and C_E) marked as 'unstable' have larger errors than the ones marked as 'neutral' or 'stable'.

The humidity fluxes calculated with the ID method are in good agreement with previous calculations such as the one from HEXOS (DeCosmo et al., 1996). The ID method allows us to perform calculations of turbulent fluxes and Dalton coefficients in high winds that were impossible to obtain with the EC method during MAP because of flow distortion.

2.5. – Summary and Conclusions

Air-sea turbulent fluxes during a phytoplankton bloom occurring during summer 2006 in the North Atlantic were measured on board the R/V Celtic Explorer. This data set was obtained during the MAP experiment, a project aimed to understand the relationships between aerosol production, surface processes and near surface turbulence. The flux tower installed in the R/V Celtic Explorer allowed a 20 Hz collection of several meteorological variables (including wind speed and direction, sound speed, humidity and

CO2 concentrations) that allow the calculation of turbulent fluxes, through the Eddy-Correlation (EC), the Bulk, and the Inertial Dissipation (ID) methods.

The strong wind variability observed during the experiment and some days of sustained high wind speed (> 20 m/s) allowed the obtaining of new information about the non-dimensional bulk coefficients for the Momentum flux. Indeed, it is observed that Drag coefficients change slightly during high winds, compared to values at low winds (about 12%) in agreement with most of the values presented by the classic work of Smith (1980), and Large and Pond (1981).

This data set presented a unique opportunity to study the effects of flow distortion caused by the structure on the Momentum flux calculation. Indeed we showed the extreme difference presented in our C_D values before and after the flow distortion correction. The frequencies most disturbed by this effect are in the range between 0.1 and 0.25 Hz.

The results of this work give insight into the surface turbulent transfer in high wind conditions and helps improving the parameterization of such transfer, by allowing a quantification of the drag and Dalton coefficients under different conditions, particularly at winds over 18 m/s.

Figures

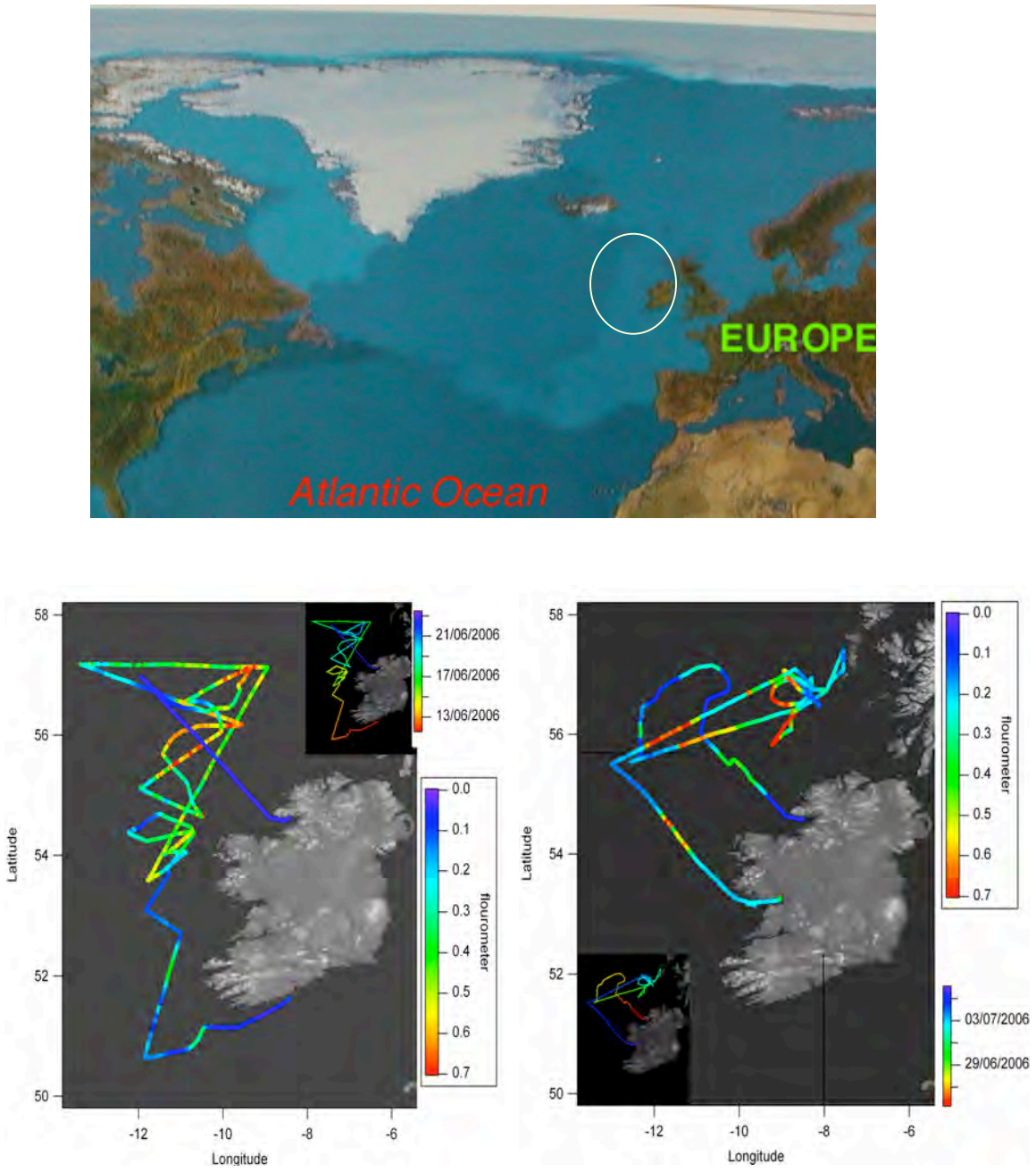

Figure 2.1: The area sampled during the MAP experiment of summer 2006 in the North Atlantic, and the path followed by the R/V Celtic Explorer. Left panel is leg 1, right panel is leg 2, divided by weather conditions (storm front).

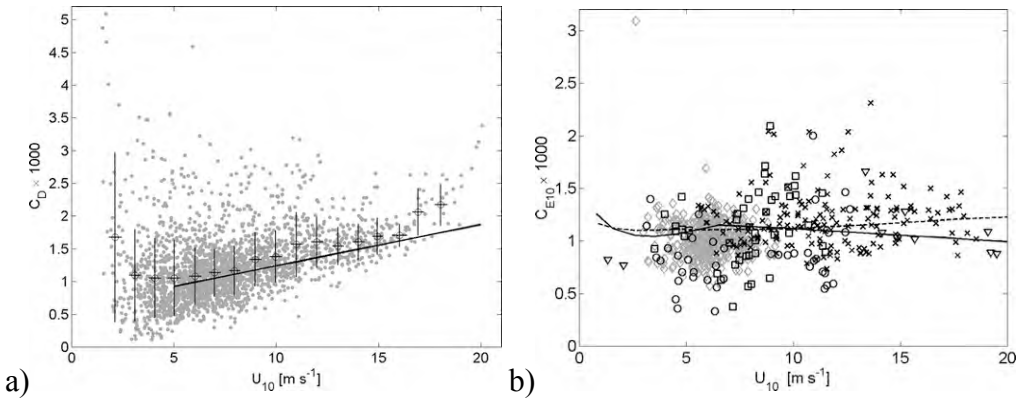

Figure 2.2. a) Drag coefficients versus wind speed at 10 m height for neutral stability from 8 different experiments using the eddy-correlation method as in Drennan et al., (2007). The solid line is from Smith (1980). The circles and thin lines show the mean and 1 standard deviation of the data in bins of 1 m/s; b) Dalton number versus wind speed at 10 m height for neutral stability from 5 field experiments using the eddy-correlation method, as listed in Drennan et al. (2007). The solid curve is from Fairall et al. (1996) and the dotted curve from Fairall et al. (2003). The squares, circles, crosses, diamonds and inverted triangles denote different experiments (see Drennan et al., 2007)

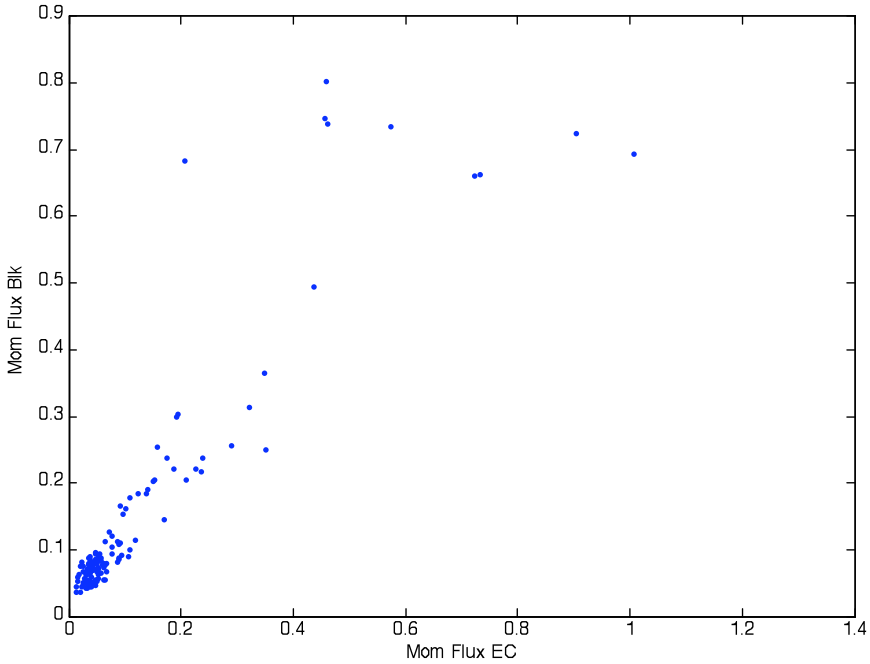

Figure 2.3. Momentum Flux (per unit of density) calculated through the eddy correlation EC and Bulk method as in (Smith, 1980).

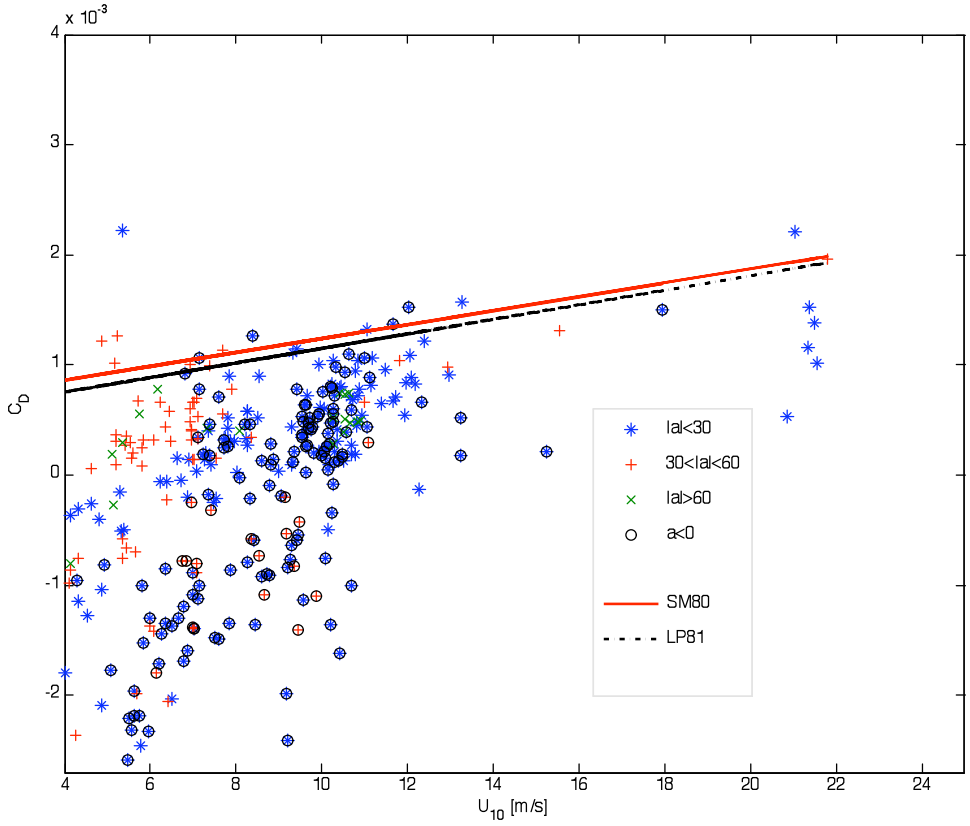

Figure 2.4. Drag coefficients (x 10^3) calculated through the EC method, versus wind speed normalized to 10 m. Signs indicate the different relative angles of wind with the ship's bow. The dashed line is the regression curve from Smith (1980), and the dash-dotted line is from Large and Pond (1981).

Figure 2.5. Distribution of instrumentation on board the R/V Celtic Explorer. Note the containers in the bow as possible source of flow distortion.

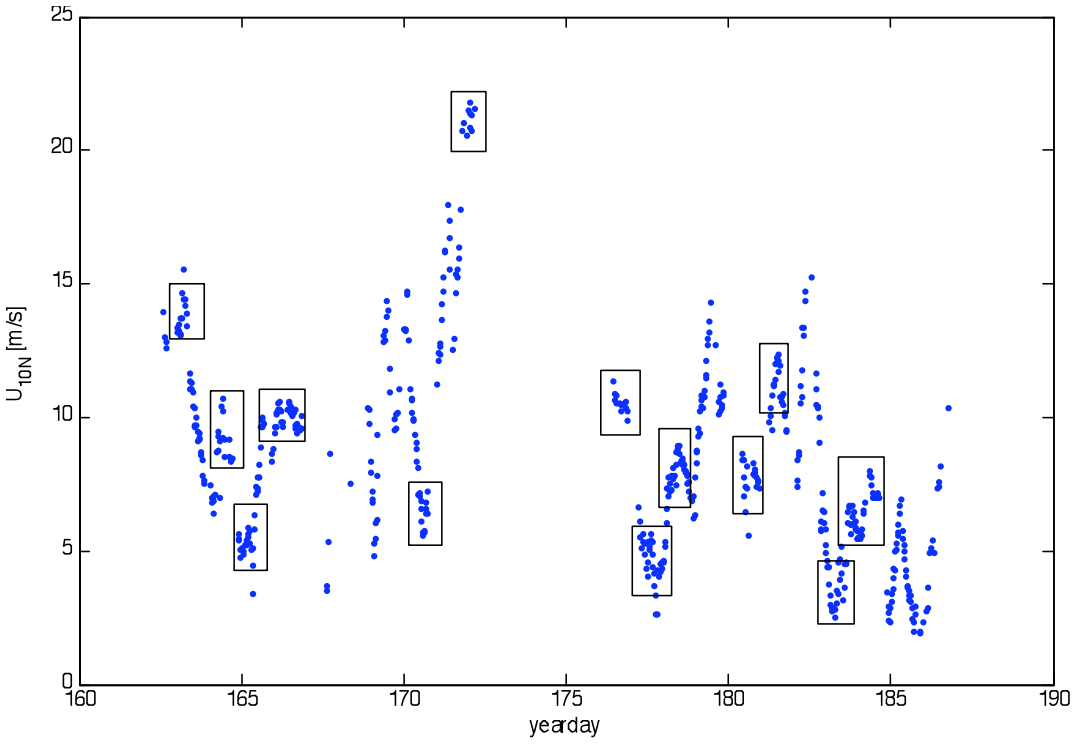

Figure 2.6. Wind speed throughout the MAP experiment, with the different groups or clusters of data indicated for further investigation.

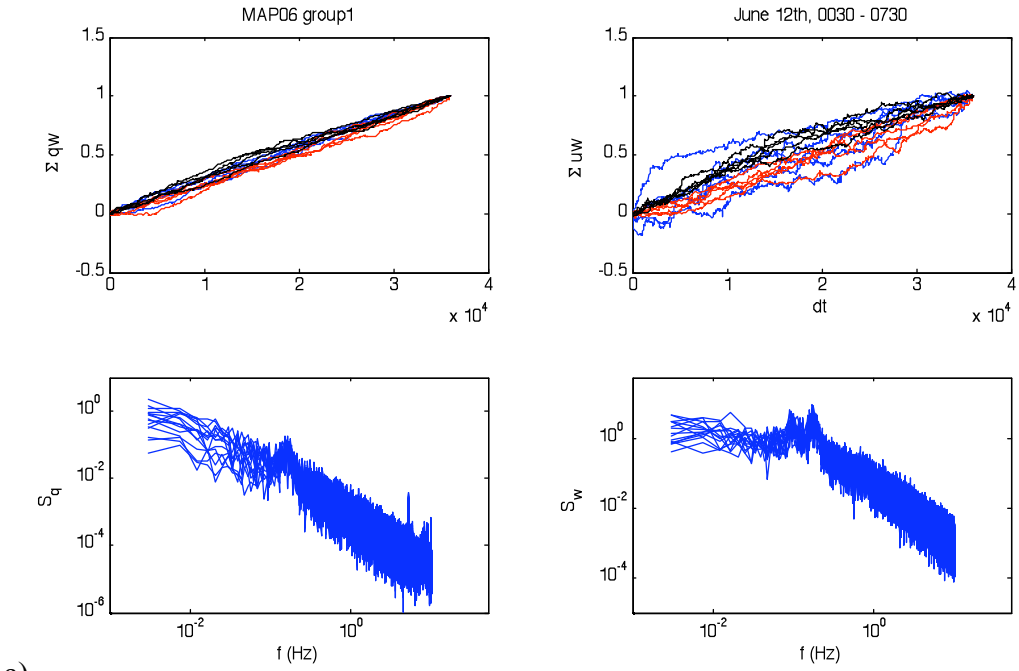

a)

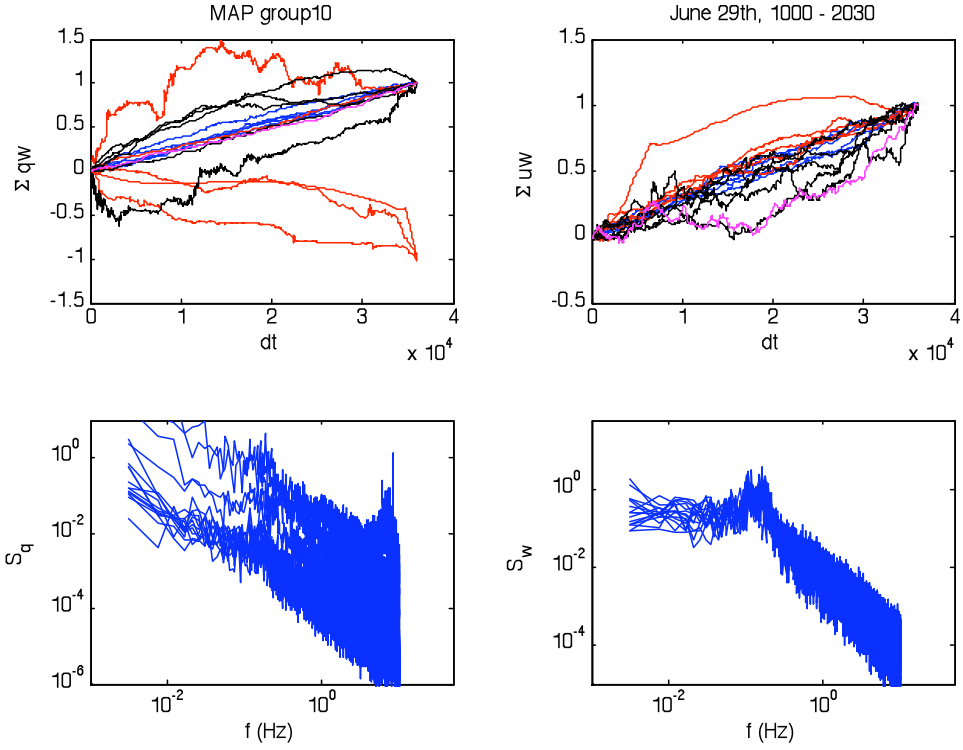

b)

Figure 2.7. Example of the groups analyzed. Top four panels (a) a good case, lower four (b) is a bad case. The upper panels are the cumulative sum of the covariance, between humidity and vertical velocity (left) and between velocities components u and w (right). Values of the upper panels have been normalized to 1. Lower left panel is the humidity spectra, and lower right is the vertical velocity spectra.

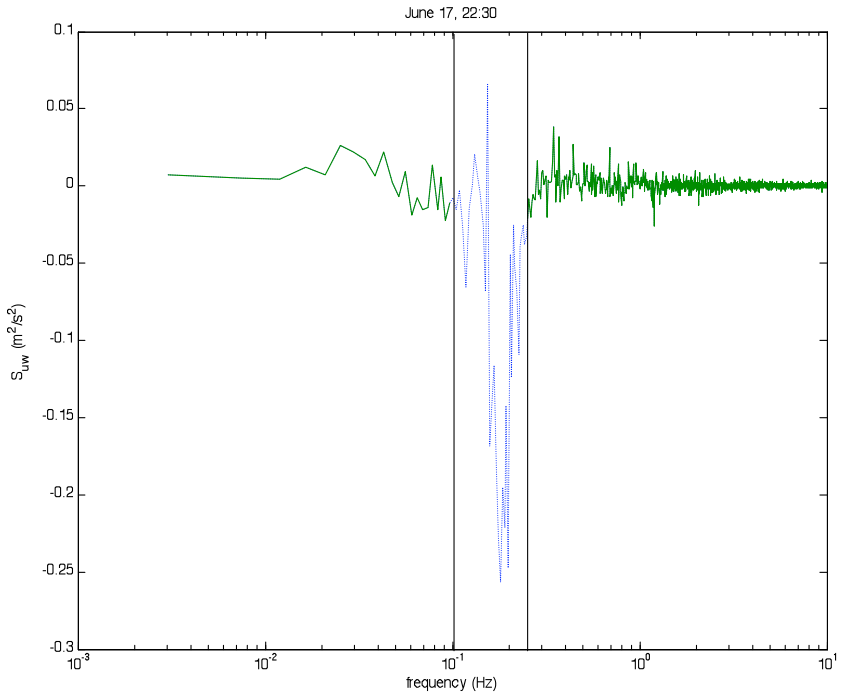

Figure 2.8. Example of velocity fluctuations spectrum for the day June 17th at 22:30. The portion of dashed line spectrum between the vertical lines is assumed to be due to flow distortion and the filtered out during the analysis (modified eddy correlation method, described in the text).

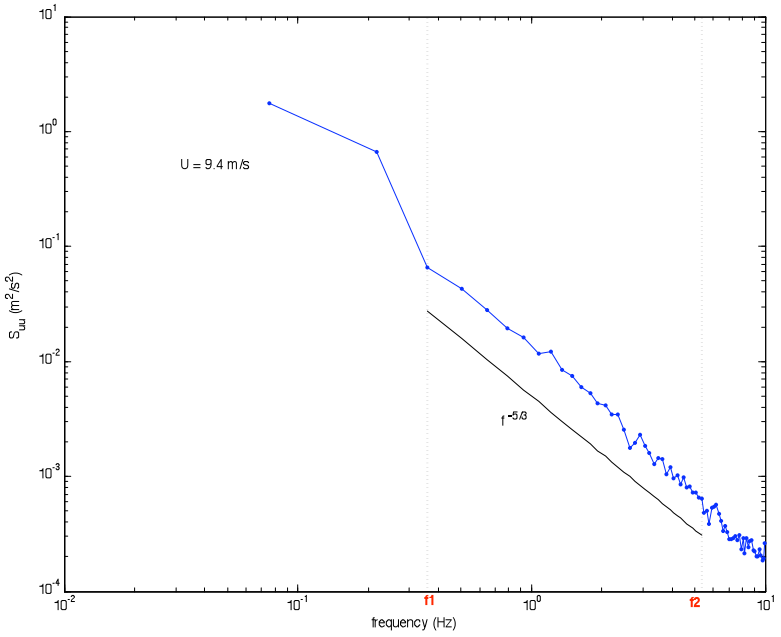

Figure 2.9. Spectrum of the horizontal velocity fluctuations for June 12th at 16:00, and the definition of ISR, bounded by the frequencies f1 and f2. The mean wind speed observed for this case is 9.4 m/s.

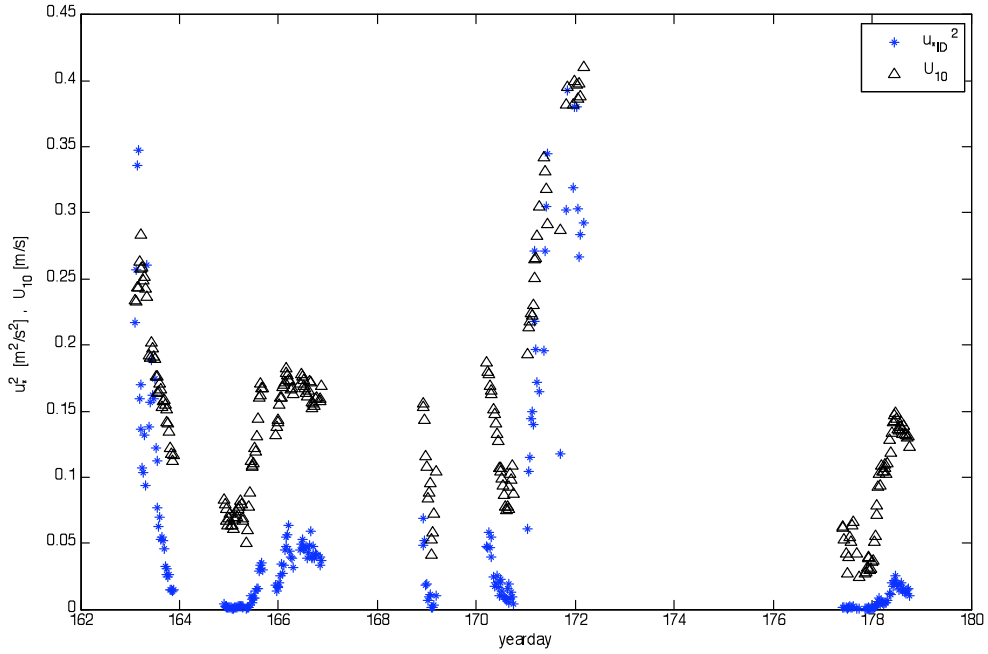

Figure 2.10. Momentum fluxes ID (inertial dissipation method) per unit of density (asterisks) and mean wind speed U_{10N} (triangles) as a function of time.

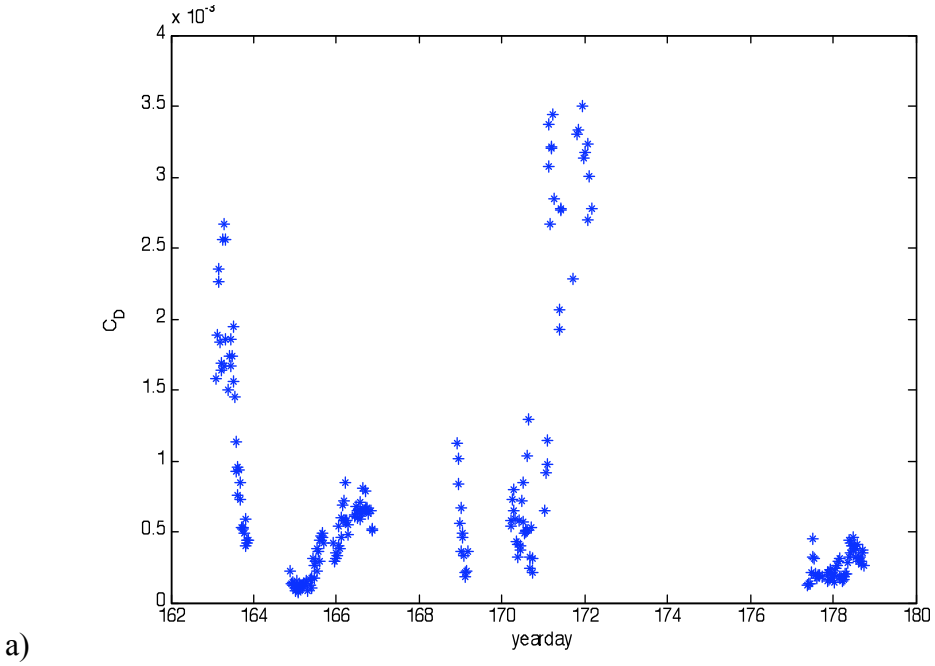

a)

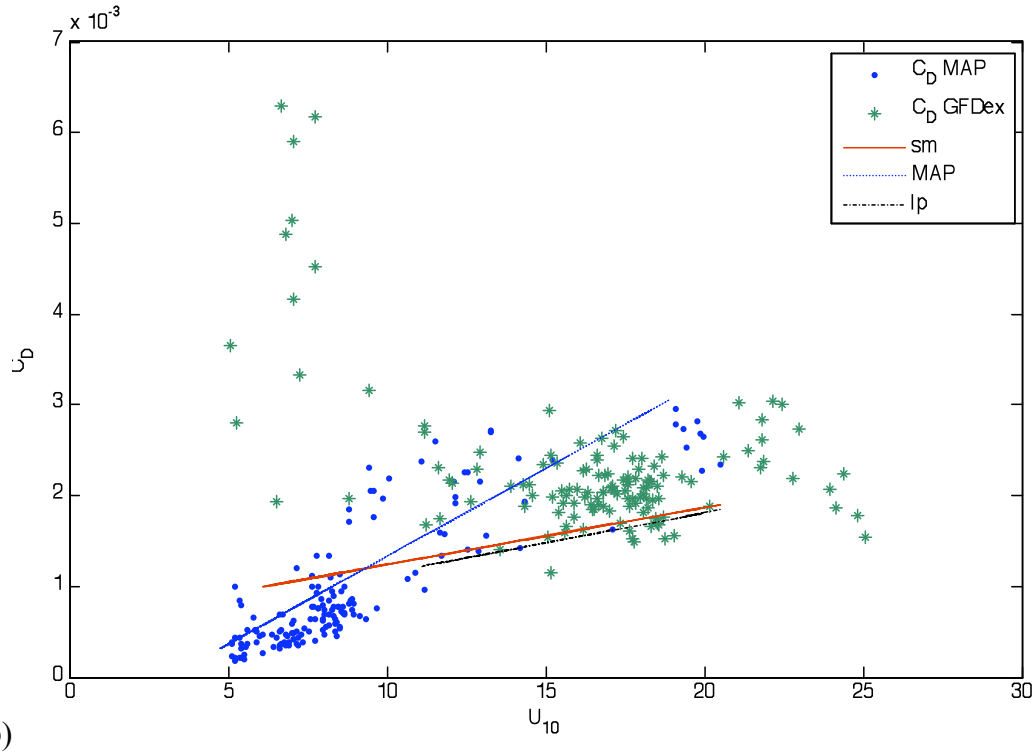

b)

Figure 2.11. Drag coefficients (10m neutral), calculated using the inertial dissipation method (ID) as function of time (a), and as function of wind speed U_{10N} (b). The MAP data is represented by dots. The dotted line is the best fit to our data, the solid line is the regression curve from Smith (1980), and the dash-dotted line is from Large and Pond (1981). Also the data from GFDex (asterisks) is presented (Peterson and Renfrew, 2009).

a)

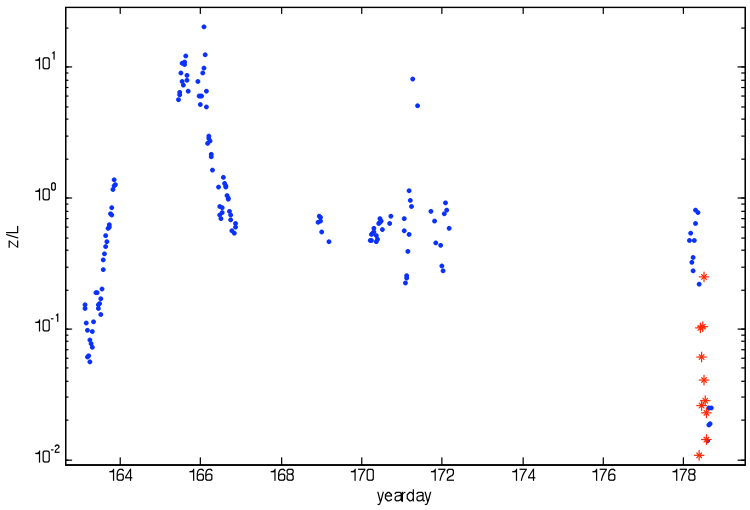

b)

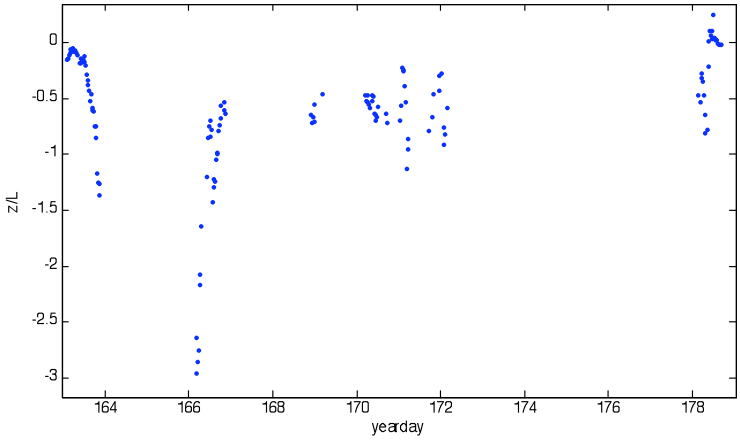

c)

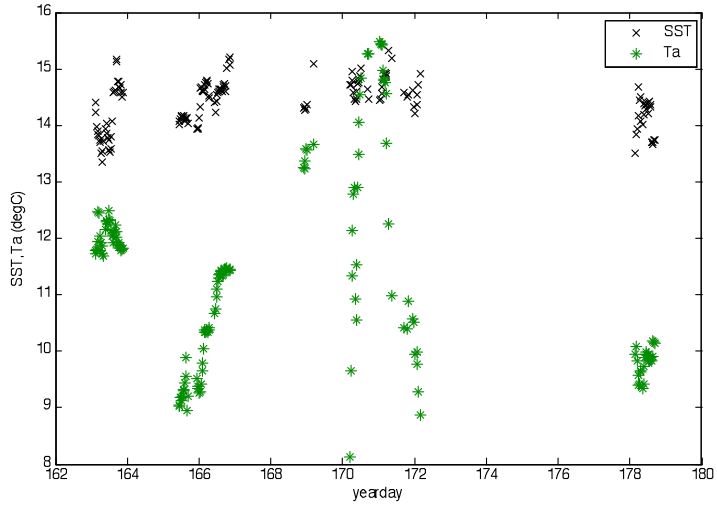

Figure 2.12. Stability parameter z/L and temperature conditions for the MAP period. a) semilog axis, dots represent –z/L, asterisks are z/L. b) linear; c) Air temperature (Ta) and Sea Surface Temperature (SST) for the days analyzed

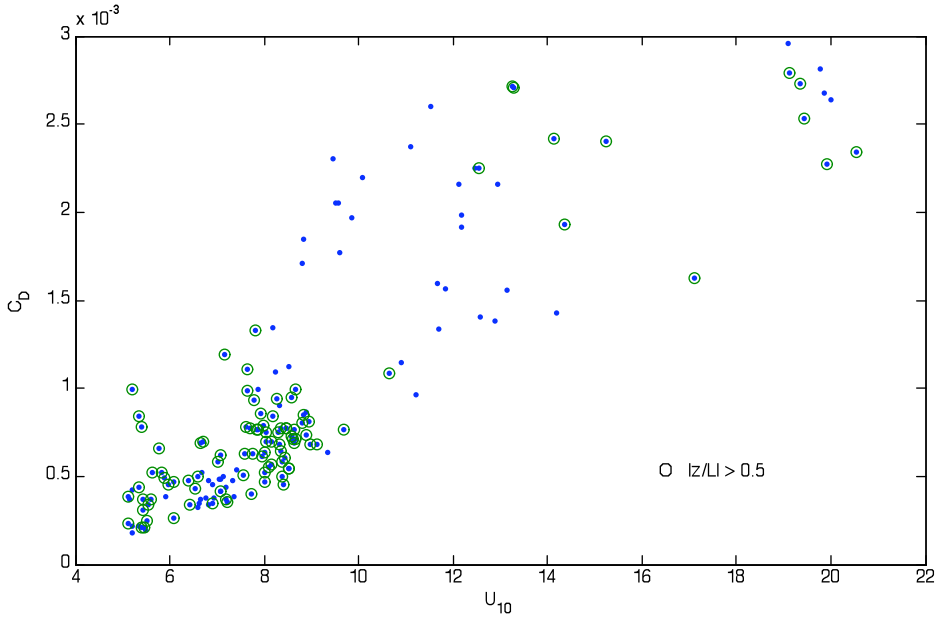

a)

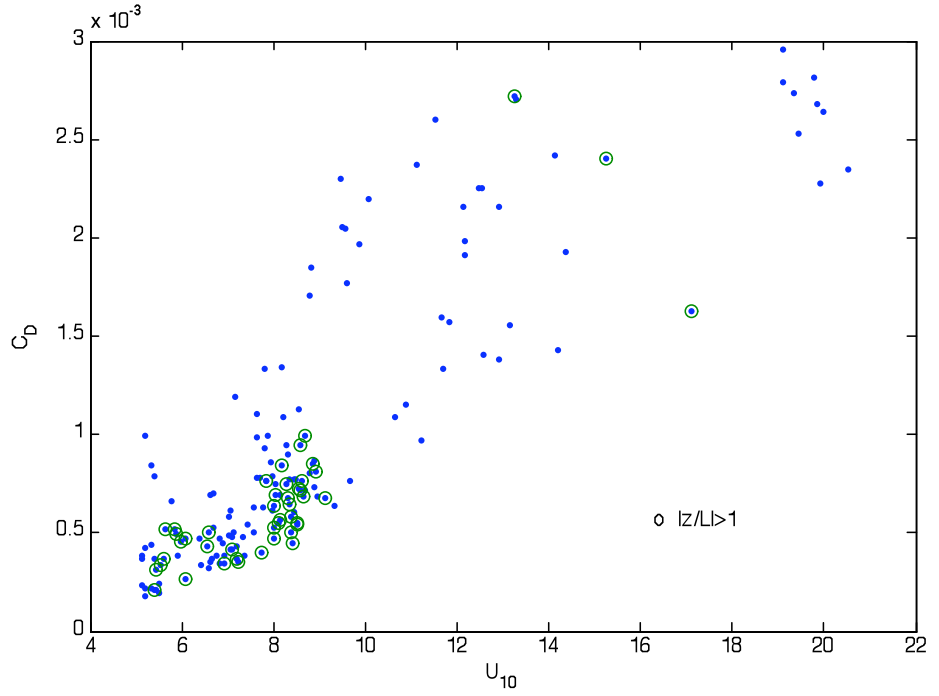

b)

Figure 2.13. Drag coefficients ID (10m, neutral, using inertial dissipation) as function of wind speed U_{10}, showing a)| z /L| > 0.5, and (b) |z / L| > 1

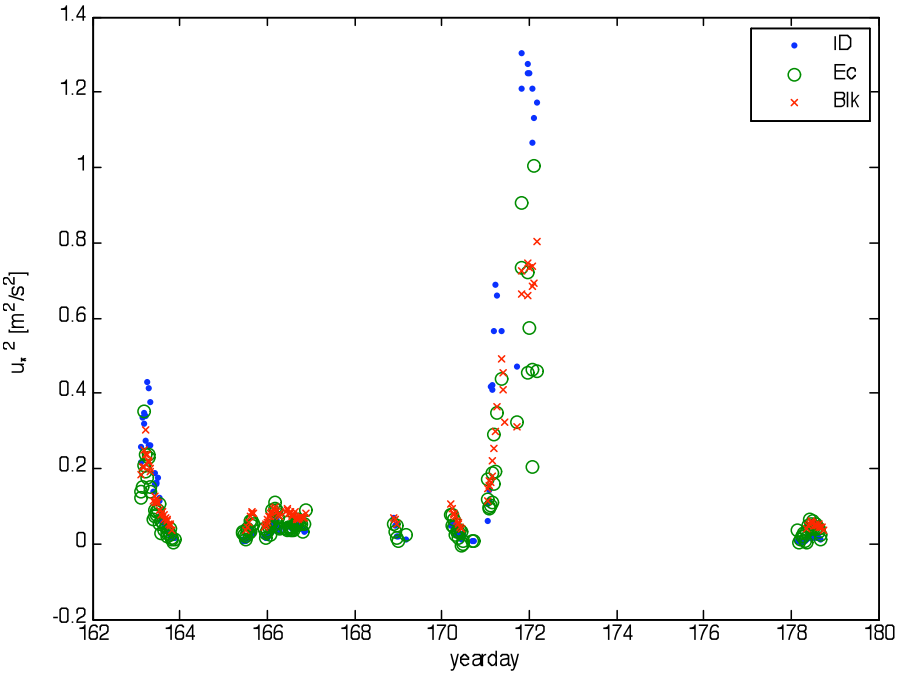

Figure 2.14. Momentum fluxes (per unit of density) comparison between the 3 methods, Eddy Correlation (EC) modified, Inertial Dissipation (ID) and Bulk (Blk) in function of time.

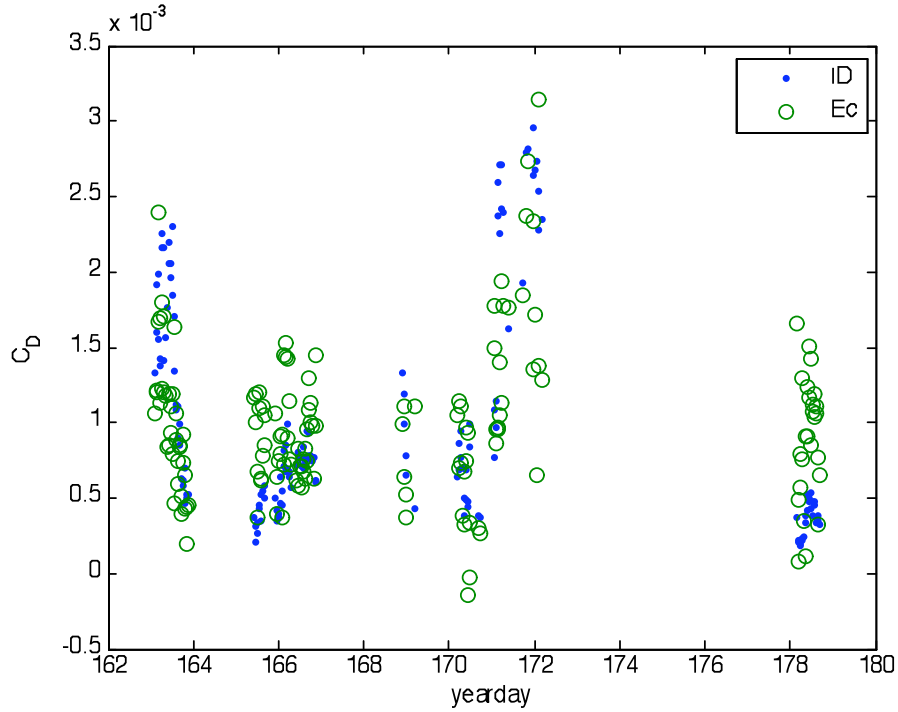

Figure 2.15. Drag coefficients calculated with the Inertial Dissipation (ID) and modified Eddy Correlation (EC) methods as a function of time.

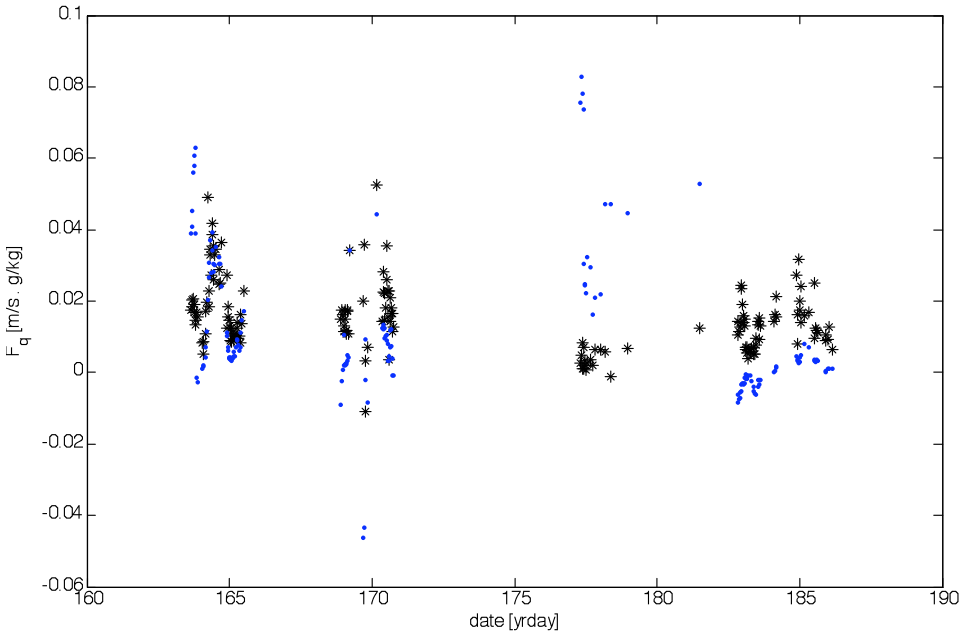

Figure 2.16. Humidity fluxes calculated through the Eddy Correlation (EC,dots) and Bulk methods (as in Smith, 1980 - asterisks) versus time.

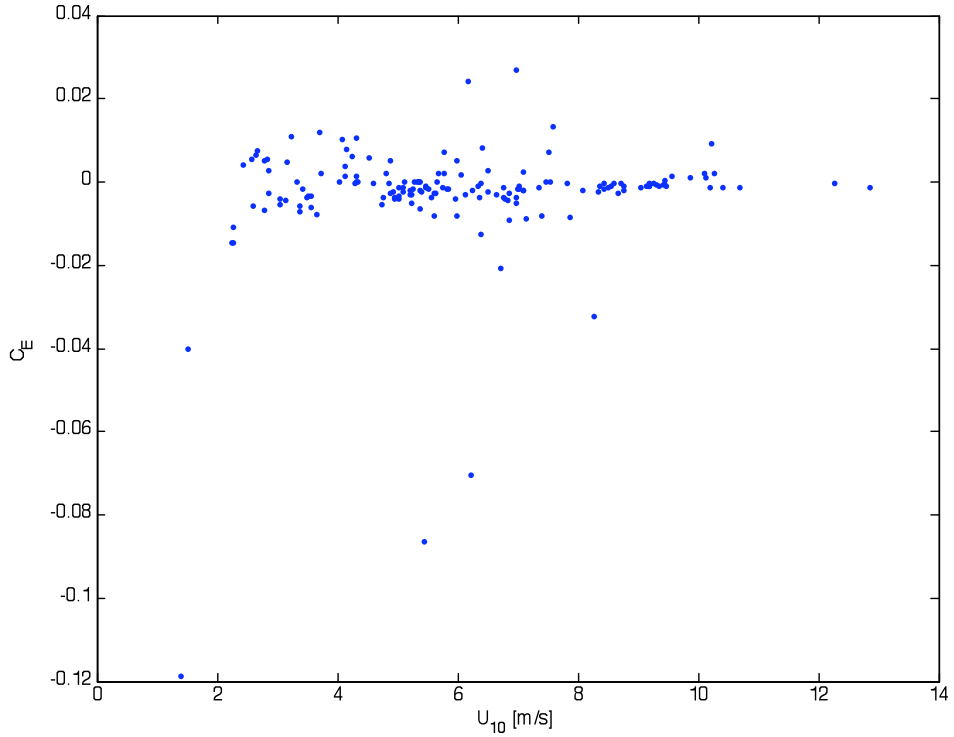

Figure 2.17. Dalton coefficients (C_E , 10m neutral) with the Eddy Correlation method versus wind speed U_{10N}

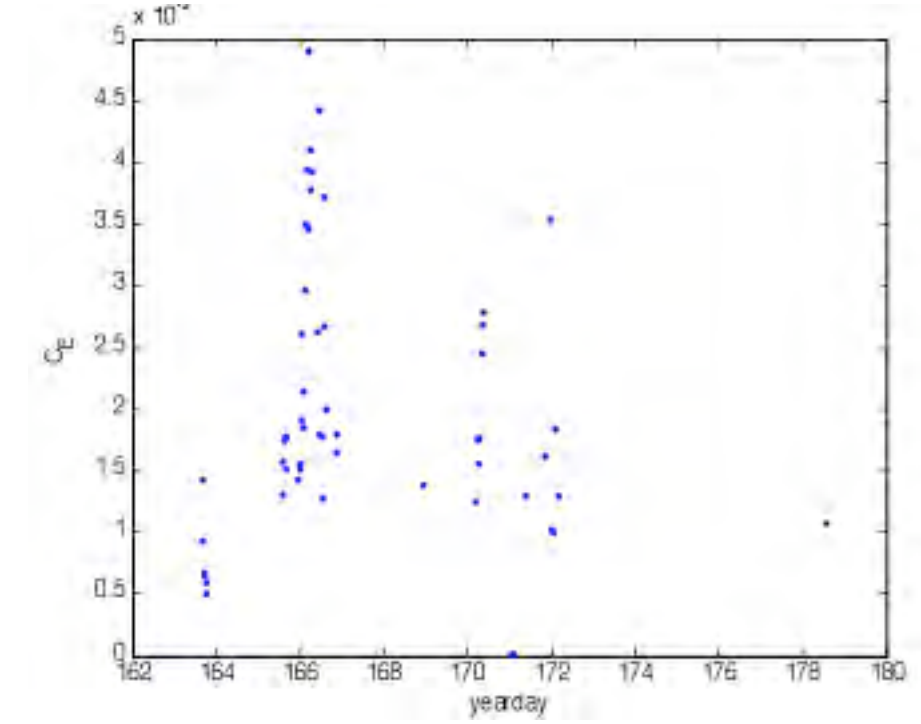

a)

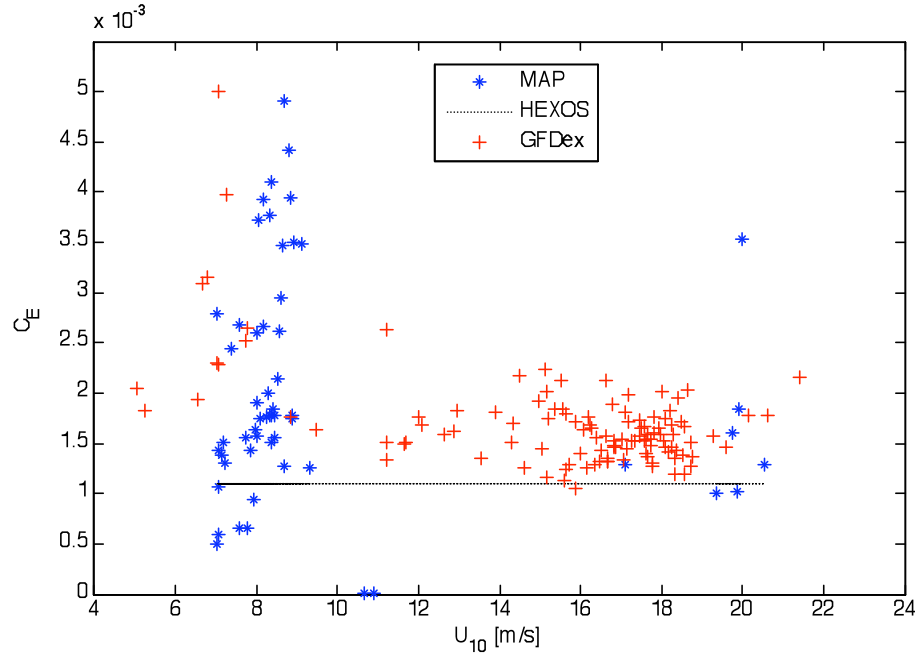

b)

Figure 2.18. Dalton coefficients calculated through the Inertial Dissipation (ID) method in function of time (a) and in function of the normalized wind speed (b). The dotted line represents the Bulk value obtained from the HEXOS experiment (De Cosmo et al., 1996). GFDex data from Petersen and Renfrew (2009).

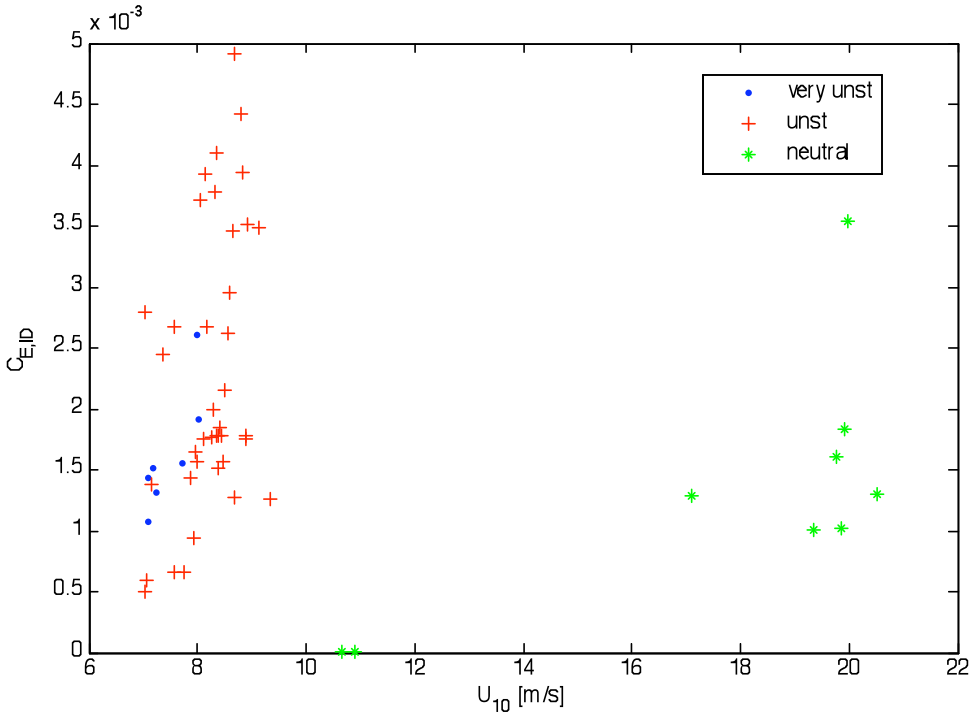

Figure 2.19. Dalton coefficients (10m neutral, via inertial dissipation method) versus wind speed differentiated by the stability parameter: very unstable (z/L< -1) represented by dots, (+) represent unstable (z/L<-1 to -0.2.), circles is neutral (z/L<-0.2 to -0.1) and stable (z/L> -0.1) is asterisks

Chapter 3

Pulse-to-pulse coherent Doppler sonar: description and signal interpretation.

3.1 – Introductory remarks

Ocean surface boundary layer analysis involves small and micro scale events. At the surface the transfer of scalar properties between the air and the ocean occurs within a very thin sublayer (20-200 μm) and comprises mainly molecular diffusive processes. Below it, in the first few meters of the ocean, turbulent effects mainly related to winds and wave breaking, rule the transfer of properties (Jähne and Haußecker, 1998; Lorke and Peeters, 2006).

Turbulence is usually defined as an energetic, rotational and eddying type of motion that transports material and transforms momentum at higher rates than molecular processes (Thorpe, 2004). Turbulence then constitutes the most effective driver of air-sea fluxes. Conventionally, turbulence is quantified by the change in the time it takes for the turbulent energy to be dissipated in the ocean, and is called Turbulent Kinetic Energy Dissipation Rate (TKEDR, from now on), usually denoted by ε (Thorpe, 2004; Gargett, 1999). Its units are m^2/s^3 or W/kg and typical values range from $10^{-10}\, m^2/s^3$ in the ocean interior to $10^{-1}\, m^2/s^3$ in the most active regions: rapid tidal currents, surf zone, and the surface boundary layer (Thorpe, 2004). It is this loss of energy to dissipation at the ocean surface that really stirs the upper ocean column, allowing the transfer of gas (Lamont and Scott, 1970; Zappa, 2007). Surface wave breaking and Langmuir circulations are prime candidates for the source of anomalously high TKEDR in the near-

surface ocean boundary layer (Gargett, 1989). Non-breaking wave-induced turbulence may also play a role (Babanin and Haus, 2009).

The equation for ε can be derived from the turbulent kinetic energy budget:

$$\frac{De}{Dt} = -\overline{u'w'}\frac{\partial \bar{u}}{\partial z} - \overline{v'w'}\frac{\partial \bar{v}}{\partial z} + \frac{g}{\bar{\theta}}\overline{w'\theta'} + 0.61\,g\,\overline{w'q'} - \frac{\partial}{\partial z}\overline{w'e} - \frac{1}{\rho}\frac{\partial}{\partial z}\overline{w'p'} - \varepsilon \qquad (3.1.1)$$

where e is the turbulent kinetic energy (TKE), defined as $e = 1/2\,(u'^2 + v'^2 + w'^2)^{1/2}$, and ε is the dissipation rate of turbulent kinetic energy. Prime denotes turbulent fluctuations, but we will use $u_i = u_i'$ from now. The left hand side of equation (3.1.1) is the total derivative, and so includes the local change and the horizontal advection terms. On the right hand side, the first and second terms together are the shear production, the third term and fourth terms together are the buoyancy production, the fifth term is the turbulent transport of TKE, the sixth term is the pressure transport, and the last term is the dissipation. An examination of the terms in the turbulent kinetic energy equation aids our understanding of the nature of turbulent production and destruction in the surface boundary layer (Gerbi et al., 2009; Kraus and Businger, 1994).

ε acts to reduce the energy of the flow, and is defined as a function of the strain tensor:

$$\varepsilon = -2\nu\left\langle S_{ij}\ S_{ji}\right\rangle = \nu\left[\left\langle \frac{\partial u_i}{\partial x_j}\frac{\partial u_i}{\partial x_j}\right\rangle + \left\langle \frac{\partial u_i}{\partial x_j}\frac{\partial u_j}{\partial x_i}\right\rangle\right] \qquad (3.1.2)$$

where ν is kinematic viscosity , S is the strain tensor and the brackets indicate a suitable temporal average. Invoking homogeneity, equation 3.1.2 becomes:

$$\varepsilon = \nu \left[\left\langle \frac{\partial u_i}{\partial x_j} \frac{\partial u_i}{\partial x_j} \right\rangle \right] \tag{3.1.3}$$

and by assuming a locally isotropic flow, the previous equation transforms to

$$\varepsilon = \left\langle 15\nu \overline{\left(\frac{\partial u_i}{\partial x_i} \right)^2} \right\rangle \tag{3.1.4}$$

where 15 is an empirical coefficient (Veron and Melville, 1999).

The importance of obtaining accurate TKE dissipation rates close to the surface resides in that turbulent air-sea fluxes and gas velocity transfer can be parameterized in terms of these rates, rather than in terms of the turbulence-generation mechanism (as breaking waves, wind shear, Langmuir circulation, etc). Direct measurements of ε as in (3.1.4) are rare, because they involve sampling the velocity field at frequencies above 2KHz. While this has been done in the air over land (Champagne et al., 1977), such measurements have not been made in the ocean. Instead, estimates of ε have been related to lower frequency measurements in the so called Inertial Sub-range (ISR), basically 2-10 Hz. We discuss this in detail in section **3.5**. The measurements referred to here are all based on ISR data.

The flow close to boundaries in general (*i.e.* the sea surface or sediment near sea bed) exerts a stress τ on the boundary, which can be expressed in terms of a friction velocity u_* and water density ρ as $\tau = \rho u_*^2$. At distances z from a rigid boundary, and considering constant stress, the dissipation rate generally follows the Law of the Wall relation $\varepsilon = u_*^3 / K z$, where K is the von Karman constant, measured as 0.4 (Högström, 1990). At depths below the sea surface greater than the significant wave height, H_s, the dissipation rate also follows the Law of the Wall with u_* given by the wind stress on the

water side. Studies performed more than a decade ago clearly showed that the values of ε closer than H_s to the surface were higher than those calculated through the Law of the Wall relationship, because of the turbulence generated by breaking waves (Agrawal et al., 1992).

Obtaining accurate measurements near the surface is extremely hard due in part to wave motion, and is still harder to distinguish the turbulent motion from those induced by waves. Laboratory experiments and field observations help to shed some light into the problem. In laboratory experiments, Rapp and Melville (1990) demonstrated that 10% of the wave energy is lost to breaking in spilling breakers and 25% in plunging breakers. Approximately 90% of the energy released by wave breaking is dissipated by turbulence within a time equivalent to four wave periods. The rest forms a coherent 'roller' structure with comparable height to the wave height (Melville et al., 2002).

Terray et al. (1996) proposed a parameterization of the production of energy within the upper ocean by wave breaking, using the energy input from wind waves (F). They scaled the upper layer dissipation under breaking wave conditions as

$$\frac{\varepsilon H_s}{F} = f(z/H_s, c_p/u_{*a}) \tag{3.1.5}$$

where f is a function determined from the data, and the conventional definition of wave age in terms of the air-side friction velocity was used. However, for intermediate depths, they stated that (3.1.5) reduced to $\varepsilon H_s / F = f(z/H_s)$ that is valid only close to the surface (Terray et al., 1996). The rate of energy input to the waves F is defined as

$$F = g\int \frac{\partial S_\eta}{\partial t} d\omega\, d\theta = g\int \beta S_\eta\, d\omega\, d\theta \tag{3.1.6}$$

where $S_\eta(\omega,\theta)$ is the frequency-direction spectrum of the waves. They defined an "effective phase speed", $\bar{c}$, related to wind input by parameterizing F in terms of this speed and the wind stress τ_a as

$$F \equiv \tau_a \bar{c} / \rho_w \approx u_{*w}^2 \bar{c} \qquad (3.1.7)$$

Gemmrich and Farmer (1999) suggested adding to the previous formulation the local rate of input energy from the wind to the wave field. By using a short average period (1 sec), they were able to separate the turbulent enhancement due to active wave breaking from the dissipation related to the decaying wave-induced turbulence and shear stresses. The TKEDR calculated were several hundred times larger than those predicted by the law-of-the-wall, but lasting for a very short period. The maximum dissipation at 1m depth is estimated to be $\varepsilon_{\max} = 0.2\, m^2 s^{-3}$ based in the consideration that $\varepsilon \propto t^n$ is the decay of wave-induced turbulence. They found the bounds for the decay rate to be $-4.3 < n < -2.9$ consistent with $n = -17/4$ predicted for isotropic turbulence.

Also, Babanin (2006) and Babanin and Haus (2009) studied near surface wave induced turbulence through tank experiments. They calculated the wavenumber velocity spectra beneath monochromatic nonbreaking unforced waves. They quantified the TKEDR as a function of surface wave amplitude, and proposed that the isotropic turbulence associated with these motions can affect the dynamics of the subsurface boundary layer.

Drennan et al. (1996) confirmed the Terray et al. (1996) scaling of the dissipation rates based on wind and waves parameters by applying the concepts to open ocean data. Very close to the surface, the dissipation rates are at least one order of magnitude larger than those predicted by the Law of the Wall theory. Underneath it, there is an

intermediate region where ε is inversely proportional to the square of depth ($\varepsilon \propto z^{-2}$). The last region shows values of dissipation asymptotically reaching the traditional wall layer predictions.

Large-scale coherent flow structures need also to be taken into account when studying the surface ocean boundary layer. The dynamical importance of the accumulation of debris in parallel structures at the ocean surface was first studied by Langmuir (1938). These bands, often composed of foam, are typically 2-300 m apart and can be 3-10 times larger in length (Thorpe, 2004). Langmuir circulation consists of a set of downwind directed vertical motions leading to windrows in convergence lines on the water surface and down-going flows beneath of about 1-20 cm/s, replenished by a weaker upward flow between the convergence lines (Thorpe, 2004). Within the down-going water below windrows, turbulent dissipation rates are found to be higher than average, maybe because of the shear and stretching of small-scale eddies by the circulation together with advection towards the area of decaying turbulence produced by breaking waves (Thorpe, 2004; Gemmrich, 2000). This effect will be explored in the next chapter.

Indirect methods involving Doppler sonar measurements are now used to estimate ε from on-board ships in coastal and shelf areas. The principle behind the method is that the energy produced by the largest turbulent eddies cascades down towards the small scale eddies at which it is dissipated. Furthermore, the rate of energy production of turbulence is equal to the dissipation rate (the basis of Kolmogorov's theory). This is usually true, except for highly stratified waters where some leakage can occur. Gargett (1999) used acoustic Doppler current profiler (ADCP) data and compared them to airfoil probe measurements to show that the dissipation rate can be parameterized by $\varepsilon = cq^3 / l$,

where q is the rms vertical velocity component measured by a vertical Doppler sonar beam and l is a vertical scale characteristic of the large eddies, determined from the sonar measurements using a zero-crossing algorithm. Her values of ε were between $10^{-5} - 10^{-6}\ m^2/s^3$.

Another method, derived by Lhormann et al. (1990) uses ADCP data to estimate the Reynolds stress and hence derive the rate of energy production. Because of the beam geometry and presence of the vessel, neither of these methods can be used to estimate ε close to the surface. Wiles et al. (2006) introduced a new technique for the estimation of ε using a standard ADCP, applying the structure function method. They detected differences between the upstream and downstream dissipation rate estimates, indicating anisotropy in stress and/or shear. The isotropy of the turbulence is a necessary assumption to apply Taylor hypothesis, a widely used approach in turbulence studies.

Kolmogorov's energy cascade theory states that there is a portion of the wavenumber spectrum where the energy is advected from the larger to the smaller eddies, without input or loss of energy, called Inertial Subrange (ISR). It can be shown through dimensional analysis that in such ISR the spectrum of the velocity fluctuations is proportional only to the wavenumber and the dissipation rate, that is, $S(k) \propto \varepsilon^{2/3} k^{-5/3}$ (Tennekes and Lumley, 1972). Taylor (1938) suggested that for some special cases turbulence might be considered to be frozen as it passes a sensor, allowing the calculation of TKEDR with frequency spectra instead of wavenumber spectra. The mean advective value of the current or wind speed (U_a) can then be used to translate turbulence measurements as a function of time to measurements as a function of space, considering $S(k)U_a \propto S(f)$ (Stull, 1988). Such a simplification is useful as most of the

instrumentation available cannot obtain measurements with the spatial resolution necessary to construct wavenumber spectra. However, it can only be applied in cases were the turbulent eddies evolve with a time scale longer than the time it takes the eddy to be advected past a sensor. The advection velocity needs to be rather large compared to the turbulent velocities, this occurs when measurements are taken on board oceanographic vessels or from a fixed platform in a strong current. Also, Taylor's hypothesis cannot be applied in presence of intermittent events such as wave breaking. However, Lumley and Terray (1983) extended this criterion to unsteady advection and showed that for deep water gravity waves, U_a could be adequately replaced by the rms of the surface waves orbital velocity provided that $U_{rms}^{orb} >> U_{turb}$.

The most widely used Doppler sonars (as mentioned previously) calculate velocity and velocity fluctuations through the shift in frequency of the backscattered signal with respect to the original signal and are called incoherent. Pulse-to-pulse coherent Doppler sonars, instead, transmit a series of identical pulses and use the phase shift in between those pulses to calculate velocities. These sonar can measure either the 3 components of velocity fluctuations (u,v,w), as the Marine Acoustic Velocimeters (MAVs) or just one of the components, the radial one in the direction of the transmitter. In the following we will describe in detail the unidirectional sonar, so called Miami DopBeam.

The pulse-to-pulse coherent unidirectional Doppler profiler is able to collect velocity information at very high sample rate (more than 400 Hz), and at densely spaced locations (0.008 m). Because of that reason, wavenumber spectra can be directly determined from the velocity series (Veron and Melville, 1999) without the need of

calculating first the frequency spectra. In this way the consideration of Taylor's or frozen turbulence hypothesis is avoided. Avoiding the use of such hypothesis has obvious advantages in regarding accuracy of the results, as explained previously.

The DopBeam was successfully tested in laboratory experiments, coastal shallow inlets and lakes (Veron and Melville, 1999; Lhermitte and Serafin, 1984; Lhermitte and Haus, 1999). The values of dissipation rates ranged from 10^{-2} to $10^{-6}\ m^2/s^3$. Also, Gemmrich and Farmer (2004) deployed a coherent sonar 150 km offshore Monterey Bay, in winds of about 10m/s. The values of dissipation rates calculated at 1 m depth were in the range of $10^{-1} - 10^{-6}\ m^2/s^3$.

There are certain limitations for the use of this coherent Doppler sonar as the backscattered signal is bounded by the availability and movement of the targets. However, previous studies together with the present work prove them to be a very effective tool in turbulence related studies.

3.2 – Physical principles of operation

The instrument considered here is a "pulse-to-pulse coherent" Doppler sonar (Fig. 3.1) in which the backscattering signal phase change associated with target motion is measured between sets of pulses. The output signal, sampled at a given time delay τ from the start of the transmitted pulse (range gated), relates to backscattering from any target located within a "backscattering volume" starting at a range $R = c\tau/2$ and whose dimensions are the beam cross section (c) and half the sonar pulse length (τ).

If the signal phase variation from pulse to pulse exceeds $\pm\pi$ ($\pm 2\pi$ if the

velocity sign is known), it is ambiguously related to target velocity. A 2π phase shift is equivalent to a $\lambda/2$ target displacement (where λ is the sonar wavelength). This means that only Doppler frequencies within $\pm f/2$ limits or radial velocities within the $\pm f\lambda/4$ domain will be unambiguously determined. Most of the work presented in this chapter is aimed at interpreting or avoiding these ambiguities in the backscattered signal. Note that the unambiguous Doppler frequency domain is f, so that if the sign of the Doppler frequency is known (approaching or receding targets) the usable domain is either 0 to f or 0 to $-f$.

In conventional Doppler sonar circuits, the difference between backscattered signal phase and the transmitted signal phase taken as reference is measured using a mixer circuit generating two orthogonal components (usually defined as I and Q signals) of a complex signal $S = I + iQ$, a procedure which preserves the frequency sign. A Fourier transform (FFT) of S yields the expression of the Doppler spectrum. The sampling rate, f controls the spectral domain ($\pm f/2$ Nyquist boundaries) and the length of the time series, T, controls the spectral resolution (1/T frequency interval between spectral lines). Doppler frequency shifts exceeding the Nyquist boundaries are aliased. The autocovariance (or pulse pair or PP) algorithms provide a better method for calculation of mean Doppler velocity which does not require prior FFT operation (Lhermitte and Serafin, 1984).

The main limiting factor of the pulse-to-pulse coherent sonar, is the opposite and conflicting influences of the pulse repetition frequency f on the maximum unambiguous range ($R_{\max} = c/2f$, where c is the velocity of sound in water), and on the maximum unambiguous velocity ($V_{\max} = \pm f\lambda/4$), essentially making it a short range instrument.

When combined these two limits yield the range-velocity function

$$R_{\max} V_{\max} \leq \pm c\lambda / 8 \qquad (3.2.1)$$

Backscattering signal intensity and target strength.

When the sonar sensitivity is set high enough as to detect weak targets, the stronger backscattering could saturate the receiver. Lhermitte and Haus (1999) used a high setting and noted that the backscattered signal had a much stronger intensity in an ebb flow compared to a flood tide as they were using this instrument in an inlet. In the open ocean it would be of interest to find out the difference in signals and velocities between approaching and receding flows (see Chapter 4).

3.3 – Technical description and details on the Miami Dopbeam

1. System description

The Dopbeam consists of two modules, a transducer module and a processor module. The transducer module consists of a 40-cm long, 6-cm diameter pressure housing with a single monostatic transducer mounted at one end and an underwater connector at the other. The transducer can be mounted with its beam pointing along the length of the housing or to the side. The housing contains the front-end electronics for driving the transducer during transmits and for amplifying and filtering the return Doppler signals. The transducer module is connected to the processor module via a waterproof (neoprene-jacket) cable with 6 twisted shielded pairs. This cable can be up to 30 m long.

The Processor module consists of a card that plugs into any 16-bit IO slot of the computer. This module contains all of the necessary electronics for controlling the operation of the system, providing the transmit power, and sampling the return signals. The signal processing required to derive Doppler velocities from the baseband complex Doppler signals can be readily implemented in the PC.

2. System frequency and bandwidths

Center Frequency ---------- 1500 kHz

Transducer Bandwidth ------ 12% of center frequency

Receiver Bandwidth ------- 9% of center frequency

Amplitude Bandwidth ----- 6% of center frequency

3. Time response/resolution

Dead Time after transmit ------- Less than 200 μs at 1.5Mhz (less than 20 cm)

Minimum pulse length ----------14 μs (1.1 cm) at 1.5MHz

Along-beam resolution ---------- 14 μs (1.1 cm) at 1.5MHz

4. Other system parameters

Maximum range ---------- Depends on frequency, volume backscattering strength, scattering and viscous losses (i.e. dissolved gases, bubbles, sediments, etc.). Typical ranges in the ocean are 5-10 m.

Maximum pinging rate --------- Limited only by the capability of the PC to store and/or process the data and by the desired profiling range (acoustic propagation time).

For the Miami DopBeam, the sampling rate is 468.16 Hz. However, the signal was averaged over 5 time steps, resulting in a rate of 93.6 Hz for the files here analyzed.

3.4 – Signal processing

As described in the previous sections, the DopBeam records the phases of the backscattered acoustic signal. Hence, the maximum and minimum phase values that the DopBeam can evaluate are π and $-\pi$, and a reconstruction of the signal was necessary. The steps followed for such reconstruction and the corrections aimed to improve the velocity series obtained, lead to several trial and error tests, which are listed in the following paragraphs.

The files used for the test and corrections were obtained during the Labrador Sea experiment of summer 2004 as detailed in Chapter 4. In summary, two devices were deployed on a platform in the open ocean to measure horizontal velocity fluctuations. One device was installed at 2 m depth (instrument A), and another at 4 m depth (B). The analysis here refers to instrument A, unless otherwise stated.

1. Phases into velocities: Radians to cm/s

The Matlab functions 'atan2', 'angle' and 'unwrap' were tested to extract velocities from the phases recorded. The test was performed initially over the first 500 points of each file (approximately 1 sec of records, for the 468.16 Hz sampling frequency), and then over several complete files, for both instruments A and B. Unwrap proved to be the most efficient in keeping the original tendency of the series to grow or

diminish (Fig. 3.3). Briefly, unwrap calculates the difference between successive input phases, keeping the sign of the angle, that is, memorizing the tendency of the signal to grow or diminish. Unfortunately unwrap gives inaccurate values when, apparently, the value of the signal is far larger than 2 π (that is for 5,6,7 π). Indeed large spikes (jumps proportional to 2π) are present in the time series, with a tendency of higher spikes to appear as we move outwards from the device (bins 20-30 have smaller spikes than bins 130-140). To correct this problem, some other test and corrections were applied, as described in the following.

2. Correlation between bins

The correlation between the time series for different bins showed the time it took to the signal to be decorrelated, for our measurements in the open ocean, and decide the interval of average. The highest values of correlation (more than 80%) were found for differences smaller than 20 bins (around 16 cm) for the first 60 bins. After the 70^{th} bin, that is, around 56 cm from the device, the series keep such correlation in space for about 24cm. The best correlations in any case seem to be up to 10 bins, that is approximately 8 cm.

3. Histograms

For ideal fluids without turbulence, the histograms of the velocities are expected to follow a Gaussian shape. For the bins closer to the instrument (bin 10-20) the histograms show perfect peaks, while less definition and a broader shape appearing for the bins situated further from the sensor (after bin 40).

4. Spectra in time

The spectra in time of the velocities were calculated initially to investigate the existence of inertial subranges (ISR), and to determine whether to average some bins, to average over some time-points or just take a portion of them. The ISR appear more evidently in the spectra corresponding to the closer bins, and start to lack shape moving away from the DopBeam.

The tests described in points *2, 3* and *4* were performed over files belonging to two different periods, for low and high winds respectively. The analysis pointed out that the results depend randomly on the file analyzed. However, it should be noted that the time series of instrument A are less noisy than those of instrument B for the files analyzed, especially for low wind conditions.

5. Unwrapping in time and/or space

The unwrapping of the signal was also performed in space, and compared to the time unwrapping. No improvement in the resulting series is evident, but the histograms of the series became more Gaussian. In addition, a combination of both 'directions' of unwrapping was tried. Performing the unwrapping only in space, improves the shape of the wavenumber spectra. But unwrapping first in time and then in space seem to have the contrary effect on the wavenumber spectra. In addition, no improvement of the phase jumps can be observed by this combination.

6. *Averages*

- *in time:* averaging the series every 5 time steps, does not resolve the ambiguity (represented as spikes) in the series. Probably more averaging is needed, but initially it

was decided not to average any points. The time-average smoothes the frequency spectra, as expected.

- *in space:* observing that the signal seemed to start to be decorrelated after approximately 3 bins, an average over 3 bins was performed. However, such averaging does not result in any improvement for both the series and the spectra.

7. *Detrending*

The detrending of the velocities series (extraction of the mean velocity and tendency) allows for the filtering of the large waves present in the data. Small portions of the time series, up to 30 seconds, were detrended. It improves the shape of the histograms of the series, that become Gaussian but does not help in the removal of the ambiguities or phase jumps. It was used only after some other corrections.

8. Ambiguity removal through extraction of the reminder from π

An attempt to remove the ambiguity of the series was performed by calculating first the difference between contiguous points and extracting the reminder after dividing by π. Then the series is reconstructed by summing up the result (matlab function 'ambiguity_removal'). The problem is that the function cannot identify correctly the sign of the differences, making it impossible to reconstruct the signal afterwards. In consequence a positive, continuously growing series is obtained (Fig. 3.3). Applying detrend to that series stops some of the tendency to grow, but very high speed values are obtained, and most importantly, huge differences between bins appear. In addition, the wavenumber spectra do not show any improvement (most of it is only noise).

9. Ambiguity removal through interpolation

Another attempt to remove the ambiguities consisted of calculating the difference between contiguous points as before, converting values higher than a certain cut-off value to NANs, unwrapping and then interpolating. Several cut-off values (C) were used: $\pi/2$, π, $\pi/3$, $\pi/6$. For C = $\pi/2$, 34% of the series were lost, for C=$\pi/3$, 43% of the data needed to be interpolated. These are mean values, as they change for each file, and each bin. The final value adopted was C = $\pi/2$. Note that for any file C=$\pi/2$ at bin 20 means losing 31% of the data, while for bin 150, 40% of the total data are lost.

In addition, different types of interpolation were tried, as linear, pchip, and spline (cubic). The comparison appears in Fig. 3.4. The resulting series obtained through these type of interpolations were extremely similar; hence a simple linear interpolation was chosen.

The main problem appears when the interpolation needed to be performed at the first point: these are automatically represented by NANs. To avoid this problem, the same technique was tried in space, but it was impossible to preserve the 'position' of the numbers replaced in the matrix after the first interpolation. For this reason, some of the bin time series are lost, and a final average spectrum will contain a very small quantity of the original series.

10. Combinations

The order of unwrapping (in time and space), applying detrend, averaging for different time steps or space steps, etc, were alternated for different files. Also the ambiguity removal before and after those combinations was tested, together with the interpolation approach. None of these tests gave satisfactory results.

11. Laspline and Lasfix: getting rid of high-frequencies (or wavenumber) noise

Laspline is a Matlab function that uses a median filter to define ‘bad points’ (with strong sudden variability and/or out of range) and then spline fits through them. The idea is to eliminate the noise at the end of the spectra that may influence the maximum energy reached and its shape. Several parameters can be chosen, as the number of points to average, the number of points used for the median filter, the maximum standard deviation STD limit of the difference between the original data and the median filtered data that will determine points to be spline fitted (called 'dfr'). Lasfix, on the other hand, is a code that simply changes the format of the data to be read by the other function.

Several trials were performed, using 7, 9 or 11 as points for the median filter, and dfr as 2 or 3. An example appears in Fig. 3.5. The original series appear in a continuous line and the curve constructed with the median filter appears with an asterisk. The bold segmented line denotes the final fitted curve.

Unfortunately, while Laspline helped get rid of most of the noise, it did not resolve the disassociation between bins. Indeed, the differences could be up to 80 cm/s between consecutive bins that is, for a distance of 0.8 cm. In addition, the times series lost most of their natural variation, and it was impossible to consider these new corrected series as a slightly modified version of the originals (see Figure 3.5, how the result in bold does not follow the original series).

12. Combination of previous trials plus filter of high energy signals

The signal was unwrapped, in both time and space. A low-pass filter was applied to reduce the sudden variations in the signal, eliminating most of the noise. Such a filter was tested with 2, 5, 10 and 20 sec as cut-off values, but the resulting ε do not show substantial changes. The best cut-off value was determined to be 10 sec, through the comparison between the spectra obtained and also between the resulting values of ε. Finally we detrended the time series using a least squares fit to a linear curve. An example of this method appears in Figure (3.6). Even if the method proves to be efficient in the automatic calculation of several large files, the values of ε obtained in this way are higher than the classical values expected (Agrawal et al., 1999; Seuront et al., 2005) by several orders of magnitude. The method seem to introduce some random noise that is difficult to identify and harder to reduce. Note, however, that the TKEDR calculated through this method were utilized only for qualitative comparison with environmental data, presented in Chapter 4.

13. Direct visualization and unwrapping on the signal without modifications

The phase signal was divided into smaller time series sections and the truncated aspect of the series generated by the limitation of the instrument (as explained in section 3.4) is avoided by adding or subtracting 2π to the series at the moment of the truncation (Fig. 3.7). In this way, we unwrap the signal by applying a simple addition or subtraction, avoiding the introduction of random noise related to the method applied. The only noise present in the velocities is related to the instrument capabilities.

Sections were unwrapped in time, and spectra were calculated in space (see next

section). The disadvantage of this method resides in its inapplicability to large files, and to a large data set.

Note that if instead of the total 56000 time steps (10 min) of the series, we take only smaller portions of the time series, as for example 94, 470 and 940 time steps (that is for 1, 5 and 10 second respectively), the values of ε obtained through method #12 have the same order of magnitude of those obtained with the method #13. This lead to the idea that the one of the problems with method #12 could be related to the large number of time steps unwrapped and averaged (56000, that is, 10 min), in addition to the random noise introduced by the method #12 itself.

3.5 – Power spectra and TKEDRE dissipation rates calculation

As mentioned in the introduction, the main advantage of the use of the DopBeam is the possibility of calculating directly the wavenumber spectra of the current variability, without using the frequency spectra and the Taylor or frozen turbulence theory. Following Kolmogorov's theory of a turbulent cascade, the portion of the spectra where the energy is transmitted from large size eddies to smaller ones is called Inertial Subrange (ISR). The transfer of energy in this range is related solely to the TKE dissipation rate:

$$S(k) = C\ \varepsilon^{2/3}\ k^{-5/3} \tag{3.5.1}$$

where S(k) is the wavenumber spectra, ε the TKE dissipation rate, k is wavenumber in the limits of the ISR and C a constant. In this way, ε can be defined as:

$$\varepsilon = D S^{3/2} k^{5/2} \tag{3.5.2}$$

with D constant. The wavenumber spectra are calculated for different files (Fig 3.8), with different time steps and space steps, explained in detail in Chapter 4.Many studies had been conducted in order to find a suitable value for the constant C. Hinze (1959) showed different values of the constant, depending on the experiments, and the different assumptions applied. Between the limits of the Kolmogorov range, he found that

$$C = 18/55 \left(8/9\alpha\right)^{2/3} \tag{3.5.3}$$

for one dimensional spectra. Here α is an effective rate of strain, proportional to $(\varepsilon/\nu)^{1/2}$ with the proportionality constant depending linearly on the skewness factor of the turbulence velocity field, namely $\alpha = -(7/6\sqrt{15}) S (\varepsilon/\nu)$. Direct observations, as the measurements of air turbulence conducted by Gibson (1962) at a Reynold number of 780, gives $\alpha = 0.45$. In his later work of 1975, Hinze used the same values as in 1959, calling α the Heisenberg constant, and assigning it a value of 0.4 for high Re numbers. Veron and Melville (1999) used the same value.

Phillips (1966) showed the results of the experiments performed by Grant et al. (1962) and Grant and Moilliet (1962) on the turbulence generated on a vigorous tidal stream in Seymour Narrows, British Columbia. For the large Re number generated ($\approx 10^8$), the value for the constant is $C = (18/55) A$, with A=1.44 with a standard deviation of 0.07 for A. Note Hinze (1975) and Gemmrich and Farmer (2004) utilized A=1.5 . Bradshaw (1976) in its book about turbulence stated, that the value of this constant C in the case of 1D spectra is about 0.5.

Terray et al. (1996) used frequency spectra to find $\varepsilon = G\, U_d\, (S_f\, f^{5/3})^{3/2}$ with U_d being the mean orbital velocity of waves and G a constant. Their value of G is 2.7 (from Lumley and Terray, 1983).

Considering all these options, and observing that most of the recent calculations of ε were obtained by using the Hinze approach (Drennan et al., 1996; Veron and Melville, 1999), we decided to use

$$S(k) = 18/55\,(8/9\alpha)^{2/3}\ \varepsilon^{2/3}\, k^{-5/3} \tag{3.5.4}$$

that is, $\varepsilon = (18/55)^{3/2}\, A\, S_k^{\,3/2}\ k^{5/2}$, with $A = 1.5$.

Subsequently, the ISR in each spectrum is detected by finding the best fit of that spectrum to a line with slope $k^{-5/3}$ (corresponding to ISR), together with the variance of the fit. A MATLAB function created with this purpose takes a portion of the spectrum and fits it to the line with slope $k^{-5/3}$. Then moves along all the values of the spectrum, in such a way that every portion of the spectrum is compared to the line slope $k^{-5/3}$, selecting the best fit. Several tests were performed to determine the minimum portion of the spectra suitable for comparison. If the portion of the spectrum taken is between 15 and 35% of the total numbers conforming the spectrum, the values of ε obtained do not show noticeable differences. After 40%, the error introducing in the fit is obviously larger, so we used 30% as a feasible limit. However, when using method #13, a direct observation of the ISR prevailed over automatic calculations.

The function in this way, identifies the ISR boundaries in both the energy spectrum and k, obtains the average of all values inside the ISR, and ultimately calculates ε through the equation

$$\varepsilon = D(\overline{S^{3/2} k^{5/2}}) \qquad (3.5.5)$$

derived from (3.5.2). Figure 3.9 schematizes the manner in which this function works.

Initial tests of ε values were performed over k-spectra obtained through method #12, to establishe the useful spatial range of the DopBeam in order to avoid possible flow distortion from the ASIS columns. Such analysis, in the case of the Labrador Sea experiment, is described in Chapter 4.

Tests for method #13 (the one considered exact) were performed over 1, 5 and 10 sec and over a minute. Also, different lengths in the spatial series were tested, that is, the quantity of bins were changed resulting in constant values of ε within a range +/- 10 bins (approx 8 cm). These results are also presented in the next chapter.

3.6 – Conclusions

The pulse-to-pulse coherent Doppler sonar has the advantage of avoiding the consideration of 'frozen turbulence' or Taylor's hypothesis. It was tested in different environments and under different conditions with fair results. As no extensive literature exists about its performance in open waters, the analysis presented here, between Chapters 3 and 4, is fundamental to understanding the capabilities and limitations of the DopBeam.

Here we present the corrections necessary to avoid the ambiguity recorded by the instrument and to obtain time series and wavenumber spectra from the backscattered signal. The best approach presented here has been the unwrapping in time of the signal by direct visualization and linear rectification, that is, method #13.

The calculation of ε involves some additional approximations as the percentage of the spectrum we want to fit to the line with slope $k^{-5/3}$. We are also assuming Kolmogorov's theory and the existence of an ISR defined only through ε. The values of ε obtained with the final method, for averages smaller than a minute, are in the range of previous works, between $10^{-6} - 10^{-5}\ m^2/s^3$.

Figures

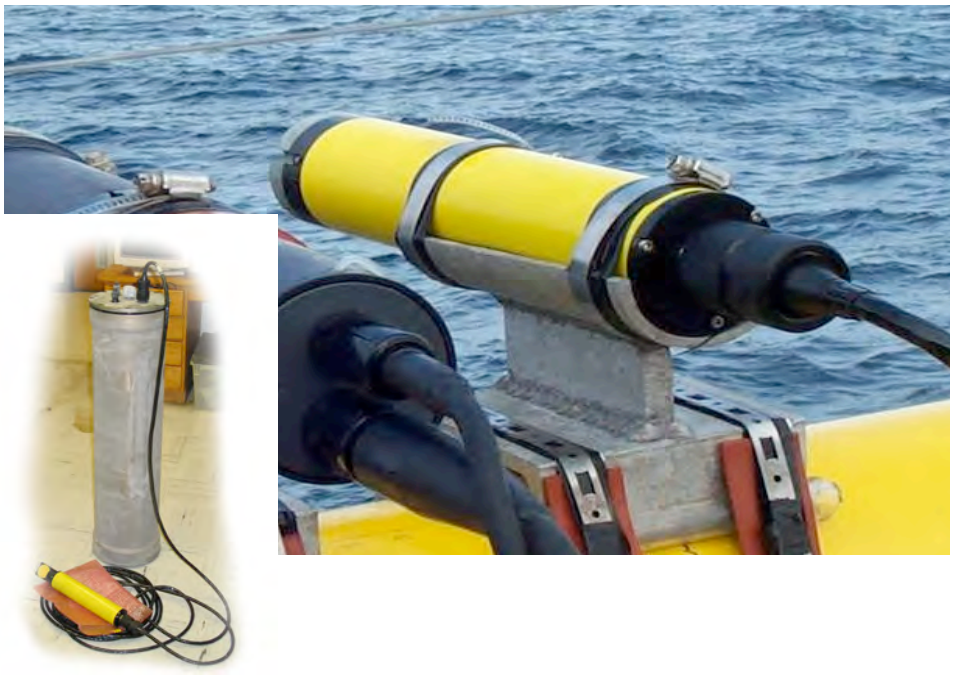

Figure 3.1: The Miami DopBeam in the lab (left) and mounted on a buoy (right).

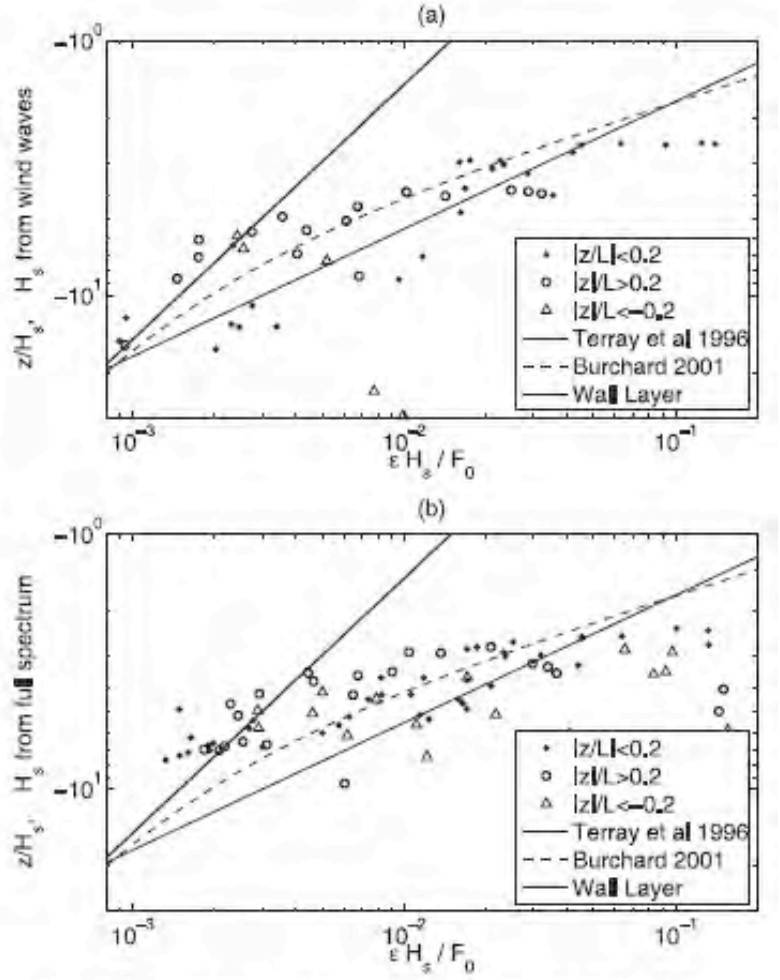

Figure 3.2: from Gerbi et al., (2009). Dissipation rates are normalized as in Terray et al. (1996). The thick lines are the expected dissipation rates using neutral rigid-boundary scaling, the thin lines show the scaling of Terray et al. (1996) and the dashed lines show the model predictions of Burchard (2001) and Craig (1996). The symbols indicate different stability regimes.

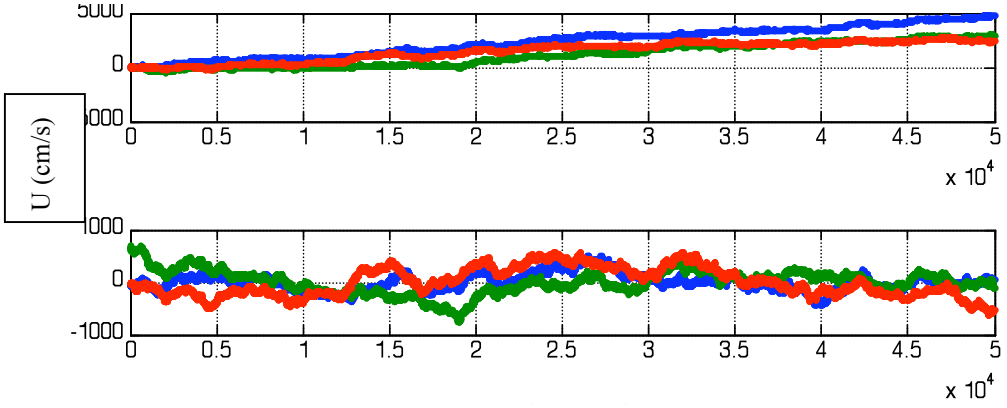

Figure 3.3: Example of 'ambiguity removal' in the series. The series is a 10 min-sample of velocities (in cm/s), as a function of sample number (1/94Hz). The upper panel is the correction as described in the text for 3 consecutive bins (around 60 (blue), 61 (red) and 62 cm (green) from the device respectively). Note the tendency of the series to grow indefinitely. The lower panel shows the detrended series with strong disagreements to the original and noticeable differences between bins.

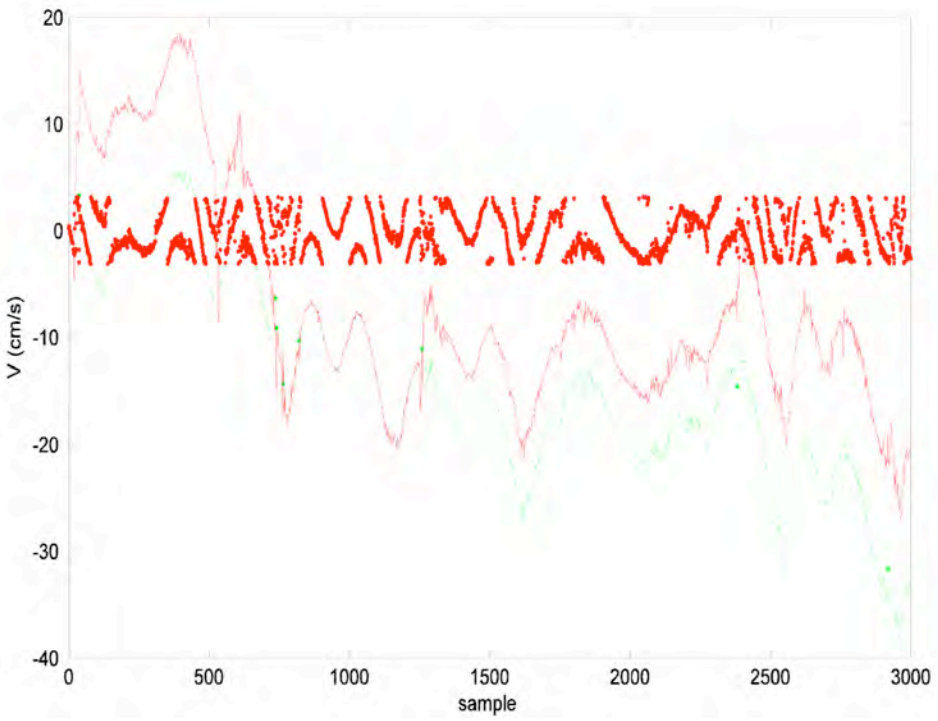

a)

Figure 3.4: a) Ambiguity removal through replacement by Nans. The red dots show the original data, and the red line an unwrap of the original. The green line shows the series without the spikes, where the jumps between consecutive points are greater than $\pi/2$.

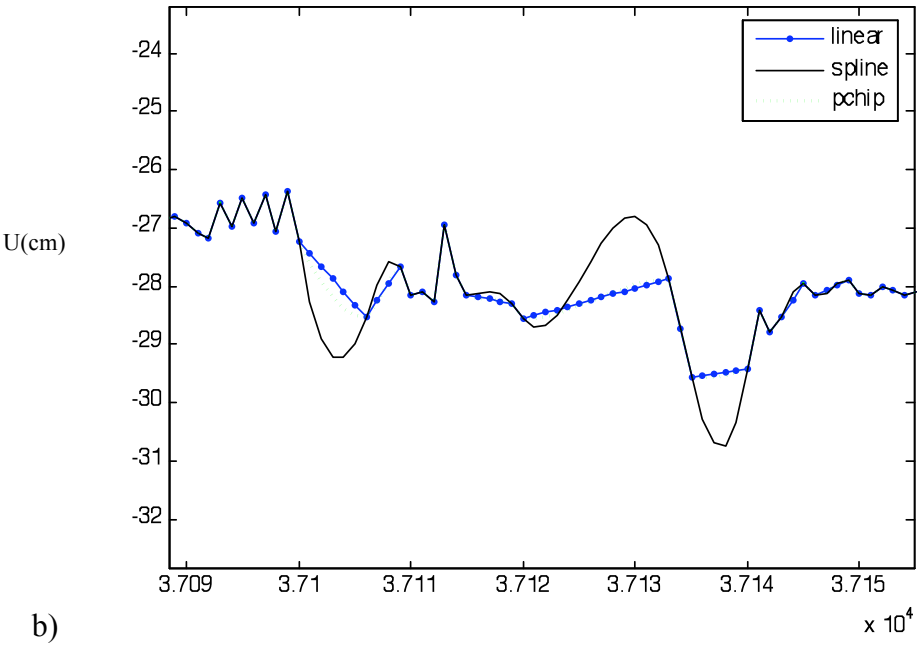

b)

Figure 3.4: b) Comparison of the resulting series for different types of interpolation. Velocities are in cm/s and plotted against sample number (1/94Hz). The blue line with dots is the linear interpolation; the black represent the splined series and the green the pchip. This example is for bin 50 (approx 60 cm from the receiver) on June 22nd at 4 am.

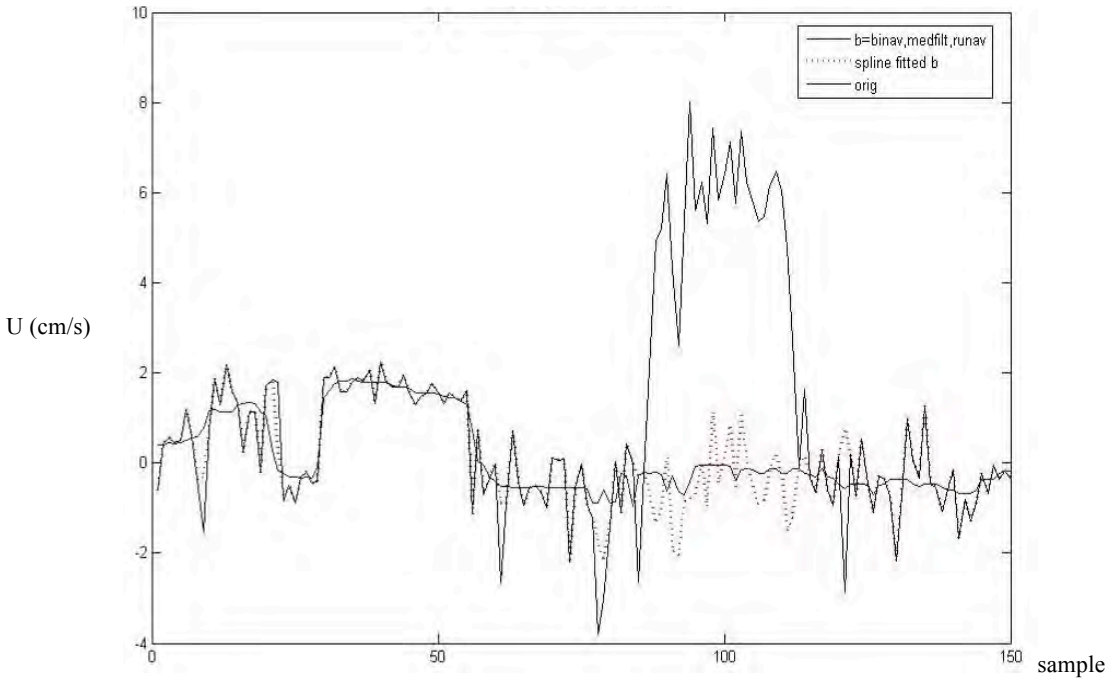

Figure 3.5: Example of the velocity series as a function of sample number, corrected with Laspline. The black line is the original velocity in cm/s, the blue line is the averaged-median filtered intermediate result, and the red dotted line is the final correction.

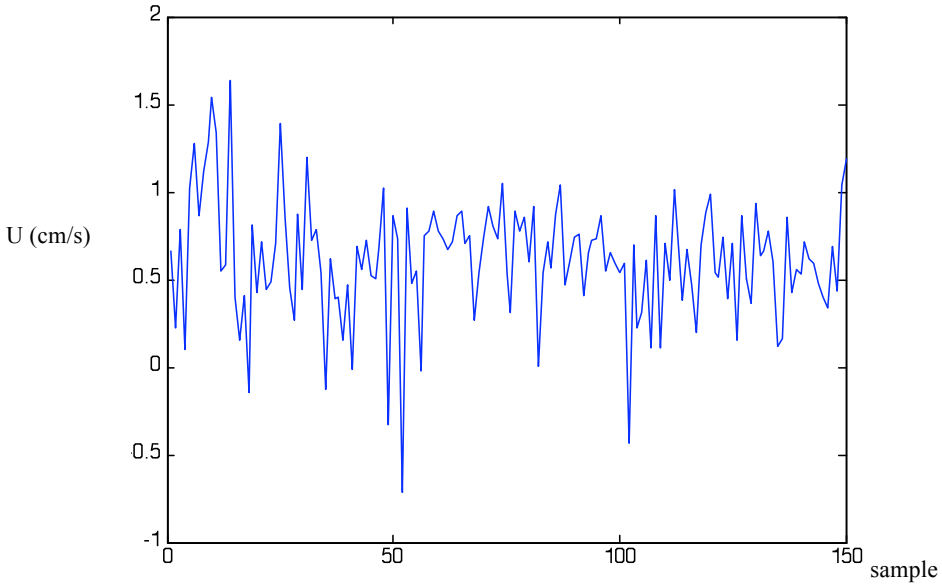

Figure 3.6: Example of the corrected velocity series from Dopbeam for June 22, at 4 am, using method #12, described in the text. The distance from the instrument is 60 cm (bin 50). Velocities are in cm/s vs sample number (1/94 Hz).

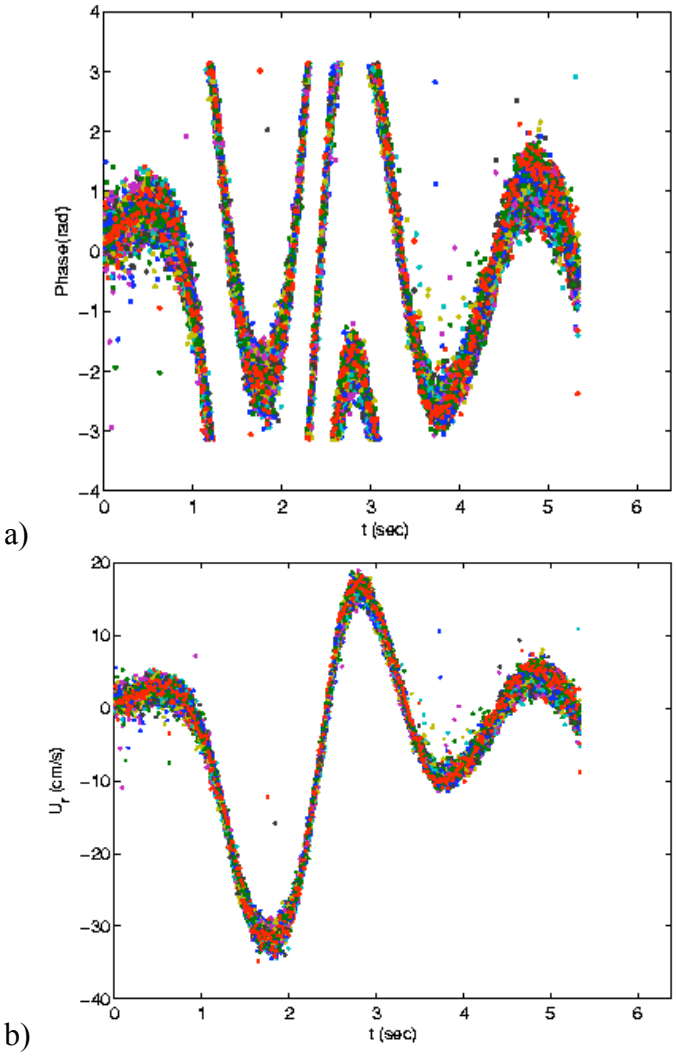

Figure 3.7. Example of the direct visual unwrapping of the series. a) phases for bins 60-90 (70 to 100 cm from the receiver), each bin being represented by a different color; b) corresponding velocities calculated as in Veron and Melville (1999).

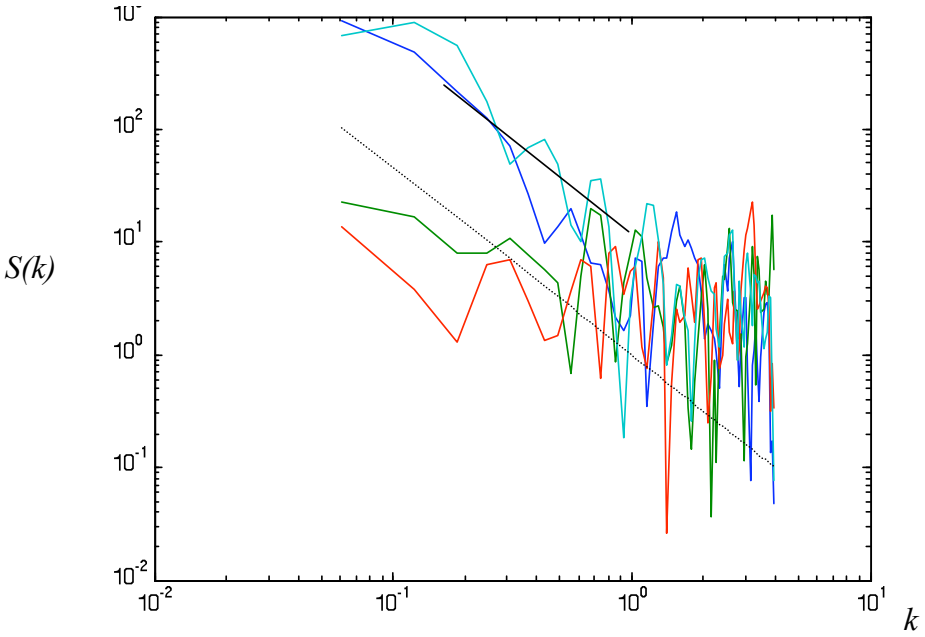

Figure 3.8: Example of wavenumber spectrum $S(k)$, in $cm^2/s^2/Hz$, of Dopbeam velocities as a function of wavenumber (1/cm), for June 16th, at 8 pm, for different portions of the file. The colors indicate different time bins, one every 10 sec. The black straight (and dotted) line indicates the line with slope -5/3, that is, for the inertial subrange (ISR).

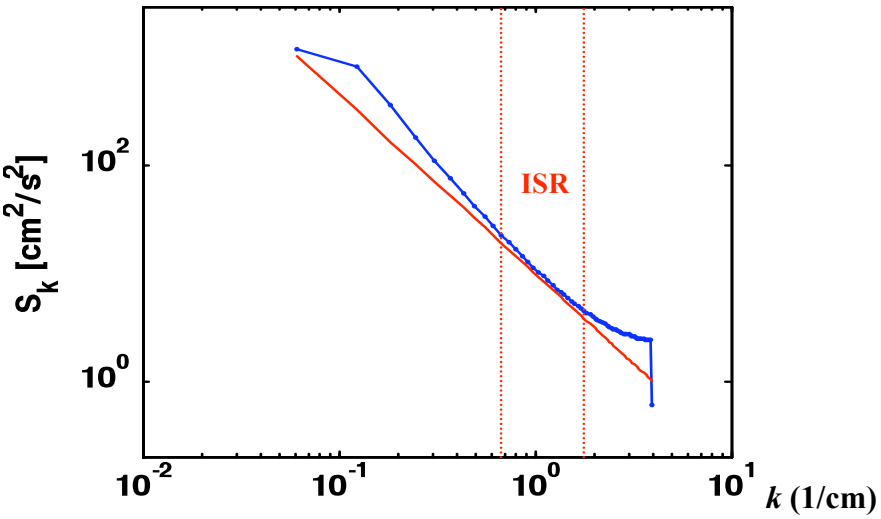

Figure 3.9: Schematic representation of the calculation of ε from the velocity wavenumber spectra $S(k)$. The inertial subrange, ISR, is determined as the portion of S that fits the red line, with slope -5/3. The dotted vertical lines represent the limits of the ISR for this case.

Chapter 4

Characteristics of turbulence close to the ocean surface: the Labrador Sea Experiment

4.1 - Overview

The turbulent structure at the ocean surface plays a fundamental role in the transfer of properties between air and ocean. One of the ways we can study the turbulence and processes involved is by studying the transfer of kinetic energy in the upper ocean. Recent efforts have been made in trying to parameterize the transfer velocities and transport across the ocean surface by means of the TKE dissipation rates. Such an approach avoids the need of defining the source of turbulence while it effect can be amply quantified.

Direct measurements of TKEDR, are difficult in laboratories and shallow waters, but become extremely complex in an open environment (Thorpe, 2007). It is usually estimated in one of 3 different ways: 1- by measuring the turbulent shear variance with microstructure profilers (Soloviev et al., 1988; Anis and Moum, 1992); 2- by measuring the velocity variance at a single point and then converting from frequency space to wavenumber space by means of Taylor's hypothesis (Lumley and Terray, 1983), as described in the previous chapter, or 3- by directly obtaining wavenumber spectra of the turbulent velocities without the passage through frequency, as with the case on hand. As presented in the previous chapter, this can be accomplished with the pulse-to-pulse coherent Doppler sonar, or DopBeam. We present here an analysis of these observations,

for the Labrador Sea experiment, carried out during the summer of 2004.

The Labrador Sea experiment consisted of the deployment of a highly specialized buoy to study air-sea interaction, the ASIS buoy (Air-Sea Interaction Spar buoy), capable of measuring oceanic and atmospheric variables at the surface boundary layer. The aim of the experiment was to measure turbulent fluxes, especially CO_2 fluxes, during the usual phytoplankton bloom occurring in the area every summer. During these blooms, the difference of CO_2 concentration between air and ocean is the maximum, allowing for these fluxes to be measured with micrometeorological techniques (e.g. McGillis et al., 2001). In addition, the CO_2 is trapped in these oceanic waters (Takahashi et al., 2002).

The area chosen is also a well know site of dense water formation. Open ocean deep convection occurs only in the Atlantic Ocean, in three major sites: Labrador, Greenland and Mediterranean Seas. These sites play a crucial role in climate variability, as the dense water produced drives the Meridional Overturning Circulation (MOC), ultimately influencing the whole ocean and climate. Moreover, this deep water convection mixes the CO_2 rich waters developed during/after the bloom throughout the water column (Lab Sea Group, 1998). The newly formed NADW is transported southward towards the Antarctic, via a system of deep currents. Given the circulation time scale of O(1000) years, atmospheric gases within the NADW are essentially sequestered. Hence the gas exchange characteristics in the Labrador Sea are of particular interest because it is one of the few areas of the global ocean that is a long term CO_2 sink. The ability to predict and forecast air-sea CO_2 fluxes over large areas is also necessary to quantify the adjacent terrestrial carbon budget.

Previous studies of TKEDR in the upper open ocean with acoustic devices are very rare. As part of the "Fluxes, Air-sea Interaction and Remote Sensing" (FAIRS) experiment, conducted in 2000 offshore Monterey Bay, Gemmrich and Farmer (2004) obtained measurements of the turbulent velocity and bubble field with three orthogonal 2-MHz pulse to pulse coherent Doppler Sonars and other instrumentation set on a surface float (Gemmrich and Farmer, 2004). The deployment lasted from September 24th until October 10th with the main intention of studying mainly the relationship between TKEDR and breaking waves. They obtained values of dissipation rates, based on wavenumber spectra analysis, of the order $10^{-6} - 10^{-1}\, m^2/s^3$, for winds between 12 and 15 m/s and significant wave heights between 2 and 4 m throughout the experiment. They proposed a parameterization of TKEDR based on wave age and wind shear (Gemmrich and Farmer, 2004). As cited in the previous chapter, measurements of TKEDR in laboratory experiments (Babanin and Haus, 2009) or in lakes (Gemmrich, 2010) also exist, and provide basis for comparison.

The current chapter presents the variability of TKEDR in temporal scales of under 10 sec, relating the results to surface forcing as wind and waves, exploring the effects of wave breaking and comparing results with previous observations and well know theories. The analysis is performed in two ways: A qualitative analysis of the TKEDR in relation to wind and currents permits the identification of the actual days when observations are reliable and also allows the determination of the flow distortion induced by the platform. A quantitative analysis performed over few files during high and low winds permit the validation of classic theories, establishes the reliability of the instrument, and provides new insight into the methodology utilized. Such new insight into the methodology,

together with the novelty of the data set, in what regards both the instrumentation, and the environmental conditions, provides new ground for studies of turbulence in the upper ocean.

In the following, the area studied is presented in section **4.2.**, the general goals of the experiment together with the instrumentation used appear in section **4.3.** The results are presented in section **4.4** and discussed in section **4.5** followed by the conclusions.

4.2. The area studied

The Labrador Sea (LS) is situated in the North Atlantic Ocean between Canada (Labrador) and Greenland, centered around 60° N and 55° W. The LS near-surface cyclonic circulation is set by the West Greenland Current and the Labrador Current (Figure 4.1), of cold and low-salinity water (Marshall and Schott, 1999). The higher salinity Irminger Sea Water flows under them, also in a cyclonic path entering from the north. The northwestern loop of the North Atlantic Current brings warmer water to the extreme southern part of the LS without really getting inside LS. It occasionally sheds eddies inside the region. The Deep Western Boundary current flows below 3000 m steered by topography carrying cold, relatively fresh water (Marshall and Schott, 1999).

Deep winter convection in the central area of the Labrador Sea has been observed for many decades (Lazier, 1973; Clarke and Gascard, 1983). The deep water formed here is part of the convection belt describing the circulation of the world ocean. It forms part of the Meridional Overturning Circulation (MOC) driving the overall Atlantic circulation,

responsible for regulating climate and weather along the USA coast and northern Europe (see schematics in Fig. 4.1).

During the late spring months, the availability of sunlight triggers the seasonal phytoplankton bloom mentioned before, clearly observed in satellite images (Fig. 4.2), that becomes an intense sink for CO_2 (Takahashi et al. 2002). The deep winter convection during the subsequent months mixes the CO_2 rich waters throughout the water column (Lab Sea Group, 1998; Avsic et al., 2006). The newly formed North Atlantic Deep Water (NADW) is transported southward towards the Antarctic, via a system of deep currents.

4.2.1. *Conditions during the experiment*

The main hydrographic conditions during the experiment have been well detailed in Martz et al. (2009). They observed that during the 70 day-period of the experiment, the mixed-layer temperature increased from ~ 5.5° to 11.5° C and winds ranged from ~1 to 15 m/s with a mean of 6.3 ± 3.1 m/s. The salinity record suggests the presence of at least two different water masses. The Labrador Sea central gyre water dominated for the first half of the deployment. After mid-July (YD 200), the periods of lower salinity indicate the intermittent contribution of Labrador Current water (Martz et al., 2009).

They also modeled mixing processes showing a wind dominated mixing in the water column with periods of cooling when static instability allowed it. As winds dropped and solar irradiance increased in late June, the Mixed Layer Depth (MLD) shoaled and remained shallower than 35 m for the remainder of the study. Between YD 180-200, during a low wind period, the MLD averaged 8 m. After YD 200, the MLD progressively deepened to a mean of 16 m (Martz et al., 2009).

Sea surface pCO_2 was ~50 μatm below saturation in mid-June (Martz et al., 2009), indicating that, even though phytoplankton standing stocks were low, significant biological drawdown had already occurred. Chl-*a* rapidly increased by 18 June (YD 170) and peaked on ~3 July (YD 185), dropping pCO_2 to 260 μatm, 120 μatm below atmospheric saturation. The chl-*a* levels indicate that the bloom was more intense than usual (Strutton et al. 2009). As the bloom declined, the pCO_2 began climbing, and leveled off around 300 μatm.

4.3. Labrador Sea Experiment: goals and instrumentation

The purpose of the experiment was to study the air-sea flux of carbon dioxide and the surface physical processes controlling it during the Labrador Sea spring bloom. The importance of this region in the global carbon cycle, and the unique atmospheric and oceanic conditions, warrant the direct determination of fluxes and gas transfer velocities, rather than the use of parameterizations developed for other regions/conditions. The aim of the experiment was then to perform continuous measurements of ocean-atmospheric fluxes and surface physical processes in the lower atmosphere, through the interface, and at the surface ocean from an Air-Sea Interaction Spar (ASIS) buoy. The ability to continuously measure gas fluxes simultaneously with continuous surface wave and current field measurements is essential to understand the controls of, and variability in, air-sea CO_2 exchange.

The parameters targeted were wind speed, wind stress, atmospheric stability, surface waves, upper ocean turbulence and mixing, and key parameters governing mixed

layer CO_2 dynamics, along with air-sea CO_2 fluxes, and CO_2 profiles in the atmospheric boundary layer. The idea was to determine the role that surface waves and turbulence play in controlling air-sea CO_2 exchange, essential to advancing the capabilities for remote-sensing of air-sea CO_2 fluxes. The proposed project, with its focus on the physical processes and quantification of air-sea fluxes, would complement efforts of Canadian SOLAS (Surface Ocean Lower Atmosphere Study) focus on understanding biogeochemical processes in the Labrador Sea.

Unfortunately, as explained in Chapter 1, the eddy correlation tower suffered a power supply problem, and the atmospheric turbulent measurements become unavailable. In this chapter we are focusing on the oceanic turbulence, the TKEDR and their relationship with surface physical processes. The broader impact of the project was to improve the parameterizations of air-sea turbulent fluxes, that is still the main purpose of this dissertation.

4.3.1. *The ASIS buoy*

The Air–Sea Interaction Spar (ASIS) buoy is a stable platform that can obtain measurements with low flow disturbance in both the atmospheric and the oceanic surface boundary layers (Fig. 4.3). It is capable of reliably and accurately measuring directional wave spectra, atmospheric surface fluxes, and radiation in the open ocean (Graber et al., 2000).

Its design helps to reduce the motion of sensors relative to the surface, while retaining the low flow disturbance characteristics of a slender spar. It permits a variety of wave sensor array geometries without major modification; it is sufficiently stable in pitch

and roll to facilitate active acoustic and microwave remote sensing and radiation flux measurements; and it is usable in deep or coastal waters, either moored or freely drifting. Previous deployments demonstrated the seaworthiness of the moored buoy system in winds over 18 m/s, and seas in excess of 3-m significant heights. Measured response functions indicate that the buoy will follow waves longer than 7 s with good vertical stability, and thus the buoy should be capable of providing accurate measurements in severe sea states (Graber et al., 2000).

Sensors mounted on the ASIS measure quantities with respect to a moving frame of reference and must be transformed into fixed coordinates. The required measurements of the buoy motion are provided by a six degree-of-freedom inertial package consisting of accelerometers, angular rate gyros, and compass.

Surface elevation is measured using a compact array of wave height gauges within the pentagonal "cage" of the ASIS. The arrays consist of eight wires, each roughly 3.5 m long. Five wires were installed on the faces of the pentagonal cage (at a radius of 0.93 m), midway between adjacent columns. Three additional wires, making up a right isosceles triangle with equal sides of 0.044 m, were placed with the right angle vertex on the centerline of the spar. The centerline wire together with the five on the faces of the cage make up a centered pentagonal array, which has a relatively uniform directional sensitivity for waves of length 1.8 m and greater. The small triangular array at the center is used to estimate the directional distribution of shorter waves with wavelengths from 0.1 to 1.8 m. In addition, the triangular array gives two orthogonal components of slope for waves in this range (Graber et al., 2000).

Since the restoring force of the ASIS is relatively small (190 kg/m), it is important to avoid additional downward forces that can be generated by connecting the spar to a subsurface buoy or anchor (Tasai et al., 1980). To avoid these forces, the ASIS is attached to a surface mooring (the "tether buoy") by means of a buoyant tether. The tether consists of coil chain and wire rope with light reflecting colored plastic floats to keep the tether at the surface and improve its visibility from afar.

The use of a surface mooring has other advantages in that the tether buoy can carry subsurface instrumentation, such as current meters, acoustic Doppler current profilers (ADCPs), ambient noise sensors (e.g., WOTAN), and thermistor strings, spanning the entire water column. To avoid mechanical fouling, the tether buoy is connected to its vertical mooring line via a swivel and is attached to the lateral tether through a torque-amplifying lever arm on top that extends beyond the diameter of the buoy. This arrangement also facilitates launching and recovery operations (Graber et al., 2000). For this experiment, instruments were located at 3 and 5 m on the main ASIS buoy and 9, 15, 20, and 35 m on the tether mooring. Based on a pressure sensor at 35 m, the instrument depths remained within ± 0.4 m throughout the deployment. In addition to the instruments listed, downward-looking 300 kHz and upward-looking 1200 kHz ADCPs were deployed on the ASIS at 8 m depth.

Wind stress is estimated by direct eddy correlation from sonic anemometer measurements of winds, corrected for platform motion using the output from the inertial sensors. The sonic anemometer (Gill Systems Solent) utilizes an asymmetrical design in which the three vertical support rods making up the head are 60° apart, resulting in an unobstructed azimuthal measurement aperture of 240°. Since, when tethered, the ASIS

points in the direction of the resultant of the forces due to the wind and near-surface current, the use of the asymmetrical head increases the likelihood of unimpeded flow through the sensor. The instruments are individually calibrated in a wind tunnel and are delivered with a calibration table that can be used to correct for azimuthal distortion due to wakes from the support rods and transducers (measured in steady flow). For the asymmetrical head, these corrections are small for wind directions within ±100° of the centerline.

4.3.2. *Evolution of the experiment*

The mooring was deployed at 53^{o} N 49^{o} W in the south-central LS on June 12, 2004 (Figure 4.4). The ASIS buoy was tethered with a 60 m cable to the mooring. On June 30 (Year Day 182), both the tether buoy and ASIS began to drift, likely the result of entanglement with fishing gear from an unidentified vessel, creating an inadvertent quasi-Lagrangian experiment for the last 7 weeks of the deployment. The buoys drifted together in a northerly direction ending up near Ocean weather station Bravo (OWSB) (Figure 4.4). Both buoys and all instrumentation were recovered on August 25, 2004. The deployment spanned year days 168-237.

A leak in one of the instrument's housing compromised the meteorological measurements early in the deployment. Consequently, only the mean wind speed was actually used in the present comparisons, as the turbulent fluctuations of wind speed could not be obtained.

The accuracy of the ASIS mean wind speed and direction was confirmed by comparison with model outputs generated by the National Center for Environmental

Predictions (NCEP). The comparison with the NCEP 4-hourly reanalysis winds, interpolated to half hr intervals (Fig. 4.5) showed a correlation of 0.72 between both series, and no significant bias (Martz et al., 2009). This good correlation allows us to use the mean ASIS winds for our analysis.

4.4. The DopBeam files

The files analyzed here were obtained with the pulse-to-pulse coherent Doppler sonar described in Chapter 3. Two of these one-dimensional sonars were installed at 2 and 4 m depth. In the following, we will call 'A' the shallower instrument, and 'B' the deeper one.

The sampling frequency of the instruments is 468.16 Hz. However, for storage purposes the signal was averaged every 5 time steps, resulting in files with a 93.6 Hz sampling rate. Data were recorded every hour, for the first 20 min of each hour, during 70 days (from June 13th until August 22nd, 2004). However, only the first 10 days gave reliable data as will be shown in the following section.

For the first treatment and corrections of the received signal necessary to convert the phases to the current velocity fluctuations please refer to Chapter 3. The analysis performed in this chapter refers to the velocity series already unwrapped and corrected, following methods #12 and #13.

4.4.1. Methods

Two different types of analyses were performed over the data, requiring different averages in space and time. A qualitative analysis of the DopBeam data allowed the

determination of the flow distortion induced by the platform (section **4.5**). For such analysis, the velocity series utilized were those derived from method #12 (see Chapter 3). The wavenumber spectra along 128 bins (from bin 10 to 137) were then calculated for every time step, for the first 10 min of every file, and then averaged forming one spectrum per file. From such mean spectrum and its ISR, the TKEDR was then calculated according to the Kolmogorov's theory, as detailed described in Chapter 3. Then different ranges were compared to these 128 bins to estimate distance from the device where the flow distortion is detectable (see section **4.5**).

The focus of this chapter is, however, the quantitative analysis performed over some of the files, in conditions of high wind (June 16th at 4 and at 6 am, and June 17th at 4 am) and low wind (June 18th at 20 and at 21 hr). For this analysis, the velocity time series utilized were derived from method #13. Five seconds of each file mentioned above were used (470 time steps) for the TKEDR calculations. The wave number spectra were calculated for every time step, for a range between bin 70 and bin 132 (equivalent to 56 - 105.6 cm from the device), being less subject to platform/device induced noise. Then the TKEDR for the 5 sec was obtained in 2 ways: by averaging all the spectra and obtaining one TKEDR from that averaged ISR, and by obtaining one TKEDR for each spectra and then average all the TKEDR. Both values of TKEDR are usually of the same order of magnitude ($10^{-5}\ m^2/s^3$); the detailed analysis can be found in section **4.6.**

Note that this procedure was applied to different portions of the file, separated in both time and space, in order to determine the error induced in assuming only one TKEDR value as representative of the whole file.

4.5. Qualitative analysis

The influence of the metal structure of the buoy can create additional sources of turbulent energy. Such effects are mostly evident in the case of instrument B, whose relative position within the structure is problematic, as we can observe in Fig 4.4. Indeed, the sonar B has been situated close to the flotation cylinders, that could lead to an extra source of turbulence due to recirculation inside the structure.

4.5.1. Influence of the water current direction- Assessment of the accuracy of the data

As the yaw, pitch and roll were recorded throughout the duration of the experiment, for the motion corrections, we have the absolute position of the ASIS with respect to the magnetic North. In addition, the ADCPs mounted on ASIS recorded absolute current velocities in 3D. We performed then a comparison between the position of the buoy and the ocean currents, to understand when the currents arrive cleanly to the DopBeam in a frontal way, and when they arrive from the back of it, and then, passing through the buoy structure. For this comparison we used the yaw recorded by ASIS and the currents as measured by the 300 kHz ADCP, calculated at 13m depth.

Figure 4.6 shows the relative angles of the Dopbeam position and the currents. Angles are measured from 0° turning clockwise; in this way, zero degrees implies that the current comes directly into the DopBeam. Positive values appearing in Fig 4.6 indicate that the currents are coming toward the buoy without structure influence, and negative, exactly the opposite.

An easier way of seeing this result is presented in Fig 4.7, where the values of ε are denoted in different colors depending of the sign of the previous angles, i.e., blue

designate flow coming toward the ASIS, and red the opposite. The days where both colors are equally distributed correspond to the time where ASIS was drifting (after yearday 182, June 30th). In the first 10 days, the negative values (red) coincide with a moment where ε was expected to decrease (as both waves and wind decrease). In fact around day 176 ε increased. Augmented flow distortion will certainly explain such an unexpected behavior.

In the analysis that follows we focus in the period before day 175, when the mooring was still intact and the wind was strong enough to keep ASIS pointed in a favorable direction for DopBeam data analysis.

Note that this analysis has been performed using the preliminary results, that is, with the velocities obtained from method #12. We assume that the noise introduced in each file by the method is the same, resulting in equally enhanced TKEDR (of about 2 orders of magnitude) throughout the experiment. While we acknowledge this is a strong approximation, the noticeable change in TKEDR values after the buoy starts to drift freely, encourages the results.

4.5.2. Influence of the distance from the platform

The above mentioned calculations of ε were obtained for the bins situated between bin 10 and 137 (an equivalent distance of 16 to 117.6 cm from the DopBeam). The closest bins to the structure, the ones expected to feel most strongly the flow distortion were deliberately left outside the spectra for the previous analysis. However, to quantify such distortion, the TKEDR were compared to the ones calculated for what we will call 'Range 2', that is, from bin 10 to 73 (Fig 4.8). For the instrument A, we can

observe a reduction in the values of these new ε_2 (or ε for range 2) of around 30% with respect to the originals. This is an unexpected result, since we would expect more turbulent energy dissipated closer to the structure. However, we also observe the order of magnitude and the variability tendency is conserved. In addition, to find out for how far the structure influence can be perceived, we calculated ε_3 for the 'Range 3' that is, from bin 80 to 143. Here the reduction is of around 35% with respect to the originals.

The results from the instrument B are excluded from the rest of the calculations as are less reliable.

4.6. Quantitative analysis – Results

4.6.1. Assessment of TKEDR temporal and spatial variability within a file

In order to look at the variability of TKEDR estimates due to the length of the time period, and number and position of spatial bins, different portions of the velocity time series were taken and processed as explained in section 4.4. We compared sections with an increased number of spatial bins and a variable number of time steps. For June 16th, 0600 hr (file 061606) the different portions and values used to calculate TKEDR can be found in Table 4.1.

After the analysis of several files, we can conclude that it is important to maximize the number of spatial bins incorporated in the calculations as this will enhance the spectral resolution. However, there is an optimal amount of spatial bins that does not involve all of the possible DopBeam range, as the bins closer to the receiver are more

influenced by the platform, and the ones further away exhibit a substantial decrease in the signal-to-noise ratio. Also, it was noted that the time interval for the series, should be short enough as to ensure stationary conditions.

bins	time steps	$\varepsilon \times 10^{-5}\, m^2/s^3$
40-111	1000-1013	2.20
45-111	700-740	0.80
40-111	700-713	0.85
40-111	700-740	0.86
45-111	700-713	0.87
30-115	700-713	1.02
10-137	700-710	1.11
20-117	907-1000	1.93
20-113	660-753	1.66
10-137	660-753	1.45
60-121	623-1090	1.32

Table 4.1. Values of TKEDR for 1 file (June 16th at 0600). First column is the distance from the receiver, each bin is 0.8 cm. Time steps are 1/93.6 sec. Wind speed was 13.73 m/s and the significant wave height, H_s = 1.74 m

From Table 4.1 we can see that the variability in TKEDR is higher when the number of spatial bins changed rather than when the time steps to average changed. However, the difference of changing up to 5 bins (far away form the most noisy bins) is between 2 and 6%. It was clearly observed in several files that the noise is present mostly

in the bins closer to the DopBeam, and the ones farther away. Hence, the range 70-131 was adopted as the best choice. Regarding the choice of times, it depends in each case of where the cleanest signal is received, that is, the less noisy part of the series is chosen. Here I refer to noise as a phase signal that can be easily unwrapped. But also considered only the spectra that exhibit a defined ISR, in such a way that the Kolmogorov theory can be applied.

Other files analyzed in high wind conditions this way were June 16th, at 0400 UTC and June 17th, at 0600 UTC. Note that even if the conditions change slightly for June 17th (Table 4.2), we still have a wind speed of almost 10 m/s.

Day-time	$U_{10}(m/s)$	$H_s(m)$	F(m/s)^3	$\bar{c}$ (m/s)	u_{*_w} (m/s)
160400	13.7310	1.7433	0.0022	5.9617	0.0192
160600	12.0055	1.8529	0.0014	5.7659	0.0157
170400	9.2290	2.7763	0.0007	5.9617	0.0111
182000	6.6556	2.0381	0.0004	6.8992	0.0075
182100	5.6726	2.1202	0.0002	6.1714	0.0061

Table 4.2. Files and variables observed. The first column indicates the day and time of the file in June, being the first 2 digits the day, and the rest is the time in UTC. H_S is significant wave height, F is the wind input, u_{*_w} is the water-side friction velocity and $\bar{c}$ is the effective phase speed, $\bar{c} = 0.5C_p$ where C_p is the peak phase velocity as in Terray et al., (1996).

4.6. 2. Comparison of TKEDR estimates with previous parameterizations.

In order to establish if the values of dissipation rate obtained are within the limits of previous observations, the TKEDR were scaled in two different ways, introducing the

effects of winds and of waves.

To introduce the effect of wind, we scaled the TKEDR with u_* following the Law of the Wall (Fig 4.9) as in Drennan et al. (1996). Note that the u_* considered here is the friction velocity in water, derived from the stress relationship at the surface: $\rho_a u_{*a}^2 = \rho_w u_{*w}^2$, and then $(\rho_a / \rho_w) u_{*a}^2 = u_{*w}^2 \cong u_{*a}^2 / 800$, with ρ being density. Our calculations show TKEDR ten times higher than the Law of the Wall, which is consistent with the findings of Terray et al. (1996) and Drennan et al. (1996).

To introduce the effect of waves, we scaled the TKEDR with the significant wave height (H_S) and the momentum input F (Fig 4.10) as in Terray et al. (1996). Note that the representative wave height is defined as $H_s = 4\sqrt{\int S_{nn}\, df}$, where S_{nn} is the frequency spectrum of the waves during the period observed, as measured with the wave gauges mounted on ASIS, and corrected for platform motion following Pettersson et al. (2003). The wind input F is defined as $F = u_{*w}^2 \bar{c}$ where $\bar{c} = 0.5 C_p$ with C_p defined as the phase velocity at the peak of the spectra.

The TKEDR used in the scaling were calculated over 5 second portions of the series at two different times within each file during the high wind conditions. For the low wind conditions only one 5sec-TKEDR was calculated, as such files are considerably noisier than the high winds ones, allowed only a shorter part of the series to be unwrapped.

4.7. Discussion and conclusions

From the first analysis of the velocity series regarding range and time portions, we can conclude that the change in bins is more influential on the final value of TKEDR than the change in time. This is mainly due to the flow distortion at close range and to the noise present in the observations at far range. Such noise is derived from the platform itself, but it also appears to be an overlapping of signals along the path of the DopBeams that creates some sort of interference (Fig 4.11). This sort of reverberation was not mentioned before for these DopBeams, and it represents new insight into this type of techniques. It was observed that the variation in TKEDR induced by the change in bins when they are already free of noise is less than 10%.

Regarding the differences found when the portions of the time selected are different, always within a file, we can refer to two nonexclusive explanations. One refers to the well known phenomenon of intermittency (Agrawal et al., 1992; Seuront et al., 2005), where TKEDR can fluctuate in less than 0.01 up to 1.5 orders of magnitude.

Table 4.3 presents values of TKEDR for each file; each one obtained every 5 sec, as described in Section 4.4. The order of magnitude found for all the TKEDR are in agreement with previous theories. In particular, we explored the scaling with Law of the Wall as in Drennan et al. (1996) and the Terray scaling (Terray et al., 1996), as presented in Fig 4.9 and 4.10. The ranges presented in both cases are in agreement with both articles. Our results are in excellent agreement with the ones of Terray (Fig 4.10), as shown in Drennan et al. (1996). We also scaled our TKEDR with the scaling of Gemmrich (2010), finding an average scaled TKEDR, $\varepsilon\kappa z/u_{ref}^3$, of about 0.8,

corresponding to the lower limit of his representation (Fig 4.12), far away from the high values that occur near the surface. Here $u_{ref} \sim 2\ u_*$, following Gemmrich.

Gemmrich (2010) performed an experiment in Lake Washington with 3 high-resolution pulse-coherent acoustic Doppler profilers to explore the 3D turbulence beneath strongly forced waves. He obtained TKEDR values within non-breaking wave crest 3 times larger on average than values found within the wave trough regions. The ratio increases to 18 for periods with frequent wave breaking. This results in TKEDR of about 1 to 2 order of magnitude higher in the crest regions than previous works (as Terray et al., 1996 and Drennan et al., 1996). He challenges the Terray et al. (1996) and Drennan et al. (1996) results by pointing out the differences in the set up of the experiment. Indeed Terray et al. (1996) used tower-based instrumentation, constraining the measurements to be obtained well below the wave troughs, as the instrument needs to remain continuously below the water. It could be argued then, that Terray et al. (1996) TKEDR derivations were lower than Gemmrich's findings because they have being acquired constantly well under wave troughs, missing most of the turbulent energy. However, long time (order 30 min) TKEDR averages from both Terray and Gemmrich were found to balance the wind input. In Gemmrich's data the high TKEDR rates beneath the crest were balanced by much lower rates beneath the troughs.

In the case of Drennan et al. (1996), they attached their instrumentation to the front of a small vessel, extending the applicability of Terray calculations to typical oceanic conditions. Indeed they performed these measurements during the SWADE (Surface Waves Dynamics Experiment), in the North Atlantic. Drennan et al. (1996) results confirm Terray theory, while contrasting the Gemmrich results.

For our experiment, the main advantage of the setting is that the instrumentation is floating in a platform, with the possibility of measuring both wave crests and troughs. In addition, it is performed in open ocean, where waves are not constrained as in a lake, or in a tank. The uniqueness of this DopBeam data set can then give fundamental insight into the problem of understanding the order of magnitude of the TKEDR in real open ocean conditions.

With this purpose, the files afore mentioned (Table 4.1) were differentiated in crests, troughs and sides (see Figure 4.13 as an example). The wavenumber spectra for these short portions (of 15 time steps, equivalent to around 0.1 sec) were then obtained. Only the spectra where a defined ISR can be identified were then used to calculate the TKEDR and then averaged (Table 4.3).

A statistical analysis was then performed over the results. The unpaired T-test compared the values of TKEDR for crests and troughs to understand if there are similarities or if one set is indeed always higher than the other. The hypothesis of being similar is true when the P-value is > 0.05. As we can see in Table 4.3 all the P-values prove that the differences between crest TKEDR and troughs TKEDR are negligible, that is, the hypothesis of similarity, with a 95% confidence has been proved. This statistical analysis proves that there are not significant differences between TKEDR under crest and troughs, which is counter to the results presented by Gemmrich (2010).

This novel result is a particularly important one, as it sheds some light over recent discrepancies in the TKEDR values. I showed here that high energy rates can be found under any part of a wave, not in association only with crests, showing that intermittency

is not a relative effect, but generalized: there is no preference of crest or troughs for high TKEDR to appear.

File name	Section	Crest $\varepsilon \times 10^{-5}\ m^2/s^3$	Trough $\varepsilon \times 10^{-5}\ m^2/s^3$	P-value
61604_1	1	7.543	5.537	0.861
61604_2	1	3.421	4.483	
61604_3	1	-	2.157	
61604_1	2	2.232	4.224	0.264
61604_2	2	1.99	2.310	
61604_3	2	3.473	4.722	
61604_4	2	1.099	-	
61606_1	2	1.358	1.730	0.664
61606_2	2	4.256	5.327	
61606_3	2	5.172	1.247	
61606_4	2	-	2.377	
61704_1	1	3.648	1.880	0.213
61704_2	1	2.701	1.680	
61704_1	2	0.971	0.884	0.614
61704_2	2	1.543	1.183	
61820_1	1	1.035	2.474	0.105
61820_2	1	1.222	3.389	
61820_3	1	1.249	1.743	
61821_1	2	2.912	0.963	0.919
61821_2	2	1.059	2.683	
61821_3	2	4.130	-	

Table 4.3. TKEDR for crests and troughs. The numbers after the file name denotes number of crests or troughs. ‘Section’ refers to different parts of the file. Last column express the probability of both samples to be similar (P>0.05 implies they are) with a 95% confidence level.

In the Lab Sea experiment, we were not able to distinguish breaking from non-breaking waves. Nevertheless we note that Gemmrich found differences between trough and crest TKEDR for both breaking and nonbreaking waves. It is very possible that the DopBeam will miss high dissipation events under breaking waves due to the non-existence of an ISR. However, this would also affect the Gemmrich results, and so can not explain the differences seen here.

Figures

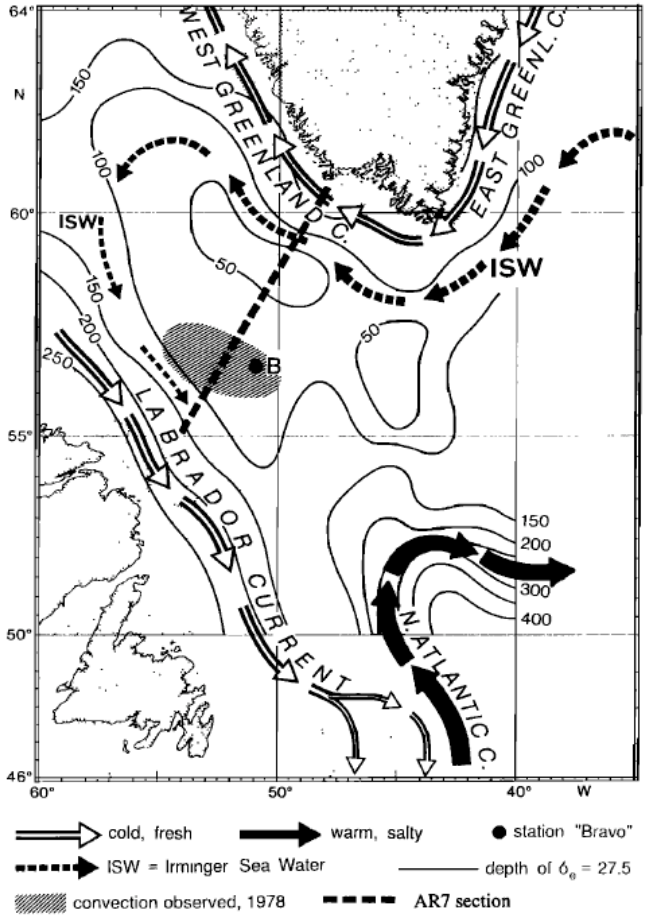

Figure 4.1. Schematic of Labrador Sea circulation (from Marshall and Schott, 1999). The direction and characteristics of the inherent currents are also shown. The B dot denotes the well known Ocean Weather Station Bravo.

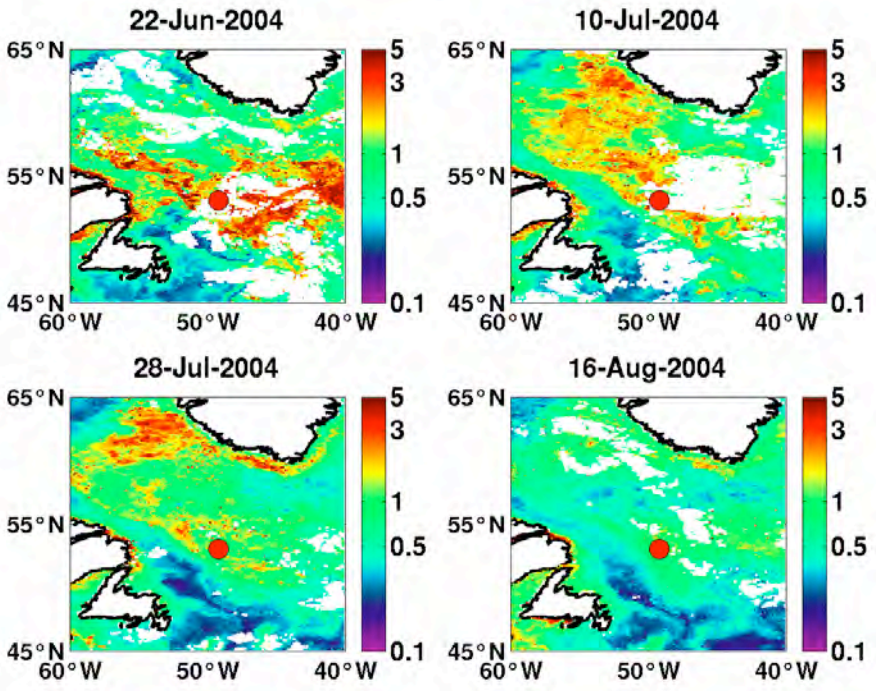

Figure 4.2. Satellite composites of Chlorophyll images from Sea Wifs showing the passage of the spring phytoplankton bloom through the domain. The red dot represents the site of the deployment. (From *daac.gsfc.nasa.gov*)

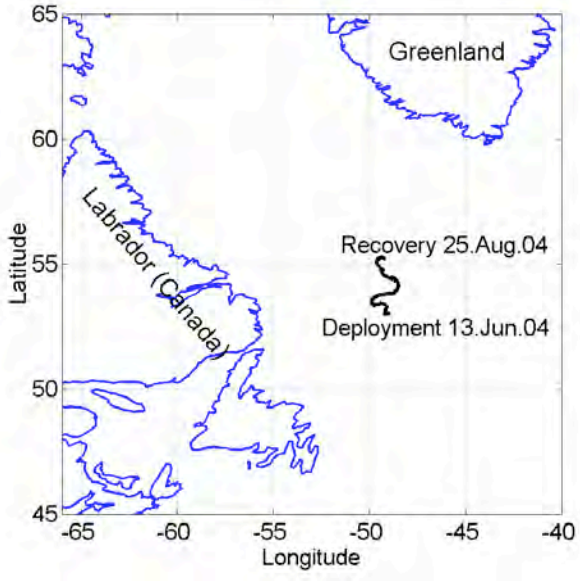

Figure 4.3. The site of the ASIS deployment, its path after 10 days, and the dates of the experiment.

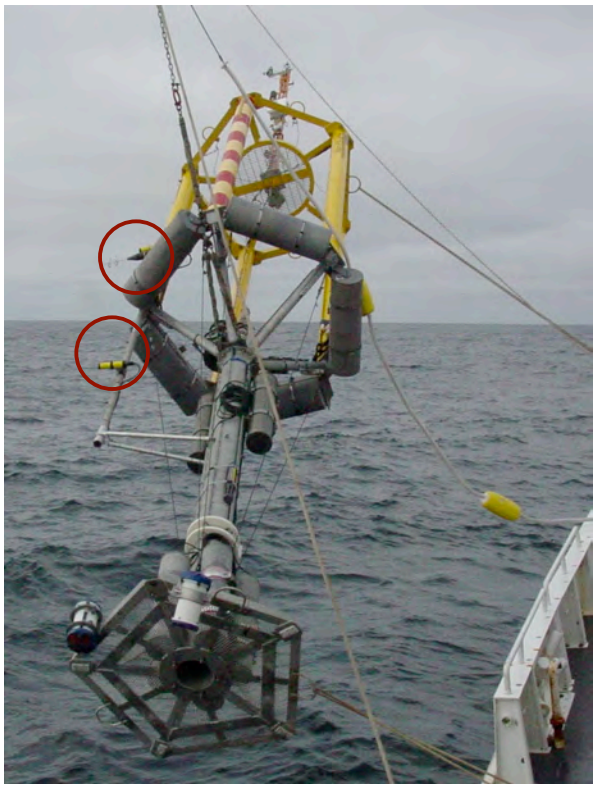

Figure 4.4. Photo of ASIS and its instrumentation. Note the position of both DopBeams.

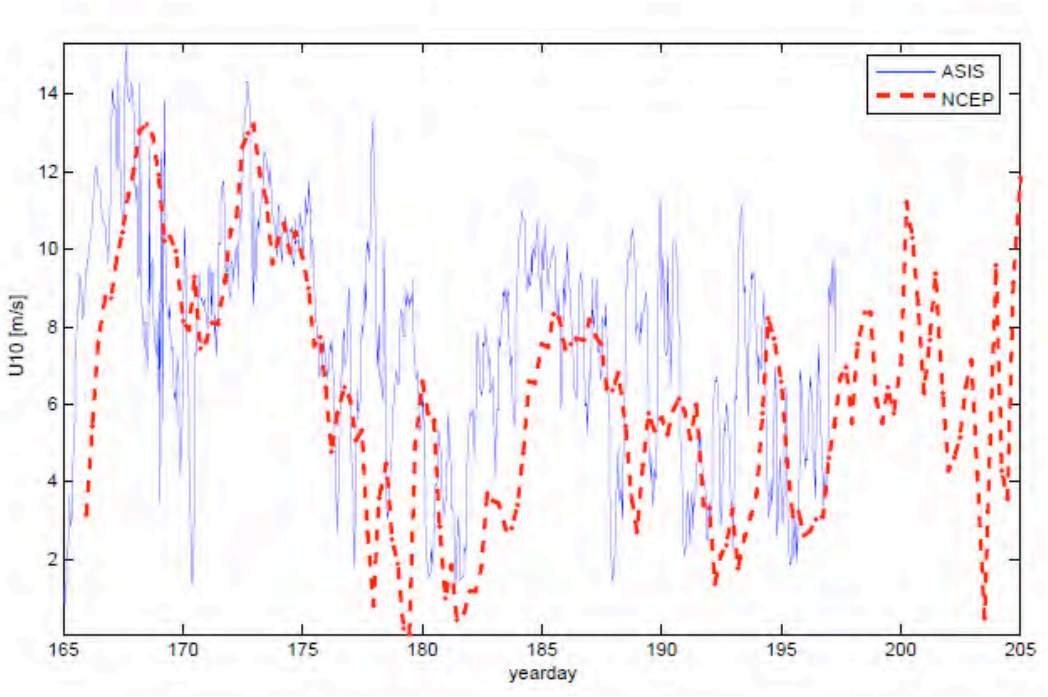

Figure 4.5. Mean wind values from NCEP 4-hourly reanalysis data, interpolated to half hr intervals, and from the ASIS tower.

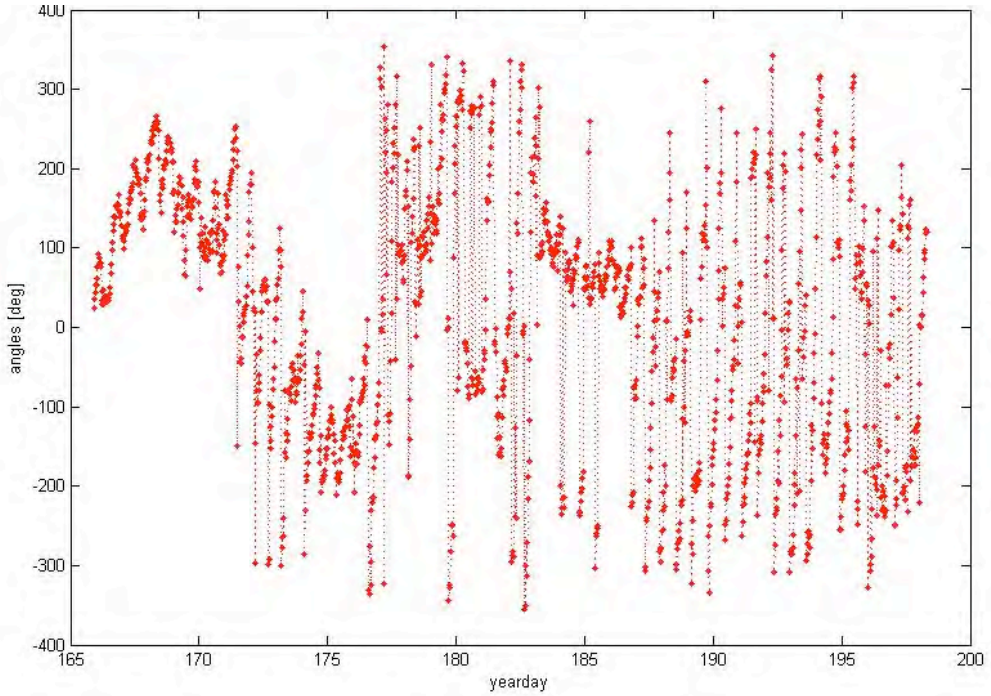

Figure 4.6. Comparison of the position of the buoy relative to the incoming ocean currents. Positive values indicate currents coming towards the DopBeam without interference of the buoy. Negative values indicate relative currents coming from behind the Dopbeam and passing through the ASIS.

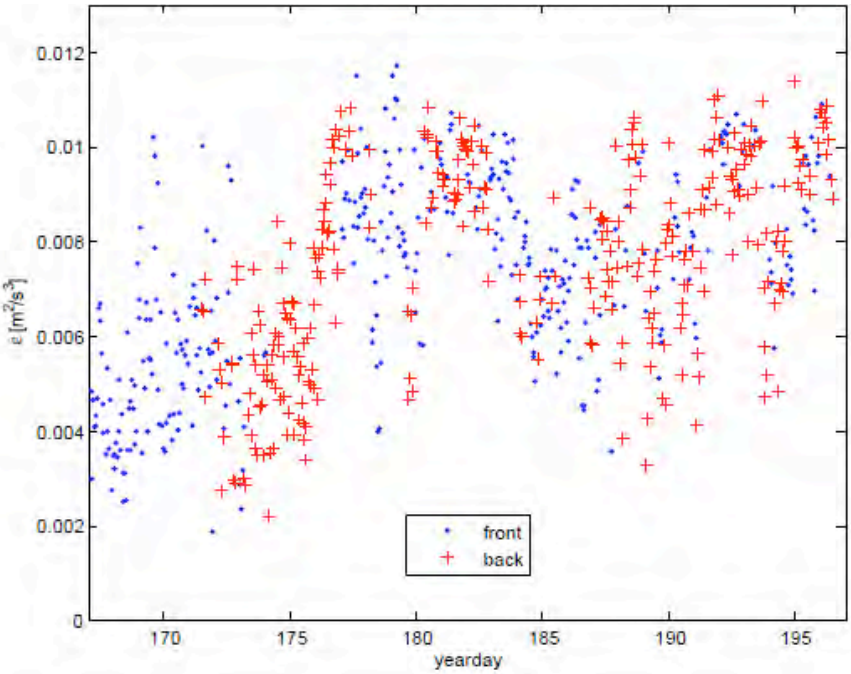

Figure 4.7. Separation of ε according to the direction of the flow for instrument A. Blue dots denotes flow coming toward the ASIS, and red crosses the opposite.

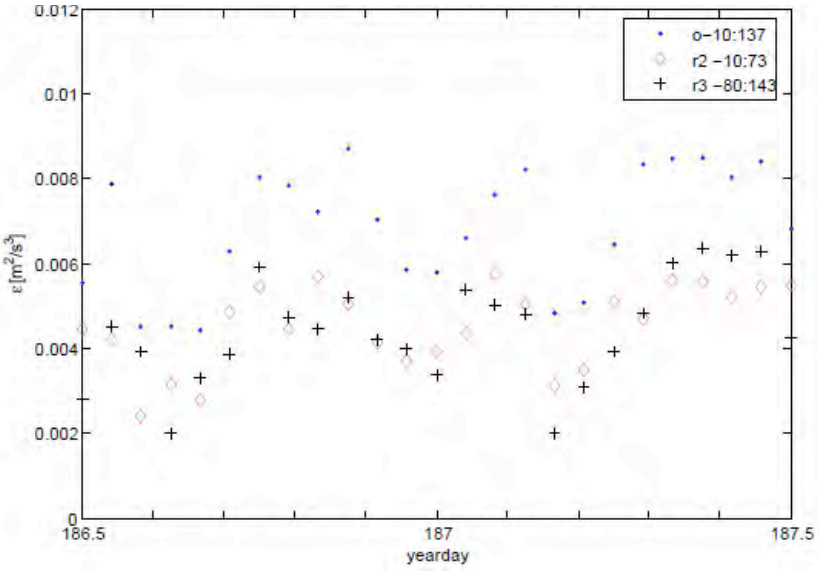

Figure 4.8. Values of ε for different ranges, to determine the distance of the ASIS structure influence (flow distortion) for instrument A. Blue dots are calculated taking bins 10 to 137; red diamonds from 10 to 73, and black crosses from 80 to 143, with bin #1 closest to the sensor, and a bin spacing of 8mm.

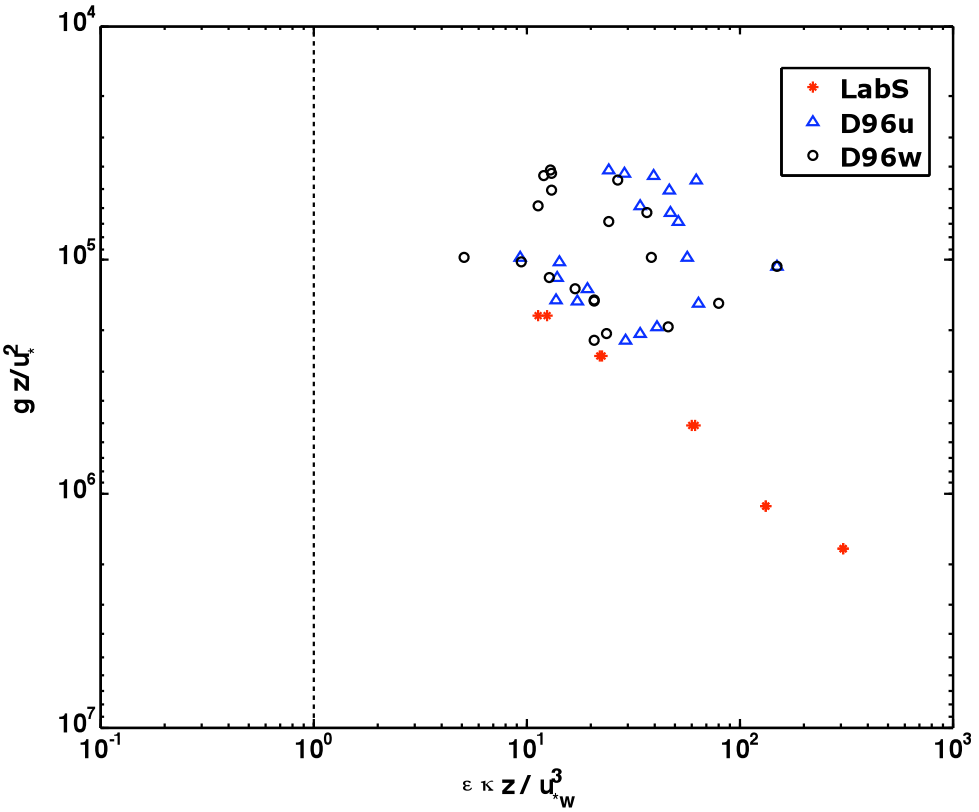

Figure 4.9. TKEDR with the Law of the wall scaling as in Drennan et al. (1996). The vertical line represents the result of wall layer theory. Diamonds correspond to horizontal values, while circles correspond to vertical values of ε .

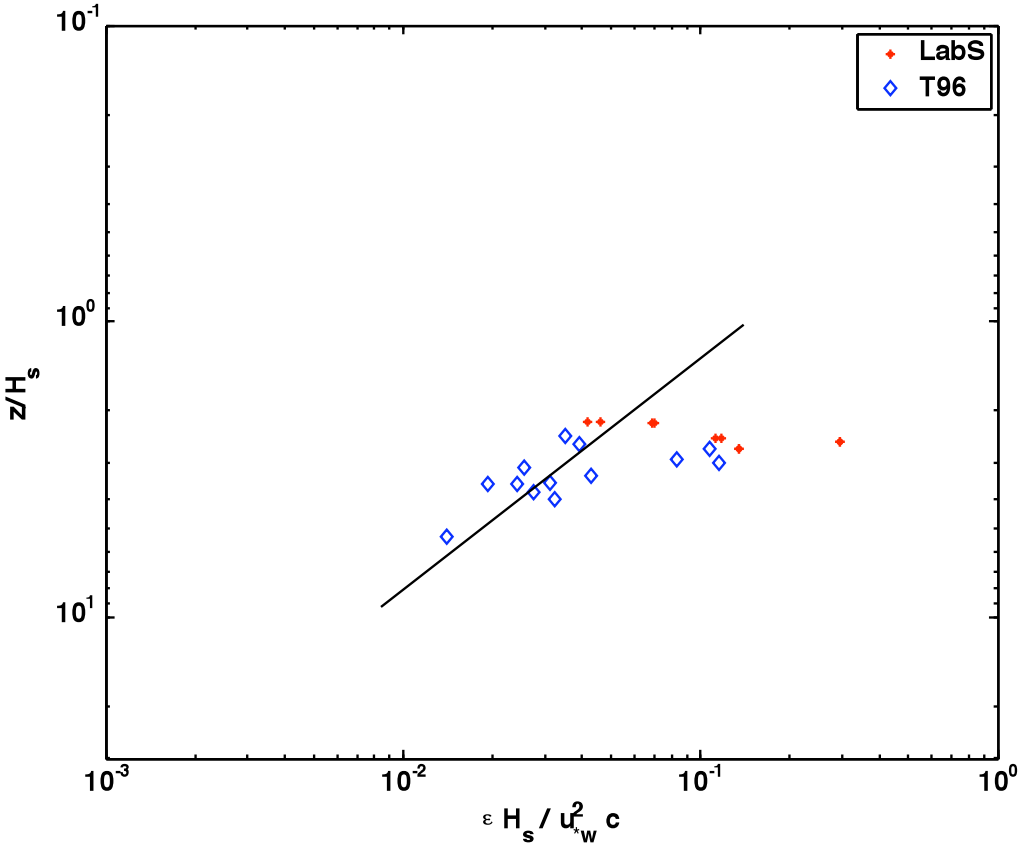

Figure 4.10 . TKEDR with the Terray scaling as in Terray et al. (1996). Blue diamonds are the Terray data for horizontal fluctuations, and the line is the regression line for their data. Red asterisks are our results, for horizontal TKEDR.

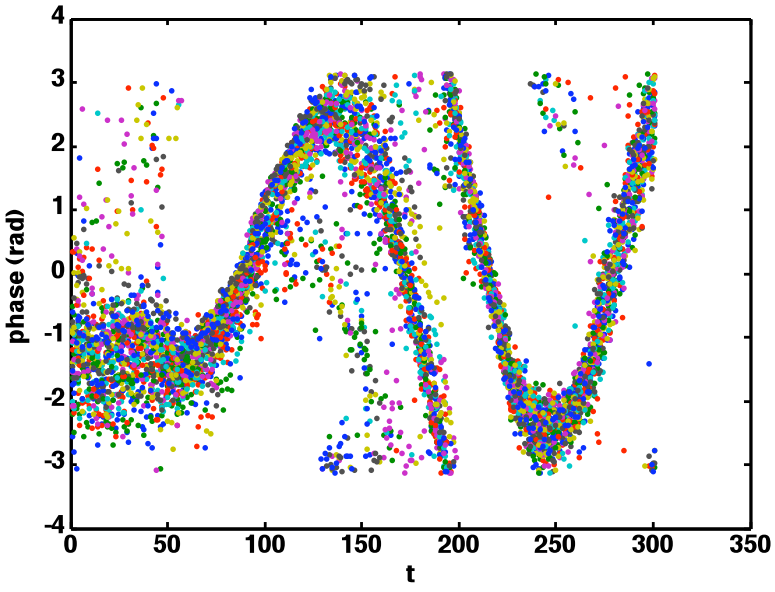

Figure 4.11. An example of the reverberation effect, for June 17th, at 0400 UTC. The colors denote different bins. The time steps represent 1/94 Hz.

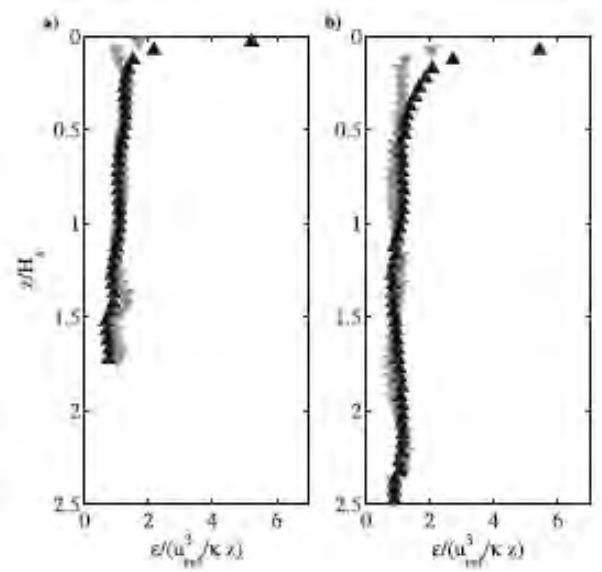

Figure 4.12. Normalized dissipation profile during frequent (a) and intermittent (b) wave breaking from Gemmrich (2010). Black upward (gray downward) triangles are data taken beneath wave crest (wave trough) regions.

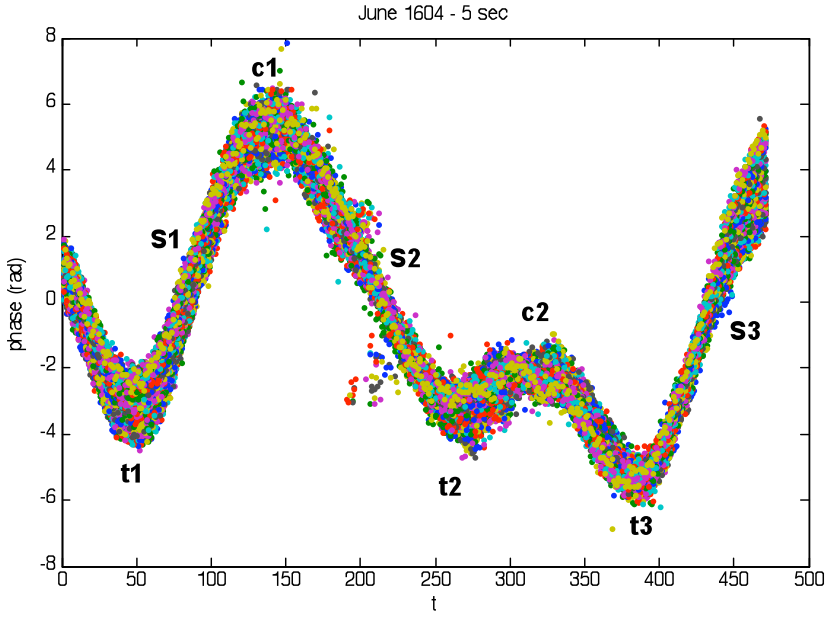

Figure 4.13. Unwrapped signal, with differentiation of crest (c), troughs (t) and sides (S). The colors denote different bins. The time steps represent 1/94 Hz

Chapter 5

Conclusions and final remarks

The study of turbulence at the surface ocean boundary layers is a complicated and wide-ranging subject. It involves different spatial-temporal scales, of several interrelated processes. In addition, the inherent difficulties of obtaining micro-scale measurements at sea make any estimate a challenge. Many aspects of the air-sea turbulent transfer remain still unknown, and it is the purpose of this dissertation to give new insight into some of the most important matters concerning flux measurements and turbulence in the open ocean.

Regarding the air-sea turbulent fluxes from the meteorological side, one of the fundamental points of the present research in the field is focused on improving their parameterization. Indeed, transfer calculations based on mean values of the different forcing parameters avoid some of the common difficulties related with the data acquisition at sea, i.e., sensors must be very durable and accurate, sampling rates must be high (at least 12 Hz), motion corrections must be applied to account for 3D accelerations and flow distortion due to the platform geometry (Anctil et al., 1994; Drennan, 2006) must be accounted for. The bulk formulae of turbulent transfer rates involve non-dimensional coefficients that have been reliably determined only under low-moderate wind conditions, i.e., between 4 and 15 m/s (Drennan, 2006; Donelan, 1990). The work presented in Chapter 2 is an attempt to improve the parameterization of the turbulent air-sea fluxes by determining those bulk coefficients during high wind conditions. Such an improvement translates into a direct improvement of the accuracy of the coupled ocean-

atmospheric models of climate prediction, fundamental in studies of global climate change.

The data set was obtained during the MAP experiment in summer 2006 on board the research vessel 'Celtic Explorer' in the North Atlantic Ocean. The area was chosen for being a well known phytoplankton bloom site during summer. The data set includes wind speed, temperature, humidity, CO_2 concentration, and sound speed fluctuations obtained from a bow-mounted flux tower that allows for the derivation of turbulent fluxes. The eddy covariance, bulk and inertial dissipation methods were all applied to obtain fluxes of momentum and humidity.

Interestingly, the data present some unique characteristics as regards the environmental conditions. Indeed a massive storm impacted the area after only a few days of measurements, allowing wind measurements of up to 24 m/s and hence some new insight into the bulk coefficient calculations in gale force winds. Measurements of momentum and humidity fluxes over 15 m/s in open ocean are very scarce making the results presented in Chapter 2 a key contribution to the field.

In addition, I also demonstrated the influence of the vessel structure in distorting the wind field, and also the calculated flux data. It has been shown in previous works that the geometry and shape of the vessel can influence the turbulent measurements and hence the flux calculations (Edson et al., 1998; Pedreros et al., 2003; Oost et al., 1994; Dupuis et al., 2003). We were able to confirm previous theories, and most importantly, to determine the flow distortion solely from the analysis of the data set. The frequencies most disturbed by this effect are in the range between 0.1 and 0.25 Hz. Up to 50% of the total recorded files needed to be discarded due to the flow distortion derived form the

platform. On the remaining files, only fluxes calculated by the inertial dissipation method proved reliable.

This work represents then a highly useful tool for improving the parameterization of humidity and momentum fluxes and the bulk coefficients (Drag and Dalton) associated with them. Indeed, it is concluded that the Drag coefficients change slightly during high winds, compared to values at low winds (about 12%), while Dalton coefficients remain constant with high winds up to 21 m/s.

On the oceanic side, the wind at the surface transmits a certain quantity of energy that is dissipated throughout the water column. However, many uncertainties exist today regarding the way this energy is transmitted to the ocean interior, measurable as turbulent kinetic dissipation rates (TKEDR). Many efforts in the past were focused on estimating these dissipation rates in somewhat deeper layers, of around 10-15 m (see Gargett, 2007 for a comprehensive review). In the upper 2 m of the ocean, the measurements are already a challenge. But in addition, the very few experiments carried out with the purpose of determining the upper layer's TKEDR do not agree about the order of magnitude they should have, nor seem to find a consensus about the surface forcing involved (winds, waves, water column stability, etc.), or how they should be related. The work presented in Chapter 4 addresses exactly this point, pointing out the most important forcing influencing TKE variability in the ocean.

An ASIS buoy, was deployed in the Labrador Sea, an important area of dense water production, during the summer of 2004. During the summer sunlight in combination with nutrients allow for a strong phytoplankton bloom to develop. The ASIS buoy is capable of measuring eddy correlation CO_2 fluxes, CO_2 profiles in the atmospheric BL and the

water column; wind speed, wind stress, atmospheric stability; surface waves, upper ocean turbulence and mixing. We focused our analysis on the data set obtained with the pulse-to-pulse acoustic Doppler radar, or DopBeam. Two groups of files were analyzed in detail: one with winds around 12 m/s and significant wave heights of 1.8 m and the other with winds of around 6 m/s and significant wave heights near 2 m.

In particular, the measurements of TKEDR in the Labrador Sea experiment are in agreement with the work of Terray et al. (1996) and Drennan et al. (1996). These introduced wave characteristics to the TKEDR scaling, instead of using the traditional 'Law of the Wall' (LOW) approach. Gemmrich (2010) challenged their results, and found TKEDR higher than the ones found in the previously cited publications. In addition, Gemmrich found that TKEDR within nonbreaking wave crests are on average 3 times larger than values found on the troughs of the wave; this ratio increased to 18 when frequent wave breaking occured. As wave breaking is not detectable in our experiment, we focused on a situation dominated by nonbreaking waves. The criterion used for selecting the non-breaking cases comes from previous field experiments involving ASIS buoys. Indeed it has been calculated that for winds around 10 m/s the percentage of wave breaking will be less than 5% of the total (Zhang, 2008; Zhang et al., 2008).

Note that the Terray et al. (1996) experiment (T96 from now on) was conducted from a tower, with the sensors below the lowest wave trough, at a fixed depth. The experiment conducted by Drennan et al. (1996) (D96) was conducted with ship-mounted sensors. The small ship was a surface follower for the big waves, so measurements were made at a roughly constant depth below the surface, but it was able to get higher in the crest regions than T96. According to Gemmrich, one would expect higher TKEDR values

in D96 than in T96, as D96 would include the higher TKEDR that T96 was missing. This was not the case. The T96 and D96 measurements were in support of each other in the T96 scaling.

Our statistical analysis showed that there is no preference for high TKEDR to exist at the crest of the wave. Gemmrich argued that the reason for the lower values of TKEDR obtained by Terray et al. (1996) and Drennan et al. (1996) was that their measurements were obtained way below the wave trough, measuring in this way only the low TKEDR related to the troughs. However, the input of the wind forcing (F) must be roughly equal to the integral of the TKEDR over 1 wavelength. If T96 and D96 underestimated some TKEDR, such an equation would not be balanced, as it actually is. Also note that our instrument not only remained near the very surface, but also is capable of distinguishing measurements in waves and troughs, something that T96 could not do, or was limited, in the case of D96. This capability of our DopBeam makes these results unique and a valuable addition to the knowledge in the field.

Regarding the DopBeam itself, we found some characteristics not cited before in literature, such as the effect of reverberation, and the different type of noise present in the files. In addition we performed an in depth analysis of the capabilities to determine the best range of data acquisition, quantifying the amount of flow distortion induced by the structure of the buoy (up to 11%), a novelty in this field.

In summary, the main contribution of this dissertation to the oceanic turbulence was to make near-surface estimates of TKEDR in the open ocean, to establish the non-dependence of TKEDR on wave phase and to prove that the correct scaling of the dissipation rates should consider the wave characteristics rather than just the wind effects,

as in the LOW. Regarding the DopBeam capabilities, the contribution to the field was to establish the best spatial range for our instrument, the best time averaging period, and the influence of the buoy structure.

Overall this dissertation has provided a fresh insight into a variety of turbulence phenomenology aspects, which are critically important to help elucidate the basic physics controlling near surface ocean processes in a global changing planet.

References

Agrawal, Y.C., Terray, E.A., Donelan, M.A., Hwang, P.A, Williams III, A.J., Drennan, W.M., Kahma, K.K. and Kitaigorodskii, S.A., 1992. 'Enhanced dissipation of kinetic energy beneath surface waves'. *Nature*, **359**, 219 – 220.

Anctil F., Donelan M., Drennan W. and Graber H., 1994. 'Eddy correlation measurements of air-sea fluxes from a Discus buoy'. *Journal of Atmospheric Oceanic Technology*, **11**, 1144-1150.

Anis, A., and J. N. Moum, 1992. 'The superadiabatic surface layer of the ocean during convection'. *Journal of Physical Oceanography*, **22**, 1221- 1227.

Avsic, T, Karstensen, J, Send, U, Fischer, J, 2006. 'Interannual variability of newly formed Labrador Sea water from 1994 to 2005'. *Geophysical Research Letters*, **33**, L21S02, doi:10.1029/2006GL026913.

Babanin, A.V, 2006. 'On a wave-induced turbulence and a wave-mixed upper ocean layer', *Geophysical Research Letters*, **33**, L206205, doi:10.1029/2006GL027308.

Babanin, A.V, and Haus, K.B., 2009. 'On the existence of water turbulence induced by nonbreaking surface waves'. *Journal of Physical Oceanography*, **39**, 2675 – 2679.

Bradshaw, P, 1976. 'Turbulence'. In '*Topics in Applied Physics*, *Volume 12'*, Springer – Verlag, 335 pp.

Champagne, F.H., Friehe, C.A., LaRue, J.C. and Wynagaard, J.C., 1977. 'Flux measurements, flux estimation techniques, and fine-scale turbulence measurements in the unstable surface layer over land'. *Journal of the Atmospheric Sciences,* **34**, 515 – 530.

Clarke R.A. and Gascard J.C., 1983. 'The formation of Labrador Sea water. Part I: Large-scale processes'. *Journal of Physical Oceanography*, **33**, 1764 - 1778.

DeCosmo J., Katsaros K.B., Smith S.D., Anderson R.J., Oost W.A., Bumke K. and Chadwick H., 1996. 'Air-sea exchange of water vapor and sensible heat: The Humidity Exchange Over the Sea (HEXOS) results'. *Journal of Geophysical Research*, **101(C5)**, 12,001 - 12,016.

Dilling L., Doney S.C., Edmonds J., Gurney K.R., Harriss R, Schimel D., Stephens B. and Stokes G., 2003. 'The role of carbon cycle observations and knowledge in carbon management'. *Annual Rev. of Environment and Resources*, **28**, 521 – 558.

Donelan M., 1990. 'Air-Sea interaction'. In *"The Sea: Ocean Engineering Science"*, Vol 9, John Wiley & Sons Eds., 238-292.

Donelan, M.A., Drennan, W.M. and Katsaros, K.B., 1997. 'The air-sea momentum flux in conditions of wind sea and swell', *Journal of Physical Oceanography,* **27**, 2087-2099.

Drennan W., 2006. 'On parameterizations of air-sea fluxes'. In *"Atmosphere-Ocean interaction"*, Vol 2, 1-33. Eds. W. Perrie, WIT Press.

Drennan W., Donelan M., Terray E. and Katsaros K., 1996. 'Oceanic turbulence dissipation measurements in SWADE'. *Journal of Physical Oceanography*, **26**, 5, 808-814.

Drennan W., Kahma K. and Donelan M., 1999. 'On momentum flux and velocity spectra over waves'. *Boundary-Layer Meteorology*, **92**, 489-515.

Drennan W.M., Zhang J.A., French J.R., McCormick C. and Black P.G., 2007. 'Turbulent fluxes in the Hurricane Boundary Layer. Part II: latent heat flux'. *Journal of the Atmospheric Sciences*, **64**, 1103-1115.

Dupuis, H., Guérin, C., Hauser, D., Weill, A., Nacass, P., Drennan, W.M., Cloché, S., & Graber, H.C., 2003. 'Impact of flow distortion corrections on turbulent fluxes estimated by the inertial dissipation method during the FETCH experiment on R/V L'Atalante'. *Journal of Geophysical Research*, **108** (C3), 8064, doi:10.1029/ 2001JC001075.

Edson, J.B., J.E. Hare, and C.W. Fairall, 1998. 'Direct covariance flux estimates from moving platforms at sea'. *Journal of Atmospheric and Oceanic Technology,* **15**, 547-562.

Fairall C.W and S.E. Larsen, 1986. 'Inertial-dissipation methods and turbulent fluxes at the air-ocean interface'. *Boundary-Layer Meteorology,* **34**, 287–301.

Fairall C., Hare J., Edson J. and McGillis W., 2000. 'Parameterization and micrometeorological measurement of air-sea gas transfer'. *Boundary-layer Meteorology*, **96**, 63-105.

French, J. R., Drennan W.M., Zhang J., and Black P.G., 2007. 'Turbulent fluxes in the hurricane boundary layer. Part I: Momentum flux'. *Journal of Atmospheric Science*, **64**, 1089 - 1102.

Garratt, J.R., 1977. 'Review of drag coefficients over oceans and continents'. *Monthly Weather Review*, **96**, 617-636.

Gargett, A., 1989. 'Ocean turbulence'. *Annual Review of Fluid Mechanics,* **21**, 419- 451.

Gargett, A., 1999. 'Velcro measurement of turbulence kinetic energy dissipation rate'. *Journal of Atmospheric and Oceanic Technology,* **16**, 1973-1993.

Gemmrich J., 2000. 'Temperature anomalies beneath breaking waves and the decay of wave-induced turbulence'. *Journal of Geophysical Research*, **105**, 8727-8736.

Gemmrich, J.R., 2010. 'Temperature anomalies beneath breaking waves and the decay of wave-induced turbulence'. *Journal of Geophysical Research*, **105(C4)**, 8727 - 8736.

Gemmrich J. and Farmer, D., 1999. 'Near-surface turbulence and thermal structure in a wind-driven sea'. *Journal of Physical Oceanography*, **29**, 480-499.

Gemmrich, J. and Farmer, D., 2004. 'Near-surface turbulence in the presence of breaking waves'. *Journal of Physical Oceanography*, **34**, 1067-1086.

Gerbi, G.P., Trowbridge, J.H., Terray, E.A., Plueddemann, A.J., Kukulka, T., 2008. 'Observations of Turbulence in the Ocean Surface Boundary Layer: Energetics and Transport'. *Journal of Physical Oceanography*, **39**, 1077-1096.

Gibson M.M, 1962. 'Spectra of turbulence in a round jet'. *Journal of Fluid Mechanics*, **15**, I2, 174-186.

Graber, H., Terray, E., Donelan, M.A., Drennan, W.M., Van Leer, J.C. and Peters, D.B, 2000. 'ASIS – A New Air – Sea Interaction Spar Buoy: design and performance at sea'. *Journal of Atmospheric and Oceanic Technology*, **17**, 708 – 720.

Grant, H.L., Stewart R.W. and Moilliet A.,1962. 'Turbulence spectra from a tidal channel'. *Journal of Fluid Mechanics*, **12**, 241- 268.

Grant H.L. and Moilliet, A., 1962. 'The spectrum of a cross-stream component of turbulence in a tidal stream', *Journal of Fluid Mechanics*, **13**, 237-240.

Hinze, J.O., 1959. *'Turbulence: An introduction to its mechanism and theory'*. McGraw-Hill, New York, USA. 586 pp.

Hinze, J.O., 1975. *'Turbulence'* – 2nd edition. Mc Graw Hill, 790 pp.

Högström, U., 1990. 'Analysis of turbulence structure in the surface layer with a modified similarity formulation for near neutral conditions'. *Journal of the Atmospheric Sciences*, **47**, 1949-1972.

Intergovernmental Panel on Climate Change (IPCC), 2007. 'Climate Change 2007: The Physical Science Basis. Contribution of Working Group I to the Fourth Assessment Report of the Intergovernmental Panel on Climate Change'. Solomon, S., D. Qin, M. Manning, Z. Chen, M. Marquis, K.B. Averyt, M. Tignor and H.L. Miller (Eds.). Cambridge University Press, Cambridge, United Kingdom and New York, NY, USA, 996 pp.

Jähne B. and Haußecker H., 1998. 'Air-water gas exchange'. *Annual Review of Fluid Mechanics*, **30**, 443-468.

Kolmogorov, A. and Nikolaevich, 1941. 'The local structure of turbulence in incompressible viscous fluid for very large Reynolds numbers'. *Proceedings of the USSR Academy of Sciences,* 30, 299–303 (Russian). Translated into English as Kolmogorov, A. and Nikolaevich (July 8, 1991). 'The local structure of turbulence in incompressible viscous fluid for very large Reynolds numbers'. *Proceedings of the Royal Society of London, Series A: Mathematical and Physical Sciences,* **434**, 9–13.

Kraus, E.B. and Businger, J.A., 1994. '*Atmosphere-Ocean Interaction*'. Oxford Univ. Press, ISBN 0-19-506618-9, 362 pp.

Lab Sea Group, 1998. 'The Labrador Sea Deep Convection experiment'. *Bulletin of the American Meteorological Society*, **79**, 2033-2058.

Lamont, J.C, Scott, D.S., 1970. 'An eddy cell model of mass transfer into the surface of a turbulent liquid', *American Institute of Chemical Engineering Journal*, **16**, No.4, 513 – 519.

Langmuir, I., 1938. 'Surface motion of water induced by wind'. *Science*, **87**, 119 - 123.

Large, W. G., and S. Pond, 1981. 'Open ocean momentum flux measurements in moderate to strong winds'. *Journal of Physical Oceanography*, **11**, 324–336.

Lazier, J.R., 1973. 'The renewal of Labrador Sea water'. *Deep-Sea Research*, **20**, 341-353.

Lhermitte, R. and Haus, B. K., 1999. 'Tidal flow velocity and turbulence measurement by coherent Doppler sonar'. Technical Report No. RSMAS 99-007. University of Miami, Miami, FL.

Lhermitte, R., and Serafin., R, 1984. 'Pulse-to-pulse coherent doppler sonar signal processing techniques'. *Journal of Atmosph. and Oceanic Technology*, **1**, 297-299.

Lhormann, A., Hackett B. and Roed L.D.., 1999. 'High resolution measurements of turbulence, velocity, and stress using a pulse-to-pulse coherent sonar'. *Journal of Atmospheric and Oceanic Technology*, **7**, 19-37.

Lorke A. and Peeters F., 2006. 'Toward a unified scaling relation for interfacial fluxes'. *Journal of Physical Oceanography,* **36**, 955-961.

Lumley, J.L. and Terray, E.A. 1983. 'Kinematics of turbulence convected by a random wave field'. *Journal of Physical Oceanography*, **13**, 2000-2007.

Marshall, J. and Schott, F. 1999. 'Open ocean convection: observation, theory and models'. *Reviews of Geophysics*, **37**, 1-23.

Martz, T, DeGrandpre, M, Strutton, P.G, McGillis, W.R, Drennan, W.M, 2009, 'Sea surface pCO2 and carbon export during the Labrador Sea spring-summer bloom: an in situ mass balance approach'. *Journal of Geophysical Research,* **114**, c09008, DOI:10.1029/2008JC005060.

McGillis W., Edson J., Ware J., Dacey J., Hare J., Fairall C. and Wanninkhof R., 2001. 'Carbon dioxide flux techniques performed during GasEx-98'. *Marine Chemistry*, **75**, 267-280.

Melville, K.W., Veron, F. and White, C.J., 2002. 'The velocity field under breaking waves: Coherent structures and turbulence'. *Journal of Fluid Mechanics*, **454**, 203-233.

Miyake, M., Stewart, R.W. and Burling, R.W., 1970. 'Spectra and cospectra of turbulence over water', *Quarterly Journal of the Royal Meteorological Society*, **96**, 138-143.

Monin, A.S., and Obukhov, A.M, 1954. 'Basic laws of turbulent mixing in the ground layer of the atmosphere'. *Trudy Geofiz. Inst., Akad. Nauk SSSR*, **151**, 163–187.

Obukhov, A. M., 1946. 'Turbulence in a thermally inhomogeneous atmosphere'. *Boundary-Layer Meteorology*, **2**, 7–29.

O'Dowd, C.D., Facchini M.C., Cavalli F., Ceburnis D., Mircea M., Decesari S., Fuzzi S., Yoon Y.J. and Putaud, J.P., 2004. 'Biogenically driven organic contribution to marine aerosol'. *Nature*, **431**, 676-680.

Oost, W.A., Fairall, C.W., Edson, J.B., Smith, S.D., Anderson, R.J., Willis, J.A.B., Katsaros, K.B. and DeCosmo, J., 1994. 'Flow distortion calculations and their application in HEXMAX'. *Journal of Atmospheric and Oceanic Technology*, **11**, 366 – 381.

Pedreros, R., Dardier, G., Dupuis, H., Graber, H.C., Drennan, W.M., Weill, A., Guérin, C., and Nacass, P. 2003. 'Momentum and heat fluxes via the eddy correlation method on the R/V L'Atalante and an ASIS buoy'. *Journal of Geophysical Research*, **108** (C11), 3339, doi:10.1029/2002JC001449.

Petersen, G.N., and Renfrew I.A., 2009. 'Aircraft-based observations of air-sea fluxes over Denmark Strait and the Irminger Sea during high wind speed conditions'. *Quarterly Journal of the Royal Meteorological Society*, **135**, 1950 - 1967.

Pettersson, H., H.C. Graber, D. Hauser, C. Quentin, K.K. Kahma, W.M. Drennan, and M.A. Donelan, 2003. 'Directional wave measurements from three wave sensors during the FETCH experiment'. *Journal of Geophysical Research*, **108** (C3), 8061, doi:10.1029/ 2001JC001164.

Phillips, O.M., 1977. '*The dynamics of the Upper Ocean*'. 2nd edition, 336 p.

Popinet, S., Smith, M. and Stevens, S., 2004. 'Experimental and numerical study of the turbulence characteristics of airflow around a research vessel'. *Journal of Atmospheric and Oceanic technology*, **21**, 1575 -1588.

Rapp, R.J., and Melville W.K., 1990. 'Measurements of deep-water breaking waves'. *Philosophical Transactions of the Royal Society of London. Series A, Mathematical and Physical Sciences*, **331(1622)**, 735 - 800.

Sahlée E., Smedman A.S., Hogstrom U. and Rutgerson A., 2008. 'Reevaluation of the Bulk exchange coefficient for humidity at sea during unstable and neutral conditions'. *Journal of Physical Oceanography*, **38**, 257-272.

Seuront, L., Yamazaki H. and Schmitt F.G., 2005. 'Intermittency'. In book : '*Marine Turbulence: Theories, Observations and Models*". H. Baumert, J. Sundermann, and J. Simpson Eds. Cambridge Univ. Press, Cambridge, U.K. pp. 66 - 78.

Smith, S. D., 1980. 'Wind stress and heat flux over the ocean in gale force winds'. *Journal of Physical Oceanography*, **10**, 709-726.

Smith S.D., R.J. Anderson, W.A. Oost, C. Kraan, N. Maat, J. deCosmo, K.B. Katsaros, K.L. Davidson, K. Bumke, L. Hasse and H.M. Chadwick, 1992. 'Sea surface wind stress and drag coefficients: the HEXOS results'. *Boundary-Layer Meteorology,* **60**, 109-142.

Soloviev, A.V., Vershinsky, N.V, Bezverchnii, V.A, 1988. 'Small scale turbulence measurements in the thin surface layer of the ocean', *Deep-Sea Research*, **35**, 1867-1870.

Strutton, P.G., Martz, T.R., DeGrandpre, M.D., McGillis, W.R. and W.M. Drennan., 2008. 'Bio-optical observations of the 2004 Labrador Sea phytoplankton bloom'. *Journal of Geophysical Research*, under review.

Stull, R.B., 1988. *'An Introduction to Boundary Layer Meteorology'*. Kluwer Academic, 666 pp.

Tasai, F., and Ocean Research Group of R.I.A.M., 1980. 'Direct measurements of the Kuroshio (I)'. *Bulletin of Research Institute of Applied Mechanics Kyushu Univ.*, **52**, 29 – 98.

Takahashi, T., S. C. Sutherland, C. Sweeney, A. Poisson, N. Metzel, B. Tilbrook, N. Bates, R. Wanninkhof, R. A. Feely, C. Sabine, J. Olafsson, and Y. Nojiri, 2002. 'Global sea-air CO_2 flux based on climatological surface ocean pCO_2, and seasonal biological and temperature effects'. *Deep-Sea Research II*, **49**, 1601-1622.

Taylor, G.I., 1938. 'The spectrum of turbulence'. *Proceedings of the Royal Society of London Series A: Mathematical and Physical Sciences*, **164(919)**, 476 - 490.

Taylor, P.K., and Yelland, M.J., 2001. 'Comments on "On the effect of ocean waves on the kinetic energy balance and consequences for the inertial dissipation technique"'. *Journal of Physical Oceanography*, **31,** 2532-2536.

Tennekes, H. and Lumley, J.L., 1972. '*A First Course in Turbulence*", The MIT Press, 300 pp.

Terray, E.A., Donelan, M.A., Agrawal, Y.C., Drennan, W.M., Kahma, K.K., Williams III, A.J., Hwang, P.A., Kitaigorodskii, S.A., 1996. 'Estimates of kinetic energy dissipation under breaking waves'. *Journal of Physical Oceanography,* **26,** 792 – 807.

Thorpe, S.A., 2007. 'Recent developments in the study of ocean turbulence'. *Annual Review of Earth and Planetary Science*, **32**, 91-109.

Turner, J.S. 1973. '*Buoyancy Effects in Fluids'*. Cambridge University Press, 367 pp.

Veron F. and Melville W.K., 1999. 'Pulse-to-pulse coherent Doppler measurements of waves and turbulence'. *Journal of Atmospheric and Oceanic Technology*, **16**, 1580-1597.

Wieringa, J., 1980. 'A re-evaluation of the Kansas mast influence on measurements of stress and cup anemometer overspeeding'. *Boundary-Layer Meteorology*, **18**, 411 - 430.

Wiles, P.J., Rippeth, T.P., Simpson, J,H., Hendricks, P.J., 2006. 'A novel Technique for measuring the rate of turbulent dissipation in the marine environment', *Geophysical Research Letters*, **33**, L21608, doi:10.1029/2006GL027050.

Wyngaard J.C., 1981. 'The effects of probe-induced flow distortion on atmospheric turbulence measurements'. *Journal of Applied Meteorology*, **20**, 784 - 794.

Yelland, M. J., B. I. Moat, P. K. Taylor, R. W. Pascal, J. Hutchings, V. C. Cornell, 1998. 'Wind stress measurements from the open ocean corrected for airflow distortion by the ship'. *Journal of Physical Oceanography*, **28**, 1511–1526.

Zappa, C., McGillis, W.R., Raymond, P.A., Edson, J.B., Hintsa. E.J., Zemmelink, H.J., Dacey, J.W.H., Ho, D.T., 2007. 'Environmental turbulent mixing controls on air-water gas exchange in marine and aquatic systems'. *Geophysical Research Letters*, **34**, L10601, doi:10.1029/2006GL028790.

Zhang, F., 2008. 'On the variability of the wind stress at the air-sea interface', University of Miami dissertation, 149 pp.

Zhang F.W., Drennan W.M., Haus, B.K, Graber, H.C., 2009. 'On wind-wave interactions during the Shoaling Waves experiment'. *Journal of Geophysical Research*, **114**, C01018, doi:10.1029/2008JC004998.